DTU Fotonik
Department of Photonics Engineering

Electromagnetic Scattering in Micro- and Nanostructured Materials

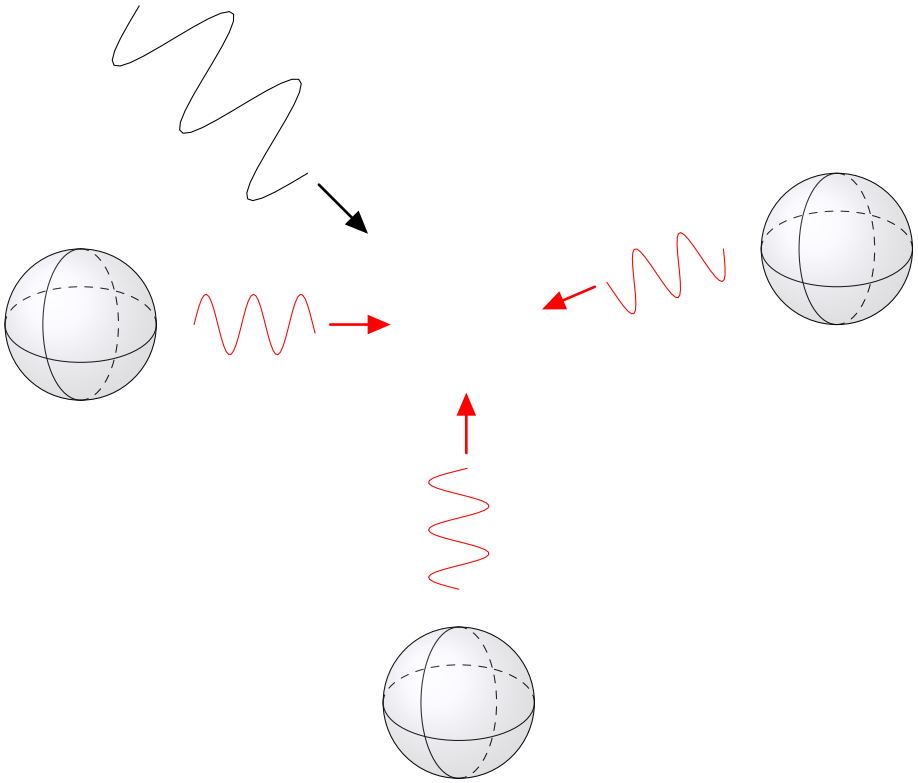

Jakob Rosenkrantz de Lasson

Master's Thesis
July 2012

Electromagnetic Scattering in Micro- and Nanostructured Materials

This thesis was prepared, written, and typeset by

Jakob Rosenkrantz de Lasson (s072159)

Under supervision by

Professor Jesper Mørk
Postdoc Philip Trøst Kristensen

Affiliated with

Technical University of Denmark
DTU Fotonik
Department of Photonics Engineering
Nanophotonics Theory & Signal Processing

Ørsteds Plads building 345v
DK-2800 Kgs. Lyngby
Denmark

Web: http://www.fotonik.dtu.dk/Forskning/Nanophotonics/NanoTheory

---

Project period:	January 30, 2012 – July 13, 2012
Type:	Master's thesis
Study programme:	Physics and Nanotechnology
ECTS:	32.5
Edition:	Second
Comments:	The report was typeset using LaTeX 2_ε and the memoir class, and is intended to be printed in color. All sketches and illustrations were created using TikZ. Numerical calculations and graphical plots were performed using MATLAB.

Abstract

The research fields of optical microstructures and plasmonic nanostructures are particularly active these years, and interesting applications in, e.g., quantum information technology in the former and novel types of solar cells in the latter, drive the investigations. Central in both fields is the interaction of light with matter, in the forms of semiconductors and metals in the two cases, and fundamental understanding of the interactions is important to optimize technological designs.

To address this, we in the present thesis develop a formalism for determining the electric field in a homogeneous three dimensional space with spherical inhomogeneities embedded. The formalism accounts fully for the multiple reflections the field undergoes in such structures, and likewise the vectorial nature of the field is treated rigorously. The formalism is based on the Lippmann-Schwinger equation and the electromagnetic Green's tensor and uses an expansion of the field on spherical wavefunctions. Addition theorems for these are extensively used, and all parts of the formalism are expressed analytically.

With the formalism, we show that the simpler approach of modeling the spherical scatterers as polarizable dipoles, which is often alluded to in the literature, breaks down in the limit of closely spaced scattering objects. The study of metallic nanoparticles is particularly intriguing when these are in close proximity, due to the coupling of their near-fields, and the breakdown of the simpler approach reveals a need for the present formalism.

Additionally, we study dimers and chains of metallic nanoparticles and analyze their spectra, when exposed to fields of different polarizations. The spectral response is highly dependent on the polarization, and we demonstrate for the dimer, under polarization along the dimer axis, a $d^{-1/2}$-dependence of the relative shift of the resonance wavelength, d being the distance between the particles. This dependence on d is softer than reported earlier, and thus constitutes the foundation for a more systematic study. The correlation of distance and spectral properties may have applications within biosensing and -imaging on the nanoscale. For the chain, we demonstrate a next-nearest neighbor interaction between the nanoparticles through the study of its spectral properties. Finally, we present a calculation of the Green's tensor for the dimer, illustrating that the formalism may likewise be used for modeling optical microstructures, e.g. three dimensional photonic crystals.

Resumé

Forksningsfelterne inden for optiske mikrostrukturer og plasmoniske nanostrukturer er særdeles aktive i disse år, og interessante anvendelser i f.eks. kvanteinformationsteknologi i førstnævnte og nye typer af solceller i sidstnævnte, motiverer undersøgelserne. Inden for begge felter er lys-stof vekselvirkningen, med henholdsvis halvledermaterialer og metaller, central, og grundlæggende forståelse heraf er vigtig for at kunne optimere teknologiske designs.

I den kontekst præsenterer vi i denne afhandling en formalisme til at beregne det elektriske felt i et homogent tredimensionelt materiale, hvori sfæriske inhomogeniteter er indlejret. I formalismen inkluderes de multiple reflektioner, feltet undergår i denne type geometri, og feltets vektorielle natur behandles ligeledes stringent. Formalismen er baseret på Lippmann-Schwinger ligningen og den elektromagnetiske Green's tensor og anvender en udvikling af feltet på sfæriske bølgefunktioner. Additionssætninger for disse anvendes i stort omfang, og alle dele af formalismen er udtrykt analytisk.

Med formalismen viser vi, at den simple tilgang, hvor spredningsobjekterne behandles som polariserbare dipoler, og som ofte anvendes i litteraturen, bryder sammen, når spredningsobjekterne placeres tæt ved hinanden. Studier af metalliske nanopartikler er særligt interessante, når disse er tæt på hinanden, pga. koblingen af deres nærfelter, og sammenbruddet af den simplere tilgang bevidner et behov for formalismen fra denne afhandling.

Endvidere undersøger vi dimere og kæder af metalliske nanopartikler, samt analyserer deres spektrer når de belyses af felter med forskellige polarisationer. Det spektrale respons afhænger kraftigt af polarisationen, og vi viser for dimeren, at det relative resonansbølgelængdeskift, når feltet er polariseret langs med dimeraksen, har en $d^{-1/2}$-afhængighed, hvor d er afstanden mellem de to partikler. Denne afhængighed af d er svagere end rapporteret i litteraturen og udgør dermed grundlaget for mere systematiske undersøgelser. Korrelationen af afstanden og de spektrale egenskaber kan have anvendelser inden for biodetektion og -billeddannelse på nanoskala. For kæden finder vi en næstnærmeste nabovekselvirkning mellem partiklerne ved at analysere dens spektrum. Endelig udfører vi en beregning af Green's tensoren for dimeren, hvilket illustrerer, at formalismen også kan bruges til at regne på optiske mikrostrukturer, eksempelvis tredimensionelle fotoniske krystaller.

Preface

This thesis is submitted as fulfillment of the requirements for obtaining the degree of Master of Science in Engineering in Physics and Nanotechnology at the Technical University of Denmark (DTU). The work has been carried out in collaboration with the Nanophotonics Theory & Signal Processing group at DTU Fotonik, Department of Photonics Engineering, under the supervision of Professor Jesper Mørk and Postdoc Philip Trøst Kristensen.

I am indebted to my thesis supervisors, Jesper and Philip, for their competent and encouraging guidance throughout the project. In particular, I thank Philip for always having time to discuss the little details and the big picture in the project and for enthusiastically engaging in my work.

I thank the board of Civilingeniør Bernhard Eisenreich Sandersen og Hustru Ruth Sandersens Mindelegat for a small economic grant for the project. Likewise, I thank my good friend and fellow student, Thomas Christensen, for a joyful study time, filled with many hours of hard work and inspiring discussions, both about physics and more general aspects of life. During the work with our respective theses, we had many interesting talks, about physics, about LaTeX and about many other things, and they all made the work a little bit more fun.

Finally, I thank Jørn Bindslev Hansen, Associate Professor at DTU Fysik, Department of Physics at DTU, for having reviewed a smaller part of the present thesis. The contact with Jørn during my studies at DTU has been inspiring and enlightening, and I encourage more physicists to stand as Jørn does.

Jakob Rosenkrantz de Lasson
Technical University of Denmark, Kgs. Lyngby
July 2012

Contents

List of Figures

CHAPTER 1

Introduction

> *We are like tenant farmers chopping down the fence around our house for fuel when we should be using Natures inexhaustible sources of energy – sun, wind and tide. ... I'd put my money on the sun and solar energy. What a source of power! I hope we don't have to wait until oil and coal run out before we tackle that.*
>
> Thomas A. Edison, *Uncommon Friends: Life with Thomas Edison, Henry Ford, Harvey Firestone, Alexis Carrel & Charles Lindbergh*

Plasmonics and Solar Cells

The research area of plasmonics has received significant attention in recent years, and virtually any type of application involving plasmonics has been proposed: Guiding and confinement of light beyond the diffraction limit [1], amplifiers and lasers [2], nanotweezers for manipulation at the nanoscale [3], metal particles as nanoantennas [4] and many more.

The main ingredient in plasmonics is metals, and one intriguing optical property of these, as compared to insulators and semiconductors, is their highly dispersive nature: The optical response of metals depends critically on the frequency of the light. This makes them interesting candidates in such applications as sensing and detection, e.g. for use in molecular sensing [5].

The strong dispersion implies that spectral properties of metallic structures, e.g. in the form of nanoparticles, may be significantly altered by varying various parameters, including the surrounding medium, the size of the metal object, and in the case of nanoparticles their shape [6]. The optical behavior of metals is mediated by oscillations

of free electrons in the material, which may give rise to so-called plasmons, and at the plasmon resonances the metallic nanoparticles may act as strong scatterers and absorbers of light. This has promoted their use in new types of solar cells.

The worldwide energy consumption continues to increase, and solar cells are a promising energy source and alternative to fossil fuels. A conventional solar cell is several hundred microns in thickness, produced mainly of silicon that constitutes the largest part of the production cost. To decrease the production cost, and to maintain the technology competitive, thin-film solar cells, with thicknesses on the order of one to two microns, have been proposed. The reduced thickness and production cost, however, come at a price: A thinner substrate absorbs less of the incident light which effectively reduces the energy produced by the solar cell. Consequently, structuring of the surface of thin-film solar cells is needed, and for that purpose nanosize metal particles have been suggested [7].

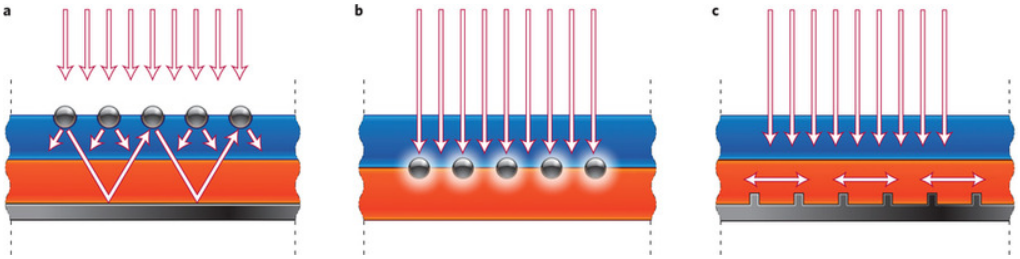

Figure 1.1 Schematic of three types of plasmonic assisted enhancements of absorption in thin-film solar cells: (a) Light trapping by scattering, (b) light trapping by excitation of localized surface plasmons, and (c) light trapping by excitation of surface plasmon polaritons. Figure from Ref. [7].

In Fig. 1.1, three ways of using plasmonic structuring to enhance the absorption in thin-film solar cells are shown. In-coupling via scattering on metallic nanoparticles, preferentially in the forward direction, is shown in section (a). Additionally, the light undergoes multiple reflections in the device, due to scattering on the particles, which effectively increases the optical path in the solar cell. In section (b), localized surface plasmons are excited in the metal particles, and the strongly enhanced near-field excite electron-hole pairs in the solar cell. Finally, a metallic grating may support surface plasmon polaritons used for effectively coupling light into the solar cell in section (c). An example of the use of nanoparticles for solar cells can be found in Ref. [8], while a grating-based device is investigated in Ref. [9]. The rest of this work focuses on analyses of nanoparticles and not gratings.

To optimize designs based on the use of metallic nanoparticles in solar cells, or in any of the other applications, systematic studies of these and their properties are essential. To that end, both experimental and theoretical investigations must be conducted, and we in this work take a theoretical and computational approach hereto.

Simulation Schemes

Maxwell's equations, that light in the form of electromagnetic waves satisfy in a classical description, have been known since the 1860's, and nevertheless they remain among the most difficult equations in physics to solve. This stems from the vectorial nature of the

involved electromagnetic fields, which in particular in three dimensional (3D) structures, to be investigated in this work, complicates the solution procedure.

Simple analytical solutions of Maxwell's equations are only available in highly symmetric geometries, and consequently much effort has been put into numerical solution schemes for modeling of technological devices. Methods based on spatial discretization such as finite-difference time-domain (FDTD) [10] and the finite element method (FEM) [11] are widely used. These are, in principle, capable of treating arbitrary geometries, but the necessity to discretize the entire computational domain leads to large memory requirements, in particular in the 3D geometries we have in mind here.

As we outline in detail in later chapters, we will be concerned with modeling of the electric field in a homogeneous 3D space with spherical scattering objects embedded. These scattering objects in some specific analyses take the forms of metallic nanoparticles. The scattering of a plane wave on a single spherical scatterer was solved by Mie in 1908 [12]. In the limit of non-interacting scatterers, problems involving several scattering objects can be analyzed by the Mie theory, and this approach was taken for analyzing plasmonic solar cells in Ref. [13]. Similarly, the quasi-static approximation in which the field is determined from electrostatics, and which is valid for particles with characteristic lengths much smaller than the wavelength of light [14, Chap. 5], is often applied. This approach provides insightful analytical expressions, but its validity breaks down in the limit of closely spaced particles [15]. In contrast to these approaches, we have a solution involving fully scatterer-scatterer and scatterer-background interactions with no restrictions on index contrasts, scatterer sizes or scatterer spacing in mind.

The scattering of a wave on more than one obstacle is complicated by the multiple reflections the wave undergoes. This is shown artistically on the title page where an incident wave (black) impinges on three spherical scatterers. This gives rise to primary scattered waves (red), that interfere and undergo multiple reflections that have to be rigorously accounted for. Different methods for solving this type of problem have been proposed: Xu in Ref. [16] presents a generalized Mie scattering theory for geometries with multiple spheres, and García de Abajo in Ref. [17] proposes a similar technique. These, and the formalism to be presented in this work, have two main ingredients: The expansion of the field on spherical wavefunctions, solutions to the homogeneous Helmholtz equation, and the addition theorems for these so-called multipoles.

In the present work, we base the analyses on the Lippmann-Schwinger equation and the electromagnetic Green's tensor. The field, in contrast to 2D simulations where it can be decomposed into TE- and TM-fields, has three non-zero components, and is expanded on spherical wavefunctions inside the scattering objects. Subsequently, a matrix equation for the associated expansion coefficients is obtained, and all involved matrix elements are expressed analytically. The choice of basis functions restricts the analyses to spherical scatterers, but the analytical work prompts high speed in computations and arbitrarily accurate results, only limited by the truncations imposed by the practical implementation. Additionally, the formalism contains an explicit error estimate, which is not available in the other schemes, in particular not in FDTD and FEM. The overall ideas in the present method were outlined and carried out for 2D geometries in Refs. [18, 19]; We generalize it for the 3D case. Finally, it should be noted that the formalism resembles the so-called Rayleigh multipole method, presented and applied in 2D in Ref. [20].

Perspectives

As alluded to in the introductory part of this chapter, plasmonics is a very active and rapidly evolving field of research these years. Much effort is put into the study of small metal particles to understand their properties, how they interact and most importantly how nanoparticles can be tailored for the applications mentioned earlier. In Chapters 4 and 5 of this work, we employ the formalism outlined in the previous section to analyze such nanosize metal particles. However, it is important to stress that this only represents one example of the applicability of the method; It is not restricted to analyses within plasmonics.

Another very active field of research is that of optical microstructures, e.g. in the form of micropillars or photonic crystals. Microcavities already play a prominent role in lasers for long-distance optical communication [21], and reliable single-photon sources, for use in quantum information technology, have been realized with a quantum dot embedded in a micropillar [22]. The latter technology relies on Purcell enhancement [23] of the spontaneous emission rate of the quantum dot, and the local density of states and the Purcell factor can be computed from the Green's tensor [24, Chap. 8], which is easily extractable in the present formalism. Refs. [18, 19] apply the formalism for analyzing 2D photonic crystals, and the 3D version developed in this work can be used for modeling more realistic 3D photonic crystals.

As a final note, the plasmonic solar cell discussed in connection with Fig. 1.1 inherently involves a layered geometry. The formalism developed in this work does not allow the modeling of layered geometries, but in the final chapter an outlook for this extension is given.

Outline of Thesis

Chapter 2: From Maxwell's equations the Lippmann-Schwinger equation is obtained. Similarly, the important concept of cross sections, used for analyzing arrays of plasmonic particles in later chapters, is introduced.

Chapter 3: For the specific geometry of spherical scatterers in a homogeneous 3D space, a solution technique for the Lippmann-Schwinger equation is presented in detail.

Chapter 4: The error estimate from the solution of the Lippmann-Schwinger equation is investigated, and likewise preliminary results for the cross sections are presented and discussed. Finally, the small-scatterer limit of the Lippmann-Schwinger equation, the so-called dipole approximation, is analyzed.

Chapter 5: Plasmonic dimers and chains are analyzed, and in particular the spectral tailoring of these is investigated and quantified. Illustrative calculations of quasinormal modes support the analyses, and the Green's tensor is computed and discussed for a resonant dimer.

Chapter 6: Conclusion and outlook for the work presented in the thesis.

Additionally, a number of appendices provide detailed derivations, explicit expressions and a number of numerical results. Reference is made to these throughout the chapters. Parts of the work presented in the thesis have been submitted for The Fifth International Workshop on Theoretical and Computational Nano-Photonics (TaCoNa), and the contribution is included in Appendix E (p. 109ff).

CHAPTER 2

Theoretical Foundation for Scattering Analyses

> *The theory I propose may therefore be called a theory of the Electromagnetic Field because it has to do with the space in the neighbourhood of the electric or magnetic bodies, and it may be called a Dynamical Theory, because it assumes that in the space there is matter in motion, by which the observed electromagnetic phenomena are produced.*
>
> James C. Maxwell, *A Dynamical Theory of the Electromagnetic Field*

This chapter outlines the fundamental equations and concepts that we build upon in the rest of this work. Starting from Maxwell's equations, we arrive at the frequency-space wave equation for the electric field. The solution of this is expressed formally via the Lippmann-Schwinger equation, the solution of which is the starting point for all analyses in later chapters. Subsequently, we introduce the radiation condition and the scattering amplitude for the scattered electric field, and this connects to the cross sections that are derivable from the scattering amplitude. The cross sections form the basis for analyses of metal particles in Chapters 4 and 5, and we in the concluding section of this chapter review the properties of such particles, by the introduction of the Drude model and a brief discussion of localized surface plasmons.

Where no other reference is given, we refer to Ref. [25].

2.1 Wave Equation for Electric Field

The starting point for the analyses is the macroscopic form of Maxwell's equations

$$\nabla \cdot \mathbf{D} = \rho, \tag{2.1a}$$
$$\nabla \cdot \mathbf{B} = 0, \tag{2.1b}$$
$$\nabla \times \mathbf{E} = -\frac{\partial}{\partial t}\mathbf{B}, \tag{2.1c}$$
$$\nabla \times \mathbf{H} = \mathbf{J} + \frac{\partial}{\partial t}\mathbf{D}, \tag{2.1d}$$

where $\mathbf{E}$, $\mathbf{D}$, $\mathbf{B}$, $\mathbf{H}$ are the electric field, the electric displacement field, the magnetic induction field, and the magnetic field, respectively. The fields are all functions of space and time, but we have suppressed this dependence above. In the absence of external stimuli, i.e. no external charges or current, we may set $\rho = 0$ and $\mathbf{J} = \mathbf{0}$, valid for semiconductors, but also for metals (see, e.g., [26, Chap. 13] or [14, Chap. 1]), and we assume this condition throughout the work.

To proceed, we need constitutive relations that give the response of the material under consideration to the electromagnetic field, and in the regime of linear and local response, these can be expressed as follows

$$\mathbf{D} = \epsilon_0 \epsilon \mathbf{E}, \tag{2.2a}$$
$$\mathbf{B} = \mu_0 \mathbf{H}, \tag{2.2b}$$

where ϵ_0 and μ_0 are the permittivity and permeability of free space, respectively, and ϵ is the relative permittivity. We have directly set the relative permeability $\mu = 1$ implying that we consider non-magnetic materials. The relative permittivity, which we henceforth simply term the permittivity or the dielectric function, may depend on both position and frequency, and we return to this later. In a more general description, the permittivity may be a tensor accounting for anisotropic effects, and in the formalism to be developed in the following chapter, this could could rather simply be included. Nevertheless, we restrict the analyses to isotropic response.

Taking the curl of Eq. (2.1c) and replacing $\mathbf{B}$ from the magnetic constitutive relation, Eq. (2.2b), we have

$$\nabla \times \nabla \times \mathbf{E} = -\mu_0 \frac{\partial}{\partial t} \left(\nabla \times \mathbf{H} \right). \tag{2.3}$$

Replacing then the curl of the magnetic field using the fourth of Maxwell's equations, Eq. (2.1d) with $\mathbf{J} = \mathbf{0}$, and inserting the electric constitutive relation, Eq. (2.2a), we have the wave equation for the electric field

$$\nabla \times \nabla \times \mathbf{E} + \frac{\epsilon}{c^2} \frac{\partial^2}{\partial t^2} \mathbf{E} = 0. \tag{2.4}$$

In this work, we shall in particular be analyzing the spectral properties of scattering objects, and we consequently seek a spectral representation of the electric field. To that end, we introduce the Fourier transform pair of the electric field

$$\mathbf{E}(\mathbf{r}; t) = \int \mathbf{E}(\mathbf{r}; \omega) \exp(-i\omega t) \, \mathrm{d}\omega, \tag{2.5a}$$
$$\mathbf{E}(\mathbf{r}; \omega) = \frac{1}{2\pi} \int \mathbf{E}(\mathbf{r}; t) \exp(i\omega t) \, \mathrm{d}t, \tag{2.5b}$$

where we use the symbol $\mathbf{E}$ for both the time-domain and frequency-domain representations of the electric field. Unless otherwise stated, the spectral representation is implied onward. We then Fourier transform Eq. (2.4), as prescribed by Eq. (2.5b), and obtain the following frequency-space equation for the electric field

$$\nabla \times \nabla \times \mathbf{E}(\mathbf{r};\omega) - k_0^2 \epsilon(\mathbf{r};\omega)\mathbf{E}(\mathbf{r};\omega) = 0, \qquad k_0 \equiv \frac{\omega}{c}, \tag{2.6}$$

where we have written the spatial and spectral dependence explicitly. We have introduced the free-space wave number, k_0, related to the free-space wavelength through

$$\lambda_0 = \frac{2\pi}{k_0} = \frac{2\pi c}{\omega}. \tag{2.7}$$

In a particular situation, we, in principle, specify the frequency, ω, but this last relation implies that we may equivalently specify the free-space wavelength, which we do consistently in the calculations in later chapters.

2.2 Lippmann-Schwinger Equation

The Lippmann-Schwinger equation, to be presented in the following section, forms the basis of the scattering analyses of this work, and we therefore in some detail motivate its introduction. For a rigorous derivation of the equation, see [24, Chap. 2].

2.2.1 Derivation

In the scope of performing scattering calculations, where inhomogeneities are embedded in a homogeneous background matrix, we introduce the dielectric contrast

$$\Delta\epsilon(\mathbf{r};\omega) \equiv \epsilon(\mathbf{r};\omega) - \epsilon_{\mathrm{B}}(\omega), \tag{2.8}$$

where ϵ_{B} is the permittivity of the background material. We use this to replace ϵ in Eq. (2.6) and rearrange slightly to find

$$\nabla \times \nabla \times \mathbf{E}(\mathbf{r};\omega) - k_0^2 \epsilon_{\mathrm{B}}(\omega)\mathbf{E}(\mathbf{r};\omega) = k_0^2 \Delta\epsilon(\mathbf{r};\omega)\mathbf{E}(\mathbf{r};\omega). \tag{2.9}$$

This equation contains the same information as Eq. (2.6), but its interpretation is more intuitive: The right-hand side of the equation, that depends on the unknown field $\mathbf{E}$ itself, acts as a driver through the finite permittivity difference $\Delta\epsilon$. The solution for such an equation is the sum of the homogeneous solution and an inhomogeneous solution

$$\mathbf{E}(\mathbf{r}) = \mathbf{E}_{\mathrm{B}}(\mathbf{r}) + \mathbf{E}_{\mathrm{scat}}(\mathbf{r}), \tag{2.10}$$

where $\mathbf{E}_{\mathrm{B}}$ is the homogeneous solution, and $\mathbf{E}_{\mathrm{scat}}$ is the inhomogeneous solution, or the scattered field. As mentioned above, the driver of Eq. (2.9) depends on the unknown field itself which suggests that the scattered field will be the solution of a self-consistent equation. We develop this equation in the following.

In the theory of inhomogeneous differential equations, particular solutions can sometimes be found using a Green's function. To illustrate this technique, we consider a simple example

$$\mathcal{L}_\nu f(\nu) = b(\nu), \tag{2.11}$$

where f is an unknown function, b is a (known) driver, $\mathcal{L}$ is a linear differential operator, and ν is a composite variable. The function f is also subject to boundary conditions that we do not specify further. The complete solution of such an equation is the complete solution of the homogeneous equation ($\mathcal{L}f_0 = 0$) plus a particular solution ($\mathcal{L}f_\mathrm{s} = b$), $f = f_0 + f_\mathrm{s}$. We suppose that f_0 is known and in the following focus on finding f_s.

To that end, we consider the same inhomogeneous equation, but with the driver replaced by Dirac's delta function

$$\mathcal{L}_\nu G(\nu, \nu') = \delta(\nu - \nu'), \tag{2.12}$$

where G is the Green's function, subject to the same boundary conditions as f. By virtue of the above equation, we see that

$$f_\mathrm{s}(\nu) = \int G(\nu, \nu') b(\nu') \, \mathrm{d}\nu', \tag{2.13}$$

is a particular solution, since

$$\begin{aligned} \mathcal{L}_\nu f_\mathrm{s} &= \int \mathcal{L}_\nu G(\nu, \nu') b(\nu') \, \mathrm{d}\nu' \\ &= \int \delta(\nu - \nu') b(\nu') \, \mathrm{d}\nu' \\ &= b(\nu). \end{aligned} \tag{2.14}$$

Thus, provided that Eq. (2.12) can be solved, the above outlines a means to finding a particular solution of the inhomogeneous equation.

In the above, we considered scalar functions in which case a scalar Green's function was sufficient. But the electric field is a vector field, and we have no à priori knowledge permitting us to assume that the scattered electric field can be derived from a scalar Green's function. Consequently, we need to generalize the basic example from above to differential equations for vector fields which can be done using a dyadic Green's function which is a second-order tensor. Following [24, Chap. 2], we write the scattered field as follows

$$\mathbf{E}_\mathrm{scat}(\mathbf{r}) = \int_V \mathbf{G}_\mathrm{B}(\mathbf{r}, \mathbf{r}') k_0^2 \Delta\epsilon(\mathbf{r}') \mathbf{E}(\mathbf{r}') \, \mathrm{d}\mathbf{r}', \tag{2.15}$$

where $\mathbf{G}_\mathrm{B}(\mathbf{r}, \mathbf{r}')$ is the electromagnetic Green's tensor, which is the solution of Eq. (2.9) with the right-hand side replaced by $\delta(\mathbf{r} - \mathbf{r}')\mathbf{I}$, $\mathbf{I}$ being a unit dyad. The integral extends over the space where $\Delta\epsilon(\mathbf{r}') \neq 0$, the source region, but to find the scattered field for $\mathbf{r}$ inside this region, an important addition must be made. In Eq. (2.14), we implicitly assumed that $\mathcal{L}_\nu$ and $\int \mathrm{d}\nu'$ commute, by pulling $\mathcal{L}_\nu$ under the integral. When $\mathbf{r}$ is in the source region, this does not hold, and additionally the Green's tensor diverges at $\mathbf{r} = \mathbf{r}'$. These issues were thoroughly analyzed by Yaghjian in Ref. [27], with the following outcome, which is widely used in the literature (see, e.g., Refs. [19, 28])

$$\mathbf{E}_\mathrm{scat}(\mathbf{r}) = \int_{V - \delta V} \mathbf{G}_\mathrm{B}(\mathbf{r}, \mathbf{r}') k_0^2 \Delta\epsilon(\mathbf{r}') \mathbf{E}(\mathbf{r}') \, \mathrm{d}\mathbf{r}' - \frac{\Delta\epsilon(\mathbf{r})}{\epsilon_\mathrm{B}} \mathbf{L}\mathbf{E}(\mathbf{r}). \tag{2.16}$$

The integral is now evaluated as a Principal value, avoiding the singularity at $\mathbf{r} = \mathbf{r}'$, and $\mathbf{L}$ is a source dyadic, whose exact form depends on the shape of the volume excluding the point at $\mathbf{r} = \mathbf{r}'$. As discussed in the above reference, the expression is unique in the

sense that a change in the shape of the exclusion volume alters the contribution from the integral term in a way that is exactly balanced by the contribution from the source dyadic term. Collecting we have thus obtained the Lippmann-Schwinger equation for the electric field

$$\boxed{\mathbf{E}(\mathbf{r}) = \mathbf{E}_{\mathrm{B}}(\mathbf{r}) + \int_{V-\delta V} \mathbf{G}_{\mathrm{B}}(\mathbf{r},\mathbf{r}')k_0^2\Delta\epsilon(\mathbf{r}')\mathbf{E}(\mathbf{r}')\,\mathrm{d}\mathbf{r}' - \frac{\Delta\epsilon(\mathbf{r})}{\epsilon_{\mathrm{B}}}\mathbf{L}\mathbf{E}(\mathbf{r}).} \tag{2.17}$$

This equation is the central result of this chapter, and all ensuing analyses take their starting point in the solution of this equation. In the following chapter, we solve it in a system of spherical scatterers in a homogeneous 3D space, but we can already outline the solution procedure:

1. Since the integral extends over the parts of space with $\Delta\epsilon(\mathbf{r}') \neq 0$, it is an implicit equation for the electric field in these regions

$$\mathbf{E}(\mathbf{r}_{\mathrm{scat}}) = \mathbf{E}_{\mathrm{B}}(\mathbf{r}_{\mathrm{scat}}) + \int_{V-\delta V} \mathbf{G}_{\mathrm{B}}(\mathbf{r}_{\mathrm{scat}},\mathbf{r}')k_0^2\Delta\epsilon(\mathbf{r}')\mathbf{E}(\mathbf{r}')\,\mathrm{d}\mathbf{r}' - \frac{\Delta\epsilon(\mathbf{r}_{\mathrm{scat}})}{\epsilon_{\mathrm{B}}}\mathbf{L}\mathbf{E}(\mathbf{r}_{\mathrm{scat}}). \tag{2.18a}$$

   Conceptually, the solution in the source regions is the difficult part, and we present in detail a technique for doing this in the following chapter.

2. Once the field inside the scatterers is determined, the field outside the scatterers is obtained by a straightforward evaluation of the Lippmann-Schwinger equation

$$\mathbf{E}(\mathbf{r}_{\mathrm{nonscat}}) = \mathbf{E}_{\mathrm{B}}(\mathbf{r}_{\mathrm{nonscat}}) + \int_{V} \mathbf{G}_{\mathrm{B}}(\mathbf{r}_{\mathrm{nonscat}},\mathbf{r}')k_0^2\Delta\epsilon(\mathbf{r}')\mathbf{E}(\mathbf{r}')\,\mathrm{d}\mathbf{r}', \tag{2.18b}$$

   where it has been used that $\Delta\epsilon(\mathbf{r}_{\mathrm{nonscat}}) = 0$, by construction.

The source dyadic, as stated above, depends on the shape of the exclusion volume, and as we will be working with spherical scatterers, it is natural to choose a spherical exclusion volume. In 3D, this gives the following source dyadic [27]

$$\mathbf{L} \equiv \mathbf{L}_{\mathrm{3D,sph}} = \frac{1}{3}\begin{bmatrix} 1 & 0 & 0 \\ 0 & 1 & 0 \\ 0 & 0 & 1 \end{bmatrix}. \tag{2.19}$$

The definition and various properties of the Green's tensor, $\mathbf{G}_{\mathrm{B}}(\mathbf{r},\mathbf{r}')$ are given in Section 3.3.1.

2.2.2 Error Estimate

In the previous section, we outlined the solution procedure for the Lippmann-Schwinger equation, and we in particular noted that the equation is an implicit equation for the field in the source region. To assess the self-consistent solution of the equation in this region, we define the local error of the Lippmann-Schwinger equation as follows

$$\mathcal{E}_{\mathrm{L}}^{\mathrm{abs}}(\mathbf{r}) \equiv \left|\mathbf{E}_{\mathrm{B}}(\mathbf{r}) + \int_{V-\delta V} \mathbf{G}_{\mathrm{B}}(\mathbf{r},\mathbf{r}')k_0^2\Delta\epsilon(\mathbf{r}')\mathbf{E}(\mathbf{r}')\,\mathrm{d}\mathbf{r}' - \left(\frac{\Delta\epsilon(\mathbf{r})}{\epsilon_{\mathrm{B}}}\mathbf{L} + \mathbf{I}\right)\mathbf{E}(\mathbf{r})\right|, \tag{2.20a}$$

$$\mathcal{E}_{\mathrm{L}}(\mathbf{r}) \equiv \sum_{\alpha} \frac{\mathcal{E}_{\mathrm{L}}^{\mathrm{abs}}(\mathbf{r})}{|\mathbf{E}(\mathbf{r})|}, \tag{2.20b}$$

where $\mathcal{E}_{\mathrm{L}}^{\mathrm{abs}}(\mathbf{r})$ and $\mathcal{E}_{\mathrm{L}}(\mathbf{r})$ are the local error and local relative error, respectively. It is implied that $\mathbf{r}$ is inside a scatterer, and the sum is over the three polarizations. We also define the global relative error of the equation

$$\mathcal{E}_{\mathrm{G}} \equiv \sum_{\alpha} \frac{\int_V \mathcal{E}_{\mathrm{L}}^{\mathrm{abs}}(\mathbf{r})\,\mathrm{d}\mathbf{r}}{\int_V |\mathbf{E}(\mathbf{r})|\,\mathrm{d}\mathbf{r}}. \tag{2.21}$$

In practice, we solve the Lippmann-Schwinger equation analytically, and the only approximation is imposed by the truncation of the sets of basis functions. So the local and global relative errors can be used as quantitative measures for the number of basis functions needed to obtain convergent results. In Chapter 4, we present examples of both the local and global relative error.

2.3 Boundary Conditions and Radiation Condition

At interfaces between different media, i and j, the electric field and the electric displacement field satisfy the following boundary conditions [25, Chap. 1]

$$\mathbf{E}_{i,\parallel} = \mathbf{E}_{j,\parallel}, \tag{2.22a}$$

$$\mathbf{D}_{i,\perp} = \mathbf{D}_{j,\perp}. \tag{2.22b}$$

When solving the Lippmann-Schwinger equation, Eq. (2.17), we do not take these boundary conditions into consideration explicitly, but since these and the Lippmann-Schwinger equation are derivable from Maxwell's equations, the boundary conditions will indeed be satisfied. We verify this in a specific case in Chapter 4.

The scattered field results from the multiple scatterings where $\Delta\epsilon(\mathbf{r}) \neq 0$, and looking far away from the scattering sites, we expect this field to propagate outwards. Specifically, it should satisfy the Sommerfeld radiation condition at large distances, $1 \ll k_{\mathrm{B}} r$, [25, Chap. 10]

$$\mathbf{E}_{\mathrm{scat}}(\mathbf{r}) \sim \mathbf{f}(\theta,\phi) E_0 \frac{\exp(ik_{\mathrm{B}} r)}{r}, \qquad 1 \ll k_{\mathrm{B}} r. \tag{2.23}$$

E_0 is the amplitude of the incoming field, and the vectorial amplitude, $\mathbf{f}(\theta,\phi)$, is the scattering amplitude, or far-field radiation pattern. The latter holds essential information about the scattering and absorption properties of the scatterers which we return to in the next section and again in the following chapters.

2.4 Extinction, Scattering and Absorption Cross Sections

In the following, we apply the conservation of energy for a general scattering problem to obtain expressions for the so-called extinction, scattering and absorption cross sections, being important quantitative measures for the properties of the scatterers. We base the discussions and derivations on [25, Chap. 10] and [26, Chap. 13].

In the following, we assume that ϵ_{B} is real, i.e., the background material is lossless, and we restrict the discussion to incoming plane waves of the form

$$\mathbf{E}_{\mathrm{B}}(\mathbf{r}) = E_0 \exp(i\mathbf{k}_{\mathrm{B}} \cdot \mathbf{r})\,\mathbf{e}_{\mathrm{B}} \tag{2.24}$$

where E_0 and $\mathbf{k}_{\mathrm{B}}$ are the amplitude and the wave vector of the incoming plane wave, respectively, while $\mathbf{e}_{\mathrm{B}}$ is the unit polarization vector of the incoming wave. The wave vector is described in spherical coordinates by k_{B}, θ_k and ϕ_k.

With the Fourier transform pair in Eqs. (2.5), we allowed for arbitrary time-dependence, but the following is based on harmonic time-dependence, $\mathbf{E}(\mathbf{r};t) = \mathbf{E}(\mathbf{r};\omega)\exp(-i\omega t)$. In this case, the energy flow of the field resulting from the scattering problem is described by the time-averaged Poynting vector

$$\mathbf{S}(\mathbf{r};\omega) = \frac{1}{2\mu_0}\mathrm{Re}\left(\mathbf{E}(\mathbf{r};\omega)\times\mathbf{B}^*(\mathbf{r};\omega)\right), \tag{2.25}$$

where we have written the spatial and spectral dependences explicitly; These are omitted in the following. By the form of the total fields, $\mathbf{E} = \mathbf{E}_\mathrm{B} + \mathbf{E}_\mathrm{scat}$ and $\mathbf{B} = \mathbf{B}_\mathrm{B} + \mathbf{B}_\mathrm{scat}$, this may be expressed more explicitly as follows

$$\mathbf{S} = \mathbf{S}_\mathrm{B} + \mathbf{S}_\mathrm{scat} + \mathbf{S}_\mathrm{ext}, \tag{2.26a}$$

$$\mathbf{S}_\mathrm{B} \equiv \frac{1}{2\mu_0}\mathrm{Re}\left(\mathbf{E}_\mathrm{B}\times\mathbf{B}_\mathrm{B}^*\right), \tag{2.26b}$$

$$\mathbf{S}_\mathrm{scat} \equiv \frac{1}{2\mu_0}\mathrm{Re}\left(\mathbf{E}_\mathrm{scat}\times\mathbf{B}_\mathrm{scat}^*\right), \tag{2.26c}$$

$$\mathbf{S}_\mathrm{ext} \equiv \frac{1}{2\mu_0}\mathrm{Re}\left(\mathbf{E}_\mathrm{B}\times\mathbf{B}_\mathrm{scat}^* + \mathbf{E}_\mathrm{scat}\times\mathbf{B}_\mathrm{B}^*\right). \tag{2.26d}$$

In Fig. 2.1, an arbitrary scattering geometry is shown, in 2D for simplicity: Four scattering objects with permittivities ϵ_j, that may or may not depend on position and frequency, are embedded in a non-dissipative background medium with permittivity ϵ_B. The structure is illuminated by a plane wave, $\mathbf{E}_\mathrm{B}$, with wave vector $\mathbf{k}_\mathrm{B}$, and the dashed circle indicates a large, imaginary sphere, S_1, of radius $r, 1 \ll k_\mathrm{B}r$, that encloses all the scatterers.

The flux of the total time-averaged Poynting vector, $\mathbf{S}$, outwards through this *closed* sphere is equal in magnitude and opposite in sign to the rate at which energy is absorbed by the scatterers, P_abs (indicated schematically by a red arrow into one of the scatterers in Fig. 2.1). This statement reflects the fact that whatever energy enters the sphere and does not come out must have been dissipated inside the scatterers. We thus have

$$P_\mathrm{abs} = -\oint_{S_1}\mathbf{S}\cdot\mathbf{n}\,\mathrm{d}A = -\left(\oint_{S_1}\mathbf{S}_\mathrm{B}\cdot\mathbf{n}\,\mathrm{d}A + \oint_{S_1}\mathbf{S}_\mathrm{scat}\cdot\mathbf{n}\,\mathrm{d}A + \oint_{S_1}\mathbf{S}_\mathrm{ext}\cdot\mathbf{n}\,\mathrm{d}A\right), \tag{2.27}$$

where $\mathbf{n}$ is a unit outwards directed normal vector on S_1. Since the background material is non-absorbing, we have $\oint_{S_1}\mathbf{S}_\mathrm{B}\cdot\mathbf{n}\,\mathrm{d}A = 0$. The total power removed from the incident field, P, either by absorption in the scatterers or by scattering into the far-field, may then be written as

$$P = P_\mathrm{abs} + P_\mathrm{scat} = -\oint_{S_1}\mathbf{S}_\mathrm{ext}\cdot\mathbf{n}\,\mathrm{d}A, \tag{2.28}$$

where the power carried by the scattered field out through S_1 is $P_\mathrm{scat} = \oint_{S_1}\mathbf{S}_\mathrm{scat}\cdot\mathbf{n}\,\mathrm{d}A$.

The related cross sections are defined as the ratio between the associated power and the incident power per unit area

$$C_\mathrm{ext} \equiv \frac{P}{|\mathbf{S}_\mathrm{B}|}, \tag{2.29a}$$

$$C_\mathrm{scat} \equiv \frac{P_\mathrm{scat}}{|\mathbf{S}_\mathrm{B}|}, \tag{2.29b}$$

$$C_\mathrm{abs} \equiv \frac{P_\mathrm{abs}}{|\mathbf{S}_\mathrm{B}|}, \tag{2.29c}$$

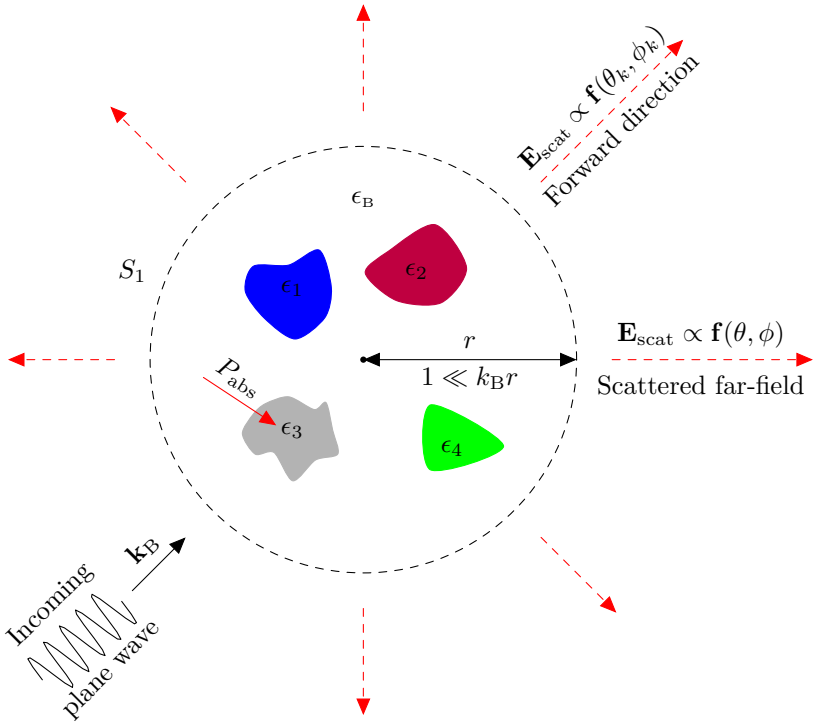

Figure 2.1 Arbitrary scattering geometry, consisting of four scatterers that are illuminated by a plane wave, $\mathbf{E}_{\text{B}}$. The dashed circle indicates an imaginary sphere, S_1, that encloses all the scatterers, and the dashed red arrows indicate the scattered far-field which is proportional to the scattering amplitude, $\mathbf{f}(\theta, \phi)$. The forward direction is indicated, and the power absorption, P_{abs}, is introduced by a red arrow into one of the scatterers.

where C_{ext}, C_{scat} and C_{abs} are the extinction, scattering and absorption cross section, respectively. These cross sections have the dimension of area and can be thought of as equivalent cross sectional areas of the scatterers under consideration; When the cross sections are large, it corresponds to scattering on or absorption by objects that are geometrically larger than the scatterers [6]. In this picture, it is customary to normalize the cross sections to the geometrical cross sections, and we do this below.

The surface integrals defining the powers can be evaluated, but they can be expressed more elegantly, in terms of the internal fields inside the scatterers and the scattering amplitude, $\mathbf{f}(\theta, \phi)$. Firstly, the scattering cross section can be written as follows

$$C_{\text{scat}} = \lim_{k_{\text{B}} r \to \infty} \frac{\int |\mathbf{E}_{\text{scat}}|^2 r^2 \, \mathrm{d}\Omega}{|E_0|^2}, \tag{2.30}$$

where the integration is over all solid angles (see Eq. (A.4)). In the above relation, the integral over the imaginary sphere S_1 has been replaced by an integral at infinity: The scattered power that propagates away from the scatterers remains unchanged and may, in the view of the asymptotic form of the scattered field in Eq. (2.23), conveniently be

computed at $k_{\mathrm{B}}r \to \infty$. Inserting this, we readily have

$$C_{\mathrm{scat}} = \int |\mathbf{f}(\theta, \phi)|^2 \, \mathrm{d}\Omega. \tag{2.31}$$

The extinction cross section can be expressed by means of the Optical theorem

$$C_{\mathrm{ext}} = \frac{4\pi}{k_{\mathrm{B}}} \mathrm{Im} \left(\mathbf{f}(\theta_k, \phi_k) \cdot \mathbf{e}_{\mathrm{B}}^* \right), \tag{2.32}$$

where $\mathbf{f}(\theta_k, \phi_k)$ is the scattering amplitude in the forward direction, as indicated in Fig. 2.1. This relation implies that the power removed from the incident wave vanishes unless some energy is scattered in the forward direction. The Optical theorem has an analogue in scattering in quantum mechanics, reflecting the conservation of probability of the wavefunction, see, e.g., [29, Chap. 7].

Combining Eqs. (2.28)-(2.29), we have

$$C_{\mathrm{abs}} = C_{\mathrm{ext}} - C_{\mathrm{scat}}, \tag{2.33}$$

so when C_{ext} and C_{scat} are determined, we strictly do not need to compute the absorption cross section independently. However, to validate the computations we seek an independent expression for C_{abs}. As discussed earlier, P_{abs} is the power absorbed by the scatterers, and we therefore expect this quantity to vanish when the permittivity of the scatterers is purely real. Likewise, we expect the quantity to be related to the energy distribution (proportional to the magnitude squared of the field) integrated inside the scatterers. This is shown rigorously by Ishimaru in Ref. [30, Chap. 2] with the following result

$$C_{\mathrm{abs}} = \frac{k_{\mathrm{B}}}{\epsilon_{\mathrm{B}}} \frac{\int_V |\mathbf{E}(\mathbf{r}')|^2 \mathrm{Im}(\epsilon(\mathbf{r}')) \, \mathrm{d}\mathbf{r}'}{|E_0|^2}, \tag{2.34}$$

where the integral is taken over the scatterer volumes. In the formalism to be developed in the following chapter, this expression will prove particularly simple to evaluate. This expression for C_{abs} is also used in [31, Chap. 2].

As mentioned earlier in this section, the cross sections are equivalent cross sectional areas, and it is therefore customary to normalize these to the geometrical cross sectional areas of the scatterers, giving rise to the so-called efficiencies. For spherical scatterers this is done through

$$Q_{\mathrm{i}} \equiv \frac{C_{\mathrm{i}}}{N\pi R^2}, \qquad \mathrm{i} \in \{\mathrm{ext}, \mathrm{scat}, \mathrm{abs}\}, \tag{2.35}$$

where N and R are the number of spherical scatterers and the radius of these, respectively.

The concepts developed in this section are, with the exception of the efficiencies defined specifically for spherical scatterers, completely general when considering the scattering and absorption of a plane wave on a collection of scatterers. In Section 3.6, we briefly review the cross sections in the specific context of spherical scatterers and express these more explicitly.

2.5 Drude Model and Localized Surface Plasmons

In Chapters 4 and 5, we consider the scattering of electromagnetic waves on metallic spheres, and to that end we in this section briefly review the properties of these. In

particular, we introduce the Drude model and briefly discuss the properties of localized surface plasmons, with reference made to [14, Chaps. 1 and 5].

The optical response of metals, expressed through the permittivity, $\epsilon_{\text{metal}}(\omega)$, can be described by considering the response of the free electron plasma in the metal to an external electric field. The oscillations of the plasma may be modeled as a damped harmonic oscillator, driven by the external field, and following the procedure of the above reference this leads to

$$\epsilon_{\text{metal}}(\omega) = 1 - \frac{\omega_{\text{p}}^2}{\omega^2 + i\gamma\omega}, \tag{2.36}$$

where ω_{p} and γ are the plasma frequency and the collision frequency, respectively. The validity of the Drude model is good for frequencies in the infrared spectrum and the lower frequencies of the visible spectrum, while for larger frequencies measured values of the permittivity start to deviate from the Drude model result. This is due to the excitation of bound electrons in the metals from high-energy photons, giving rise to interband transitions in the metal which may be accounted for by more sophisticated models. However, the Drude model in the form in Eq. (2.36) will suffice and be applied for the scattering calculations of this thesis. We use the parameters of Ref. [32], valid for silver (Ag)

$$\hbar\omega_{\text{p}}^{\text{Ag}} = 7.9 \text{ eV}, \tag{2.37aa}$$

$$\hbar\gamma^{\text{Ag}} = 0.06 \text{ eV}, \tag{2.37ab}$$

or the parameters from Ref. [17], valid for aluminum (Al), in the specific calculations

$$\hbar\omega_{\text{p}}^{\text{Al}} = 15 \text{ eV}, \tag{2.37ba}$$

$$\hbar\gamma^{\text{Al}} = 1.06 \text{ eV}. \tag{2.37bb}$$

When we embed metallic scatterers in a background medium with real permittivity, an insulator or semiconductor, the interface between the media may sustain localized fields, the so-called localized surface plasmons. These are collective oscillations of the free electrons in the metal bound to the metal-insulator/dielectric interface, and may exhibit large field enhancements. Similarly, as we shall see in Chapter 5, the localized plasmons on different metal particles may couple resonantly, and we analyze how this coupling depends on distance and polarization.

2.6 Summary

From Maxwell's equation, we have derived the frequency-space scattering equation, the Lippmann-Schwinger equation. In the next chapter, we choose a specific geometry and in detail present a formalism for solving this equation. Furthermore, we have introduced the extinction, scattering and absorption cross sections, and we have related these to the far-field radiation pattern via the scattering amplitude. Finally, we have reviewed the dielectric response of metals, through the introduction of the Drude model, and briefly discussed the properties of localized fields at interfaces between metals and insulators/semiconductors, the so-called localized surface plasmons. Detailed analyses of these and the cross sections will be performed in Chapters 4 and 5.

CHAPTER 3

Solution Technique for Lippmann-Schwinger Equation

> *...But you were talking about physics and if that's what you're talking about, then to not know mathematics is a severe limitation in understanding the world.*
>
> Richard P. Feynman, *The Pleasure of Finding Things Out*

This chapter develops, for the specific geometry of spherical scatterers in a homogeneous 3D background, a formalism for solving the Lippmann-Schwinger equation. The electric field is expanded on an orthonormal set of basis functions, and a matrix equation for the associated expansion coefficients is developed. The related Green's tensor matrix elements are expressed, which includes a number of technical details, and the field outside the scatterers is expressed. Three different types of background fields, that we use in the following chapters, are introduced, and explicit expressions for the cross sections, in the specific geometry, are presented. Finally, a section on the dipole approximation for solving the Lippmann-Schwinger equation in the limit of small scatterers concludes the chapter.

3.1 Geometry

The specific geometry to be analyzed in the rest of this work is a homogeneous bulk, with permittivity ϵ_{B}, in which we place N spherical scatterers with constant, but possibly frequency dependent permittivities $\epsilon_j, j = 1, 2, \ldots, N$. An arbitrary example with three scatterers is shown in Fig. 3.1 where the global coordinate axes are indicated in black,

and the three sets of local coordinate axes are indicated in blue. The jth scatterer is centered at $\mathbf{r}_j^0$ and has radius R_j.

In the context of N homogeneous scatterers, we may rewrite the Lippmann-Schwinger equation, Eq. (2.17), as follows

$$\mathbf{E}(\mathbf{r}) = \mathbf{E}_{\mathrm{B}}(\mathbf{r}) + k_0^2 \sum_{j'=1}^{N} \Delta\epsilon_{j'} \int_{V_{j'}-\delta V_{j'}} \mathbf{G}_{\mathrm{B}}(\mathbf{r},\mathbf{r}')\mathbf{E}(\mathbf{r}')\,\mathrm{d}\mathbf{r}' - \frac{\Delta\epsilon(\mathbf{r})}{\epsilon_{\mathrm{B}}}\mathbf{L}\mathbf{E}(\mathbf{r}). \tag{3.1}$$

In the following sections, we expand the electric field inside the N scatterers and convert the above equation into a matrix equation for the expansions coefficients.

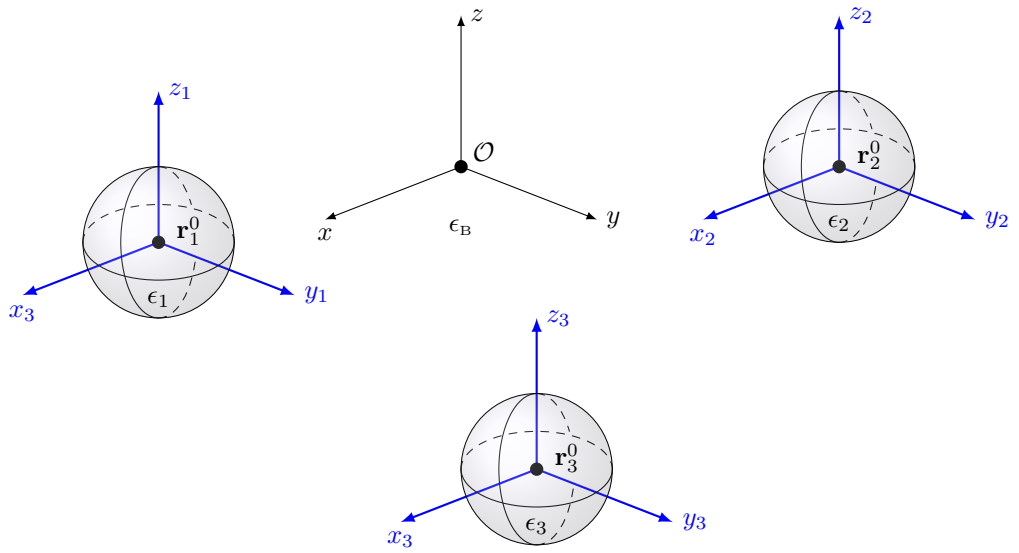

Figure 3.1 Sketch of a homogeneous background material with permittivity ϵ_{B}, in which $N = 3$ spherical scatterers, with permittivities $\epsilon_j \neq \epsilon_{\mathrm{B}}$, are embedded. The global coordinate axes, (x, y, z), are indicated in black, while the three sets of local coordinate axes, (x_j, y_j, z_j) are indicated in blue. Black dots in the spheres denote the local Origos, $\mathbf{r}_j^0$, with respect to the global Origo, $\mathcal{O}$.

3.2 Matrix Equation

3.2.1 Basis Functions

The simplest choice of basis functions are the so-called pulse basis functions where the scattering regions are discretized in a mesh. The kth basis function then equals unity inside the kth subunit of this mesh and vanishes everywhere else

$$p_k(\mathbf{r}) = \begin{cases} 1 & \mathbf{r} \in \text{subunit } k \\ 0 & \text{otherwise} \end{cases}. \tag{3.2}$$

The expansion coefficients of the field then merely become approximations to the field inside the kth subunit. A disadvantage of the pulse basis expansion is the simple, piecewise constant basis functions since strong variations of the electric field can only be accurately

modeled if the mesh is very fine, that is, if many basis functions are included. This leads to large memory requirements, in particular in 3D, which is a well-known problem from similar finite elements methods. More severe is the fact that pulse basis expansions do not converge properly [33, Chap. 2], and this motivates the introduction of more sophisticated basis functions.

As we shall see below, we define basis functions inside scatterer j in local coordinates, cf. Fig. 3.1. In that context, we in Fig. 3.2 show the coordinate conventions to be applied throughout this work. The global axes and labels are shown in black, while the local coordinates and axes of the jth scatterer are shown in blue. The red vector is $\mathbf{r}_j^0$, while the green vector is an arbitrary vector in the local coordinate system.

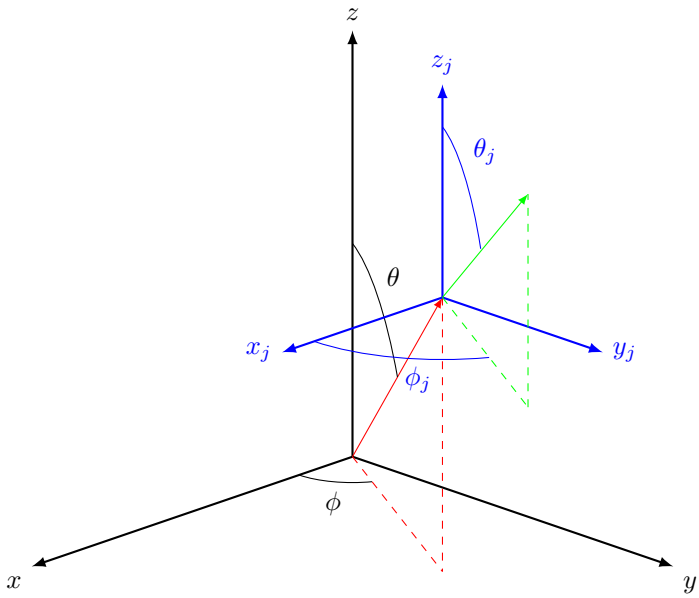

Figure 3.2 Sketch of coordinate conventions: The global coordinates, indicated by black axes and labels, x, y, z, θ and ϕ, and the local coordinates of the jth scatterer, indicated by blue axes and labels, x_j, y_j, z_j, θ_j and ϕ_j. The red vector is the displacement vector from the global Origo to the center of the jth scatterer, $\mathbf{r}_j^0$, while the green vector is an arbitrary vector in the local coordinate system.

We introduce the spherical basis functions of the jth scatterer as follows

$$\psi_{l,m}^j(\mathbf{r}_j) \equiv S_j(\mathbf{r}) N_l^j j_l(k_j r_j) Y_l^m(\theta_j, \phi_j), \qquad l = 0, 1, \ldots, \; -l \leq m \leq l, \tag{3.3}$$

where $\mathbf{r}_j \equiv \mathbf{r} - \mathbf{r}_j^0$ is the local coordinate with local spherical coordinates (r_j, θ_j, ϕ_j) and $k_j \equiv k_0\sqrt{\epsilon_j}$. The functions $j_l(k_j r_j)$ and $Y_l^m(\theta_j, \phi_j)$ are a spherical Bessel function and a normalized spherical harmonic, respectively, defined in Appendices A.1 and A.2, respectively. The function $S_j(\mathbf{r})$ is unity when $\mathbf{r}$ is inside scatterer j and zero otherwise,

$$S_j(\mathbf{r}) \equiv \begin{cases} 1 & r_j \leq R_j \\ 0 & \text{otherwise} \end{cases}, \tag{3.4}$$

which ensures that basis functions of different scatterers are orthogonal by construction. Finally, N_l^j is a radial normalization constant, ensuring that the basis functions in Eq. (3.3) form an orthonormal set.

In analogy with the definition in Eq. (3.3), we introduce the background basis functions

$$\psi_{l,m}^{j,\mathrm{B}}(\mathbf{r}_j) \equiv S_j(\mathbf{r}) N_l^{j,\mathrm{B}} j_l(k_\mathrm{B} r_j) Y_l^m(\theta_j, \phi_j), \quad l = 0, 1, \ldots, \; -l \leq m \leq l, \tag{3.5}$$

that only differ from $\psi_{l,m}^j(\mathbf{r}_j)$ in the radial part where k_j is changed to k_B. N_l^j and $N_l^{j,\mathrm{B}}$ are expressed analytically in Appendix A.3.

The basis functions are so-called regular spherical wavefunctions; They are bounded everywhere and in particular at the Origin

$$j_l(0) = \delta_{0l}. \tag{3.6}$$

As we expect the electric field to be bounded everywhere, they are suitable candidates for expansion of the field. In contrast to this, the scalar Green's function and the Green's tensor, to be introduced formally in Section 3.3.1, diverge at the Origin, and for representing this we introduce the outgoing spherical wavefunctions

$$\varphi_{l,m}^{\mathrm{B}}(\mathbf{r}) \equiv h_l^{(1)}(k_\mathrm{B} r) Y_l^m(\theta, \phi), \tag{3.7}$$

where $h_l^{(1)}(k_\mathrm{B} r_j)$ is a spherical Hankel function of the first kind, defined in Appendix A.1. For later convenience, we also define regular spherical wavefunctions, that are the basis functions from Eqs. (3.3) and (3.5) without the radial normalization

$$\tilde{\psi}_{l,m}^j(\mathbf{r}_j) \equiv \frac{\psi_{l,m}^j(\mathbf{r}_j)}{N_l^j}, \tag{3.8a}$$

$$\tilde{\psi}_{l,m}^{j,\mathrm{B}}(\mathbf{r}_j) \equiv \frac{\psi_{l,m}^{j,\mathrm{B}}(\mathbf{r}_j)}{N_l^{j,\mathrm{B}}}. \tag{3.8b}$$

Function	Definition	Expansion Of
$\psi_{l,m}^j(\mathbf{r}_j)$	Eq. (3.3)	$\mathbf{E}(\mathbf{r}_j)$
$\psi_{l,m}^{j,\mathrm{B}}(\mathbf{r}_j)$	Eq. (3.5)	$\mathbf{E}_\mathrm{B}(\mathbf{r}_j)$
$\varphi_{l,m}^{\mathrm{B}}(\mathbf{r})$	Eq. (3.7)	$\mathbf{G}_\mathrm{B}(\mathbf{r}, \mathbf{r}')$
$\tilde{\psi}_{l,m}^j(\mathbf{r}_j)$	Eq. (3.8a)	$\mathbf{G}_\mathrm{B}(\mathbf{r}, \mathbf{r}')$
$\tilde{\psi}_{l,m}^{j,\mathrm{B}}(\mathbf{r}_j)$	Eq. (3.8b)	$\mathbf{G}_\mathrm{B}(\mathbf{r}, \mathbf{r}')$

Table 1 Overview of basis functions and spherical wavefunctions.

We use the above functions extensively in the rest of this chapter, and an overview is provided in Table 1. All of these functions contain the normalized spherical harmonics, $Y_l^m(\theta, \phi)$, and the orthonormality of these functions (Eq. (A.4)) is a crucial building block in the rest of this chapter.

With $f(\mathbf{r}) \equiv f(r) Y_l^m(\theta, \phi)$ being any of the introduced functions, we define the complex conjugation of this function in the spherical harmonic only

$$\{f(\mathbf{r})\}^{Y^*} \equiv f(r) \{Y_l^m(\theta, \phi)\}^*. \tag{3.9}$$

This may seem cumbersome, but when we consider metallic scatterers, the wave numbers inside these, k_j, become complex which renders the radial parts of the basis functions,

$j_l(k_\mathrm{B} r_j)$, complex, and it is important that these are not complex conjugated. We then introduce the following inner product

$$\langle f|g\rangle \equiv \int \{f(\mathbf{r})\}^{Y^*} g(\mathbf{r})\,\mathrm{d}\mathbf{r}, \tag{3.10}$$

and have

$$\langle \psi^j_{l,m}|\psi^{j'}_{l',m'}\rangle = \delta_{jj'}\delta_{ll'}\delta_{mm'}, \tag{3.11a}$$

$$\langle \psi^{j,\mathrm{B}}_{l,m}|\psi^{j',\mathrm{B}}_{l',m'}\rangle = \delta_{jj'}\delta_{ll'}\delta_{mm'}, \tag{3.11b}$$

$$\langle \psi^{j}_{l,m}|\psi^{j',\mathrm{B}}_{l',m'}\rangle = M^j_l\delta_{jj'}\delta_{ll'}\delta_{mm'}, \tag{3.11c}$$

where M^j_l is expressed in Appendix A.4. Many times in this chapter, we encounter integrals of the form in Eqs. (3.11), and these relations consequently play a central role.

We shall often sum over all basis functions or wavefunctions, and we therefore introduce the following shorthand notation for the double sum over their indices

$$\sum_{l,m} \equiv \sum_{l=0}^{\infty}\sum_{m=-l}^{l}. \tag{3.12}$$

We have in this section introduced the basis functions of the jth scatterer and of the background material. In the following section, we expand the electric field, $\mathbf{E}$, and the background field, $\mathbf{E}_\mathrm{B}$, on these, respectively, and employ the expansions in the Lippmann-Schwinger equation.

3.2.2 Expansion of Electric Field

As discussed earlier, the Lippmann-Schwinger equation is an implicit equation for the field inside the scatterers, and when the field in these regions has been determined, it is explicit for the field outside the scatterers. We therefore focus on the field inside the jth scatterer and expand this and the background field as follows

$$\boxed{\mathbf{E}(\mathbf{r}_j) = \sum_\alpha\sum_{l,m} e_{j\alpha lm}\psi^j_{l,m}(\mathbf{r}_j)\,\mathbf{e}_\alpha,} \tag{3.13a}$$

$$\boxed{\mathbf{E}_\mathrm{B}(\mathbf{r}_j) = \sum_\alpha\sum_{l,m} e^\mathrm{B}_{j\alpha lm}\psi^{j,\mathrm{B}}_{l,m}(\mathbf{r}_j)\,\mathbf{e}_\alpha,} \tag{3.13b}$$

where $\alpha \in \{x, y, z\}$ denotes one of the three Cartesian components.

In practice, the expansions are truncated at some finite number of basis functions which we do by truncating the l-sums for each scatterer at l_max

$$\mathbf{E}(\mathbf{r}_j) = \sum_\alpha\sum_{l=0}^{\infty}\sum_{m=-l}^{l} e_{j\alpha lm}\psi^j_{l,m}(\mathbf{r}_j)\,\mathbf{e}_\alpha \simeq \sum_\alpha\sum_{l=0}^{l_\mathrm{max}}\sum_{m=-l}^{l} e_{j\alpha lm}\psi^j_{l,m}(\mathbf{r}_j)\,\mathbf{e}_\alpha, \tag{3.13a$'$}$$

$$\mathbf{E}_\mathrm{B}(\mathbf{r}_j) = \sum_\alpha\sum_{l=0}^{\infty}\sum_{m=-l}^{l} e^\mathrm{B}_{j\alpha lm}\psi^{j,\mathrm{B}}_{l,m}(\mathbf{r}_j)\,\mathbf{e}_\alpha \simeq \sum_\alpha\sum_{l=0}^{l_\mathrm{max}}\sum_{m=-l}^{l} e^\mathrm{B}_{j\alpha lm}\psi^{j,\mathrm{B}}_{l,m}(\mathbf{r}_j)\,\mathbf{e}_\alpha. \tag{3.13b$'$}$$

The field inside scatterer j is then expanded on a total of

$$K_j = 3\sum_{l=0}^{l_\mathrm{max}}(2l+1) = 3\,(l_\mathrm{max}+1)^2, \tag{3.14}$$

basis functions, where the factor 3 stems from the three polarizations. As we shall see, the truncation introduced in Eqs. (3.13a′)-(3.13b′) is the only approximation in the formalism, and we in the next chapter analyze what values of $l_{\max}$ are needed to obtain convergence in the computations.

3.2.3 Matrix Equation for Expansion Coefficients

Inserting the expansions in Eqs. (3.13a)-(3.13b) into the Lippmann-Schwinger equation, Eq. (3.1), we in Appendix C.1 derive the following matrix equation for the expansion coefficients of the field

$$\left(\mathbf{I} + \frac{L}{\epsilon_{\mathrm{B}}}\boldsymbol{\Delta\epsilon}\right)\mathbf{e} = \mathbf{M}_{\mathrm{B}}\mathbf{e}_{\mathrm{B}} + k_0^2\mathbf{G}\boldsymbol{\Delta\epsilon}\mathbf{e}, \tag{3.15}$$

where $\mathbf{e}$ ($\mathbf{e}_{\mathrm{B}}$) contains the expansion coefficients of the field (background field). This equation is solved for $\mathbf{e}$ to give the expansion coefficients of the electric field explicitly

$$\boxed{\mathbf{e} = \left(\mathbf{I} + \frac{L}{\epsilon_{\mathrm{B}}}\boldsymbol{\Delta\epsilon} - k_0^2\mathbf{G}\boldsymbol{\Delta\epsilon}\right)^{-1}\mathbf{M}_{\mathrm{B}}\mathbf{e}_{\mathrm{B}}.} \tag{3.16}$$

This result together with the expansion in Eq. (3.13a) is the main result of this chapter; It holds the solution of the implicit Lippmann-Schwinger equation. What remains is evaluation of the matrices in the above equation, and we focus on this in the following sections.

The vectors and matrices in Eq. (3.16) acquire finite dimensions when we impose the truncations from Eqs. (3.13a′)-(3.13b′). In the same equation, $L = 1/3$ is the diagonal elements of the source dyadic, $\mathbf{L}$, and $\boldsymbol{\Delta\epsilon}$ and $\mathbf{M}_{\mathrm{B}}$ are diagonal matrices whose elements are given in Appendix C.1.

The Green's tensor matrix, $\mathbf{G}$, is non-diagonal in all indices; It accounts for the coupling between $e_{j'\alpha'l'm'}$ and $e_{j\alpha lm}$. This matrix, that can be decomposed into submatrices as shown in Eqs. (C.6c) in Appendix C.1, has elements of the form

$$\left[\mathbf{G}_{j,j'}^{\alpha\alpha'}\right]_{l,l'}^{m,m'} \equiv \int_{V_j}\int_{V_{j'}-\delta V_{j'}} \{\psi_{l,m}^{j}(\mathbf{r}_j)\}^{Y^*}\mathbf{G}_{\mathrm{B}}^{\alpha\alpha'}(\mathbf{r}_j,\mathbf{r}'_{j'})\psi_{l',m'}^{j'}(\mathbf{r}_{j'})\,\mathrm{d}\mathbf{r}'_{j'}\,\mathrm{d}\mathbf{r}_j. \tag{3.17}$$

As we see in Eq. (3.16), the terms from the Green's tensor matrix and the source dyadic matrix are multiplied by the dielectric contrast matrix, $\boldsymbol{\Delta\epsilon}$; These coupling terms vanish if all $\Delta\epsilon_j \equiv \epsilon_j - \epsilon_{\mathrm{B}} = 0$, that is, in the absence of scatterers $\mathbf{e} = \mathbf{M}_{\mathrm{B}}\mathbf{e}_{\mathrm{B}}$, as expected.

3.3 Green's Tensor Matrix

In the following sections, we derive expressions for the elements of the Green's tensor matrix. The scope is to introduce the techniques used for evaluating the matrix elements, which, however, does involve a number of technicalities. In turn, we only present generic expressions for the matrix elements, while the detailed expressions, that are rather comprehensive, are given in appendices.

As discussed earlier, the integrals involving the Green's tensor must be evaluated as Principal values, that is, the singularity at $\mathbf{r} = \mathbf{r}'$ must be avoided. By the definition of the matrix elements, the Principal value only needs to be applied when $j = j'$ in which case the $\mathbf{r}_j$- and the $\mathbf{r}'_{j'}$-integrations are performed on the same scatterer. Consequently,

we in the following distinguish between the cases when $j \neq j'$ (scattering terms) and when $j = j'$ (self terms). In both cases, we will need representations of the Green's tensor that are suitable for performing the integrations in the local coordinate systems, and we therefore first review the scalar Green's function and the Green's tensor. In the following sections, Ref. [34, Chap. 3] is used when nothing else is stated.

3.3.1 Scalar Green's Function and Green's Tensor

The electromagnetic Green's tensor for a homogeneous 3D space can be expressed as follows [24, Chap. 2]

$$\mathbf{G}_{\mathrm{B}}(\mathbf{r},\mathbf{r}') = \left(\mathbf{I} + \frac{1}{k_{\mathrm{B}}^2}\nabla\nabla^T\right) g_{\mathrm{B}}(\mathbf{r},\mathbf{r}'), \tag{3.18a}$$

$$g_{\mathrm{B}}(\mathbf{r},\mathbf{r}') = g_{\mathrm{B}}(\mathbf{r}',\mathbf{r}) = g_{\mathrm{B}}(\mathbf{R}) = \frac{\exp(ik_{\mathrm{B}}|\mathbf{R}|)}{4\pi|\mathbf{R}|}, \tag{3.18b}$$

where $g_{\mathrm{B}}(\mathbf{r},\mathbf{r}')$ is the scalar Green's function, and where $\mathbf{R} = \mathbf{r} - \mathbf{r}'$. Since $g_{\mathrm{B}}(\mathbf{R})$ only depends on the length of $\mathbf{R}$, the first two equalities in Eq. (3.18b) follow immediately. Likewise, the fact that $g_{\mathrm{B}}(\mathbf{R})$ only depends on $|\mathbf{R}|$ implies that we can, at our convenience, define $\mathbf{R}' = \mathbf{r}' - \mathbf{r}$ and then have $g_{\mathrm{B}}(\mathbf{R}) = g_{\mathrm{B}}(\mathbf{R}')$. These facts will be exploited to express the different types of matrix elements.

The elements of the Green's tensor can be expressed explicitly as follows

$$\mathbf{G}_{\mathrm{B}}^{\alpha\alpha'}(\mathbf{r},\mathbf{r}') = \left(\delta_{\alpha\,\alpha'} + \frac{1}{k_{\mathrm{B}}^2}\partial_\alpha\partial_{\alpha'}\right) g_{\mathrm{B}}(\mathbf{r},\mathbf{r}'), \tag{3.19}$$

where ∂_α is shorthand notation for the partial derivative with respect to $\alpha \in \{x, y, z\}$, $\partial_\alpha \equiv \partial/\partial_\alpha$. The differential operator should act on $\mathbf{R}$ if $\mathbf{r}$ and $\mathbf{r}'$ vary simultaneously, while it can act on $\mathbf{r}'$ for fixed $\mathbf{r}$ and vice versa. By the form in Eq. (3.19), we see that the Green's tensor is symmetric, since $\partial_\alpha\partial_{\alpha'} = \partial_{\alpha'}\partial_\alpha$

$$\mathbf{G}_{\mathrm{B}}^{\alpha\alpha'}(\mathbf{r},\mathbf{r}') = \mathbf{G}_{\mathrm{B}}^{\alpha'\alpha}(\mathbf{r},\mathbf{r}'), \tag{3.20}$$

and it consequently only has six independent components.

With reference to the outgoing spherical wavefunctions, $\varphi_{l,m}^{\mathrm{B}}(\mathbf{r})$, introduced in Eq. (3.7), the scalar Green's function can be written in the following way

$$g_{\mathrm{B}}(\mathbf{r},\mathbf{r}') = \frac{ik_{\mathrm{B}}}{\sqrt{4\pi}}\varphi_{0,0}^{\mathrm{B}}(\mathbf{R}). \tag{3.21}$$

In the following sections, we compute the matrix elements, Eq. (3.17), and to do this analytically various expansions of the scalar Green's function will play an important role.

3.3.2 Scattering Terms

In this section, we are concerned with expressing the matrix elements $\left[\mathbf{G}_{j,j'}^{\alpha\alpha'}\right]_{l,l'}^{m,m'}$ where $j \neq j'$. In this case, by construction, $\mathbf{r} \neq \mathbf{r}'$, and we thus do not cross the singularity of the Green's tensor at $\mathbf{r} = \mathbf{r}'$.

As discussed in the previous section, the Green's tensor depends on the displacement between $\mathbf{r}$ and $\mathbf{r}'$, and to perform the integration over $\mathbf{r}'$ on scatterer j' and the integration

over $\mathbf{r}$ on scatterer j analytically, we need an expansion of the Green's tensor that will allow this.

The sketches in this and the following section convey simple, geometric considerations and are for that reason done in 2D, but we keep in mind that the scatterers are spheres in 3D.

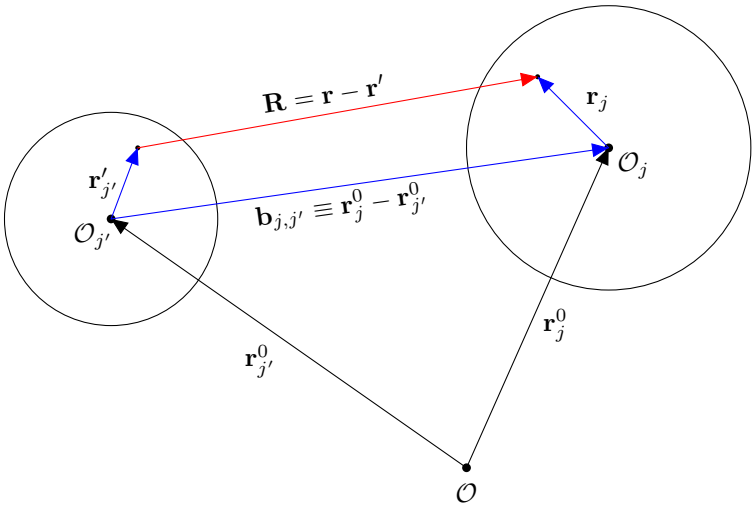

Figure 3.3 Two scatterers, j and j', sketched in 2D. The centers of the scatterers, $\mathbf{r}^0_j$ and $\mathbf{r}^0_{j'}$, and two arbitrary local points inside the scatterers, $\mathbf{r}_j$ and $\mathbf{r}'_{j'}$, are indicated. Likewise, the displacements between the two points, $\mathbf{R}$, and between the centers of the scatterers, $\mathbf{b}_{j,j'}$, are shown.

We sketch two scatterers, j and j', in Fig. 3.3. In the figure, we introduced the displacement vector between the centers of the two scatterers, $\mathbf{b}_{j,j'}$, which we henceforth simply term $\mathbf{b}$. As discussed above, the Green's tensor only depends on the displacement between $\mathbf{r}$ and $\mathbf{r}'$ (indicated by the red vector in the figure), and we see that we may express this vector using the three blue vectors in the figure

$$\mathbf{R} = \mathbf{r} - \mathbf{r}' = \mathbf{r}_j + \mathbf{b} - \mathbf{r}'_{j'}. \tag{3.22}$$

This decomposition of $\mathbf{R}$ into local coordinates on scatterers j and j' is convenient because it subsequently allows us to expand the scalar Green's function, $g_{\mathrm{B}}(\mathbf{R})$, on the background regular spherical wavefunctions of the two scatterers. This is done using a so-called two-center expansion

$$g_{\mathrm{B}}(\mathbf{R}) = ik_{\mathrm{B}} \sum_{p,t} \sum_{\nu,\mu} S^{t,\mu}_{p,\nu}(\mathbf{b}) \{\tilde{\psi}^{j',\mathrm{B}}_{p,t}(\mathbf{r}'_{j'})\}^{Y^*} \tilde{\psi}^{j,\mathrm{B}}_{\nu,\mu}(\mathbf{r}_j), \tag{3.23}$$

where the separation matrix, $S^{t,\mu}_{p,\nu}(\mathbf{b})$, is defined in Appendix B.1. We recall that the functions $\tilde{\psi}^{j,\mathrm{B}}_{\nu,\mu}(\mathbf{r}_j)$ and $\tilde{\psi}^{j',\mathrm{B}}_{p,t}(\mathbf{r}'_{j'})$, defined in Eq. (3.8b), are merely scaled versions of the background basis functions, $\psi^{j,\mathrm{B}}_{\nu,\mu}(\mathbf{r}_j)$ and $\psi^{j',\mathrm{B}}_{p,t}(\mathbf{r}'_{j'})$, and consequently the orthogonality relation in Eq. (3.11c) will prove useful as we shall see below.

The elements of the Green's tensor can now be expressed by combining Eqs. (3.19) and (3.23)

$$\mathbf{G}_{\mathrm{B}}^{\alpha\alpha'}(\mathbf{r},\mathbf{r}') = \left(\delta_{\alpha\,\alpha'} + \frac{1}{k_{\mathrm{B}}^2}\partial_\alpha\partial_{\alpha'}\right)\left\{ik_{\mathrm{B}}\sum_{p,t}\sum_{\nu,\mu} S_{p,\nu}^{t,\mu}(\mathbf{b})\{\tilde{\psi}_{p,t}^{j',\mathrm{B}}(\mathbf{r}'_{j'})\}^{Y^*}\tilde{\psi}_{\nu,\mu}^{j,\mathrm{B}}(\mathbf{r}_j)\right\}, \quad (3.24a)$$

where we for all scattering terms, at our convenience, choose to act the differential operators on the wavefunctions of scatterer j, namely

$$\mathbf{G}_{\mathrm{B}}^{\alpha\alpha'}(\mathbf{r},\mathbf{r}') = ik_{\mathrm{B}}\sum_{p,t}\sum_{\nu,\mu} S_{p,\nu}^{t,\mu}(\mathbf{b})\{\tilde{\psi}_{p,t}^{j',\mathrm{B}}(\mathbf{r}'_{j'})\}^{Y^*}\left(\delta_{\alpha\,\alpha'} + \frac{1}{k_{\mathrm{B}}^2}\partial_\alpha\partial_{\alpha'}\right)\tilde{\psi}_{\nu,\mu}^{j,\mathrm{B}}(\mathbf{r}_j). \quad (3.24b)$$

What remains to express the scattering matrix elements is the result of acing the double partial derivative operator $\partial_\alpha\partial_{\alpha'}$ on $\tilde{\psi}_{\nu,\mu}^{j,\mathrm{B}}(\mathbf{r}_j)$. This may be written as a sum of other spherical wavefunctions which we express symbolically as follows

$$\partial_\alpha\partial_{\alpha'}\tilde{\psi}_{\nu,\mu}^{j,\mathrm{B}}(\mathbf{r}_j) = \sum_{\gamma_{\alpha,\alpha'}} g_{\gamma_{\alpha,\alpha'}}\tilde{\psi}_{\nu(\gamma_{\alpha,\alpha'}),\mu(\gamma_{\alpha,\alpha'})}^{j,\mathrm{B}}(\mathbf{r}_j), \quad (3.25)$$

where $\nu(\gamma_{\alpha,\alpha'}) \equiv \nu + \gamma'_{\alpha,\alpha'}$ and $\mu(\gamma_{\alpha,\alpha'}) \equiv \mu + \gamma''_{\alpha,\alpha'}$, with $\gamma'_{\alpha,\alpha'}$ and $\gamma''_{\alpha,\alpha'}$ being integers. We note that the sums are finite, containing between one and nine terms depending on α, α', ν and μ. The specific expressions for the different double derivatives are presented in Appendix A.5. Combining the representation of the elements of the Green's tensor in Eq. (3.24b) with Eq. (3.25), we finally have a form of the matrix elements that is suitable for performing the integrations on scatterers j and j' analytically

$$\begin{aligned}\mathbf{G}_{\mathrm{B}}^{\alpha\alpha'}(\mathbf{r},\mathbf{r}') = ik_{\mathrm{B}}&\sum_{p,t}\sum_{\nu,\mu} S_{p,\nu}^{t,\mu}(\mathbf{b})\{\tilde{\psi}_{p,t}^{j',\mathrm{B}}(\mathbf{r}'_{j'})\}^{Y^*} \\ &\times\left(\delta_{\alpha\,\alpha'}\tilde{\psi}_{\nu,\mu}^{j,\mathrm{B}}(\mathbf{r}_j) + \frac{1}{k_{\mathrm{B}}^2}\sum_{\gamma_{\alpha,\alpha'}} g_{\gamma_{\alpha,\alpha'}}\tilde{\psi}_{\nu(\gamma_{\alpha,\alpha'}),\mu(\gamma_{\alpha,\alpha'})}^{j,\mathrm{B}}(\mathbf{r}_j)\right). \quad (3.26)\end{aligned}$$

We then compute the matrix elements, as defined in Eq. (3.17), using the inner products of Eqs. (3.11)

$$\begin{aligned}\left[\mathbf{G}_{j,j'}^{\alpha\alpha'}\right]_{l,l'}^{m,m'} = ik_{\mathrm{B}}&\sum_{p,t}\sum_{\nu,\mu} S_{p,\nu}^{t,\mu}(\mathbf{b})\langle\tilde{\psi}_{p,t}^{j',\mathrm{B}}|\psi_{l',m'}^{j'}\rangle \\ &\times\left(\delta_{\alpha\,\alpha'}\langle\psi_{l,m}^{j}|\tilde{\psi}_{\nu,\mu}^{j,\mathrm{B}}\rangle + \frac{1}{k_{\mathrm{B}}^2}\sum_{\gamma_{\alpha,\alpha'}} g_{\gamma_{\alpha,\alpha'}}\langle\psi_{l,m}^{j}|\tilde{\psi}_{\nu(\gamma_{\alpha,\alpha'}),\mu(\gamma_{\alpha,\alpha'})}^{j,\mathrm{B}}\rangle\right), \quad (3.27)\end{aligned}$$

which finally becomes

$$\boxed{\begin{aligned}\left[\mathbf{G}_{j,j'}^{\alpha\alpha'}\right]_{l,l'}^{m,m'} &= ik_{\mathrm{B}}M_{l'}^{j'}M_{l}^{j}\Big/\left(N_{l'}^{j',\mathrm{B}}N_{l}^{j,\mathrm{B}}\right) \\ &\times\left(\delta_{\alpha\,\alpha'}S_{l',l}^{m',m}(\mathbf{b}) + \frac{1}{k_{\mathrm{B}}^2}\sum_{\gamma_{\alpha,\alpha'}} g_{\gamma_{\alpha,\alpha'}}S_{l',l-\gamma'_{\alpha,\alpha'}}^{m',m-\gamma''_{\alpha,\alpha'}}(\mathbf{b})\right). \quad (3.28)\end{aligned}}$$

The above is a generic scattering matrix element, and we in Appendix B.2 present explicit expressions for all permutations of the polarizations, α and α'. We also note that the g-coefficients, introduced in Eq. (3.25), depend on the wavefunction indices, ν and μ, but we have for brevity suppressed them above; The details are given in the aforementioned appendix.

In the next section, we are concerned with expressing the self terms of the Green's tensor matrix, corresponding to $j = j'$.

3.3.3 Self Terms

The self terms are the matrix elements, Eq. (3.17), with $j = j'$, i.e., the $\mathbf{r}'$- and $\mathbf{r}$-integrations are both carried out on scatterer j. This means that the $\mathbf{r}'$-integral must be evaluated as a Principal value, by imposing a small Principal volume at $\mathbf{r}$ around which the $\mathbf{r}'$-integration is carried out. We choose a spherical Principal volume and sketch the situation in Fig. 3.4.

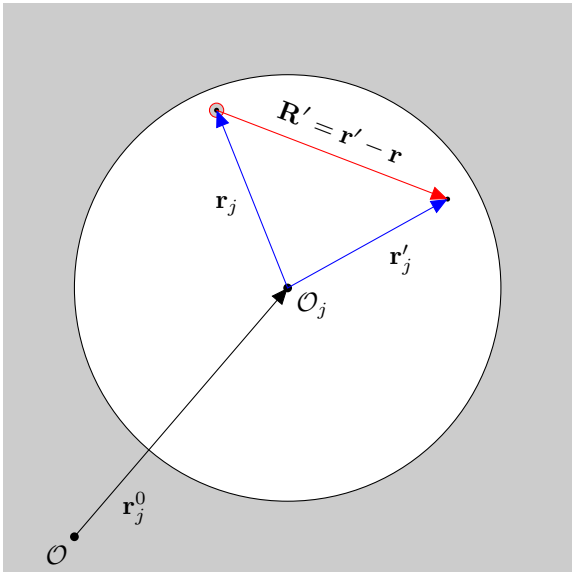

Figure 3.4 One scatterer, j, sketched in 2D. The center of the scatterer, $\mathbf{r}_j^0$, and two arbitrary local points inside the scatterer, $\mathbf{r}_j$ and $\mathbf{r}'_j$, are indicated. Likewise, the displacement between the two points, $\mathbf{R}'$, and the Principal volume (small red circle) are shown. Gray color indicates volumes that are *not* included in the $\mathbf{r}'$-integration.

In the figure, two arbitrary points inside scatterer j, $\mathbf{r}_j$ and $\mathbf{r}'_j$, are shown (blue vectors), and the displacement vector from the former to the latter, $\mathbf{R}'$, is also indicated (red vector). The Principal volume, centered at $\mathbf{r}_j$, is schematically shown as a small red circle, and in this and the following figure gray indicates volumes that are *not* included in the $\mathbf{r}'$-integration. We then need to perform the $\mathbf{r}'$-integration around this small exclusion volume for all arbitrary $\mathbf{r}$, and with the ambition of doing this analytically we proceed as done in the 2D case in Ref. [18]: We split the $\mathbf{r}'$-integration into a part over all space, $\mathbb{R}^3$, minus the Principal volume (A) minus an integration over all space minus the scatterer volume (B)

$$\left[\mathbf{G}_{j,j}^{\alpha\alpha'}\right]_{l,l'}^{m,m'} = \left[A_{j,j}^{\alpha\alpha'}\right]_{l,l'}^{m,m'} - \left[B_{j,j}^{\alpha\alpha'}\right]_{l,l'}^{m,m'}, \tag{3.29}$$

where

$$\left[A_{j,j}^{\alpha\alpha'}\right]_{l,l'}^{m,m'} \equiv \int_{V_j}\int_{\mathbb{R}^3-\delta V_j} \{\psi_{l,m}^j(\mathbf{r}_j)\}^{Y^*} \mathbf{G}_{\mathrm{B}}^{\alpha\alpha'}(\mathbf{r}_j,\mathbf{r}'_j)\psi_{l',m'}^j(\mathbf{r}'_j)\,\mathrm{d}\mathbf{r}'_j\,\mathrm{d}\mathbf{r}_j, \tag{3.30a}$$

$$\left[B_{j,j}^{\alpha\alpha'}\right]_{l,l'}^{m,m'} \equiv \int_{V_j}\int_{\mathbb{R}^3-V_j} \{\psi_{l,m}^j(\mathbf{r}_j)\}^{Y^*} \mathbf{G}_{\mathrm{B}}^{\alpha\alpha'}(\mathbf{r}_j,\mathbf{r}'_j)\psi_{l',m'}^j(\mathbf{r}'_j)\,\mathrm{d}\mathbf{r}'_j\,\mathrm{d}\mathbf{r}_j. \tag{3.30b}$$

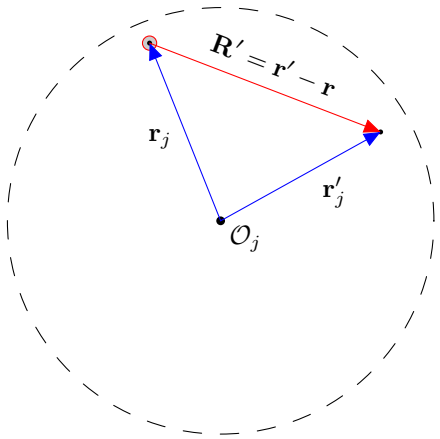

(a) Integration domain for the A-part of the matrix element, extending over all space minus the Principal volume.

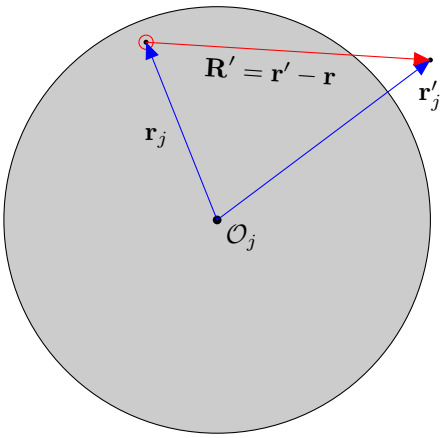

(b) Integration domain for the B-part of the matrix element, extending over all space minus the scatterer volume.

Figure 3.5 The two $\mathbf{r}'$-integration domains for expressing the $j = j'$ Green's tensor matrix elements. The left minus the right integration domain produces the original integration domain, see Fig. 3.4. Gray color indicates volumes that are *not* included in the $\mathbf{r}'$-integration.

These two integration domains are sketched in Figs. 3.5(a) and 3.5(b), respectively. In Fig. 3.5(a), the scatterer boundary is dashed as it is, in principle, not present for the A-integrations. Note that we omit the global Origo in these figures for simplicity.

In the following sections, we discuss the A- and B-integrals further, but we already here note that the splitting is only a convenient way of circumventing the singularity of the Green's tensor at $\mathbf{r} = \mathbf{r}'$. By the definitions of the basis functions, Eqs. (3.3) and (3.5), these vanish outside the scatterers, so to render the integrations outside the scatterers non-trivial we in the following sections relax this constraint; We employ the same definitions as in the aforementioned equations, but without the compact support function $S_j(\mathbf{r})$. This is allowable since the integration outside the scatterer is virtual in the sense that we compute the integral (A) and subtract it again (B).

A-Integrals

In the A-integrals, we may equally well integrate $\mathbf{R}'$ as $\mathbf{r}'_j$ over all space, and while the exclusion of the Principal volume upon integrating over the latter is tricky, and in practice infeasible, this is straightforward when integrating over the former: The radial part of the integral is truncated at some positive infinitesimal, $\delta R'$, and the limit $\delta R' \to 0$ is subsequently expressed. The Green's tensor depends only on $\mathbf{R}'$ (see the discussion after Eqs. (3.18)), but $\psi^j_{l',m'}(\mathbf{r}'_j)$ is defined with respect to the local Origo, $\mathcal{O}_j$, so we need an

expansion of this function around $\mathbf{r}_j$

$$\psi^j_{l',m'}(\mathbf{r}'_j) = N^j_{l'} \sum_{\nu,\mu} (-1)^\mu \hat{S}^{m',\mu}_{l',\nu}(\mathbf{r}_j) \{\tilde{\psi}^j_{\nu,-\mu}(\mathbf{R}')\}^{Y^*}, \tag{3.31}$$

where a new type of separation matrix, $\hat{S}^{m',\mu}_{l',\nu}(\mathbf{r}_j)$, defined in Appendix B.1, is applied. The scalar Green's function, $g_{\mathrm{B}}(\mathbf{R}')$, may be expressed as an outgoing spherical background wavefunction, see Eq. (3.21), which is convenient because the Cartesian partial derivatives of this function are expressed in Appendix A.5

$$\partial_\alpha \partial_{\alpha'} g_{\mathrm{B}}(\mathbf{R}') = \frac{ik_{\mathrm{B}}}{\sqrt{4\pi}} \partial_\alpha \partial_{\alpha'} \varphi^{\mathrm{B}}_{0,0}(\mathbf{R}') = \frac{ik_{\mathrm{B}}}{\sqrt{4\pi}} \sum_{\gamma_{\alpha,\alpha'}} g_{\gamma_{\alpha,\alpha'}} \varphi^{\mathrm{B}}_{\gamma'_{\alpha,\alpha'},\gamma''_{\alpha,\alpha'}}(\mathbf{R}'). \tag{3.32}$$

As compared to the general expression of Eq. (3.25), we have used that $\nu(\gamma_{\alpha,\alpha'}) = 0 + \gamma'_{\alpha,\alpha'}$ and $\mu(\gamma_{\alpha,\alpha'}) = 0 + \gamma''_{\alpha,\alpha'}$. The elements of the Green's tensor for expressing the A-integrals then are

$$\mathbf{G}^{\alpha\alpha'}_{\mathrm{B}}(\mathbf{r},\mathbf{r}') = \frac{ik_{\mathrm{B}}}{\sqrt{4\pi}} \left(\delta_{\alpha\,\alpha'} \varphi^{\mathrm{B}}_{0,0}(\mathbf{R}') + \frac{1}{k^2_{\mathrm{B}}} \sum_{\gamma_{\alpha,\alpha'}} g_{\gamma_{\alpha,\alpha'}} \varphi^{\mathrm{B}}_{\gamma'_{\alpha,\alpha'},\gamma''_{\alpha,\alpha'}}(\mathbf{R}') \right), \tag{3.33}$$

and the integrals become

$$\begin{aligned}
\left[A^{\alpha\alpha'}_{j,j}\right]^{m,m'}_{l,l'} &= \int_{V_j} \int_{\mathbb{R}^3 - \delta V_j} \{\psi^j_{l,m}(\mathbf{r}_j)\}^{Y^*} \frac{ik_{\mathrm{B}}}{\sqrt{4\pi}} \Bigg(\delta_{\alpha\,\alpha'} \varphi^{\mathrm{B}}_{0,0}(\mathbf{R}') \\
&\quad + \frac{1}{k^2_{\mathrm{B}}} \sum_{\gamma_{\alpha,\alpha'}} g_{\gamma_{\alpha,\alpha'}} \varphi^{\mathrm{B}}_{\gamma'_{\alpha,\alpha'},\gamma''_{\alpha,\alpha'}}(\mathbf{R}') \Bigg) \\
&\quad \times N^j_{l'} \sum_{\nu,\mu} (-1)^\mu \hat{S}^{m',\mu}_{l',\nu}(\mathbf{r}_j) \{\tilde{\psi}^j_{\nu,-\mu}(\mathbf{R}')\}^{Y^*} \, \mathrm{d}\mathbf{R}' \, \mathrm{d}\mathbf{r}_j \\
&= \frac{ik_{\mathrm{B}}}{\sqrt{4\pi}} N^j_{l'} \int_{V_j} \{\psi^j_{l,m}(\mathbf{r}_j)\}^{Y^*} \Bigg(\delta_{\alpha\,\alpha'} \hat{S}^{m',0}_{l',0}(\mathbf{r}_j) I^{\mathbb{R}^3 - \delta V_j}_0 \\
&\quad + \frac{1}{k^2_{\mathrm{B}}} \sum_{\gamma_{\alpha,\alpha'}} g_{\gamma_{\alpha,\alpha'}} (-1)^{\gamma''_{\alpha,\alpha'}} \hat{S}^{m',-\gamma''_{\alpha,\alpha'}}_{l',\gamma'_{\alpha,\alpha'}}(\mathbf{r}_j) I^{\mathbb{R}^3 - \delta V_j}_{\gamma'_{\alpha,\alpha'}} \Bigg) \, \mathrm{d}\mathbf{r}_j,
\end{aligned} \tag{3.34}$$

where the integral $I^{\mathbb{R}^3 - \delta V_j}_l$ is defined and expressed in Appendix B.3. Finally, a generic matrix element is

$$\boxed{\begin{aligned}
\left[A^{\alpha\alpha'}_{j,j}\right]^{m,m'}_{l,l'} &= \frac{ik_{\mathrm{B}}}{\sqrt{4\pi}} N^j_{l'} \Bigg(\delta_{\alpha\,\alpha'} \langle \psi^j_{l,m} | \hat{S}^{m',0}_{l',0} \rangle I^{\mathbb{R}^3 - \delta V_j}_0 \\
&\quad + \frac{1}{k^2_{\mathrm{B}}} \sum_{\gamma_{\alpha,\alpha'}} g_{\gamma_{\alpha,\alpha'}} (-1)^{\gamma''_{\alpha,\alpha'}} \langle \psi^j_{l,m} | \hat{S}^{m',-\gamma''_{\alpha,\alpha'}}_{l',\gamma'_{\alpha,\alpha'}} \rangle I^{\mathbb{R}^3 - \delta V_j}_{\gamma'_{\alpha,\alpha'}} \Bigg).
\end{aligned}} \tag{3.35}$$

As can be seen in Appendix B.1, the separation matrix $\hat{S}^{m',-\gamma''_{\alpha,\alpha'}}_{l',\gamma'_{\alpha,\alpha'}}(\mathbf{r}_j)$ consists of a sum of a finite number of spherical wavefunctions. Consequently, the inner product under the $\gamma_{\alpha,\alpha'}$-sum at most contributes with one term, and due to orthogonality it vanishes for many permutations of the indices. The details and explicit expressions are given in Appendix B.4.

B-Integrals

In the B-integrals, as sketched in Fig. 3.5(b), the $\mathbf{r}'$-integration takes place outside the scatterer, so by construction $\mathbf{r} \neq \mathbf{r}'$. Consequently, we do not have to worry about the singularity of the Green's tensor. In this context, we may express the scalar Green's function as follows

$$g_{\mathrm{B}}(\mathbf{R}') = ik_{\mathrm{B}} \sum_{\nu,\mu} \tilde{\psi}^{j,\mathrm{B}}_{\nu,\mu}(\mathbf{r}_j)\{\varphi^{\mathrm{B}}_{\nu,\mu}(\mathbf{r}'_j)\}^{Y^*}. \tag{3.36}$$

Acting the differential operators on the $\mathbf{r}_j$-dependent wavefunction, a generic element of the Green's tensor, for expressing the B-integrals, becomes

$$\mathbf{G}^{\alpha\alpha'}_{\mathrm{B}}(\mathbf{r},\mathbf{r}') = ik_{\mathrm{B}} \sum_{\nu,\mu} \{\varphi^{\mathrm{B}}_{\nu,\mu}(\mathbf{r}'_j)\}^{Y^*} \left(\delta_{\alpha\,\alpha'} \tilde{\psi}^{j,\mathrm{B}}_{\nu,\mu}(\mathbf{r}_j) + \frac{1}{k^2_{\mathrm{B}}} \sum_{\gamma_{\alpha,\alpha'}} g_{\gamma_{\alpha,\alpha'}} \tilde{\psi}^{j,\mathrm{B}}_{\nu(\gamma_{\alpha,\alpha'}),\mu(\gamma_{\alpha,\alpha'})}(\mathbf{r}_j) \right). \tag{3.37}$$

With this representation at hand, the B-integrals may readily be computed

$$\begin{aligned} \left[B^{\alpha\alpha'}_{j,j}\right]^{m,m'}_{l,l'} &= ik_{\mathrm{B}} \sum_{\nu,\mu} \langle \varphi^{\mathrm{B}}_{\nu,\mu} | \psi^{j}_{l',m'} \rangle_{\mathbb{R}^3 - V_j} \\ &\quad \times \left(\delta_{\alpha\,\alpha'} \langle \psi^{j}_{l,m} | \tilde{\psi}^{j,\mathrm{B}}_{\nu,\mu} \rangle + \frac{1}{k^2_{\mathrm{B}}} \sum_{\gamma_{\alpha,\alpha'}} g_{\gamma_{\alpha,\alpha'}} \langle \psi^{j}_{l,m} | \tilde{\psi}^{j,\mathrm{B}}_{\nu(\gamma_{\alpha,\alpha'}),\mu(\gamma_{\alpha,\alpha'})} \rangle \right), \end{aligned} \tag{3.38}$$

where $\langle \cdot | \cdot \rangle_{\mathbb{R}^3 - V_j}$ denotes an inner product over all space minus the scatterer volume. This may finally be expressed as follows

$$\boxed{\begin{aligned} \left[B^{\alpha\alpha'}_{j,j}\right]^{m,m'}_{l,l'} &= ik_{\mathrm{B}} M^{j}_{l} I^{\mathbb{R}^3 - V_j}_{l'} N^{j}_{l'} / \left(N^{j,\mathrm{B}}_{l} \right) \\ &\quad \times \left(\delta_{\alpha\,\alpha'} \delta_{l\,l'} \delta_{m\,m'} + \frac{1}{k^2_{\mathrm{B}}} \sum_{\gamma_{\alpha,\alpha'}} g_{\gamma_{\alpha,\alpha'}} \delta_{l-\gamma'_{\alpha,\alpha'}\,l'} \delta_{m-\gamma''_{\alpha,\alpha'}\,m'} \right), \end{aligned}} \tag{3.39}$$

where $I^{\mathbb{R}^3 - V_j}_{l'}$ is the radial part of the integral outside the scatterer; It is defined and expressed in Appendix B.3. The B-integrals for all permutations of the polarizations, α and α', are expressed in Appendix B.5.

3.4 Field Outside Scatterers

With the results from the first parts of this chapter, we have expressed the field inside the scatterers. We may then compute the field outside these source regions by explicit evaluation of the Lippmann-Schwinger equation, Eq. (3.1), as follows

$$\boxed{\begin{aligned} \mathbf{E}^{\alpha}(\mathbf{r}) &= \mathbf{E}^{\alpha}_{\mathrm{B}}(\mathbf{r}) + k^2_0 \sum_{j=1}^{N} \Delta\epsilon_j \sum_{\alpha'} H^{\alpha\alpha'}_{j}(\mathbf{r}), && \text{(3.40a)} \\ H^{\alpha\alpha'}_{j}(\mathbf{r}) &\equiv \int_{V_j} \mathbf{G}^{\alpha\alpha'}_{\mathrm{B}}(\mathbf{r},\mathbf{r}'_j) \mathbf{E}^{\alpha'}(\mathbf{r}'_j)\, \mathrm{d}\mathbf{r}'_j. && \text{(3.40b)} \end{aligned}}$$

In these equations, $k^2_0 \Delta\epsilon_j H^{\alpha\alpha'}_{j}(\mathbf{r})$ is the scattered field at position $\mathbf{r}$ along the Cartesian direction α due to the induced field at scatterer j along the Cartesian direction α'.

Interchanging the roles of $\mathbf{r}_j$ and $\mathbf{r}'_j$ and proceeding as for the B-integrals of the previous section, the integrals $H_j^{\alpha\alpha'}(\mathbf{r})$ may be evaluated analytically for all permutations of the polarizations. We give the detailed expressions in Appendix C.2.

3.5 Background Field

In the following sections, we express the expansion coefficients for the background field, cf. Eq. (3.13b), for three different types of sources. We explore all of these in the two following chapters.

3.5.1 Plane Wave

We consider an arbitrary incoming plane wave, of the form

$$\mathbf{E}_{\mathrm{B}}(\mathbf{r}) = E_0 \exp(i\mathbf{k}_{\mathrm{B}} \cdot \mathbf{r})\, \mathbf{e}_{\mathrm{B}} \tag{3.41}$$

where E_0 and $\mathbf{k}_{\mathrm{B}}$ are the amplitude and the wave vector of the incoming plane wave, respectively, while $\mathbf{e}_{\mathrm{B}}$ is its unit polarization. θ_k and ϕ_k are the global polar and azimuthal angles of $\mathbf{k}_{\mathrm{B}}$, and to ensure transversality of the plane wave we may express the coordinates of $\mathbf{e}_{\mathrm{B}}$ as follows

$$\mathbf{e}_{\mathrm{B}} = \begin{bmatrix} -\cos(\theta_k)\cos(\phi_k) \\ -\cos(\theta_k)\sin(\phi_k) \\ \sin(\theta_k) \end{bmatrix} \equiv \begin{bmatrix} \mathbf{e}_{\mathrm{B}}^x(\theta_k,\phi_k) \\ \mathbf{e}_{\mathrm{B}}^y(\theta_k,\phi_k) \\ \mathbf{e}_{\mathrm{B}}^z(\theta_k,\phi_k) \end{bmatrix}. \tag{3.42}$$

We then express the expansion coefficients of the incoming plane wave on the background basis functions [34, Chap. 3]

$$e^{\mathrm{B}}_{j\alpha lm} = \left[E_0 \mathbf{e}^{\alpha}_{\mathrm{B}}(\theta_k,\phi_k) 4\pi i^l \{Y_l^m(\theta_k,\phi_k)\}^{Y^*} / \left(N_l^{j,\mathrm{B}}\right) \right] \exp(i\mathbf{k}\cdot\mathbf{r}_j^0), \tag{3.43}$$

where the exponential factor accounts for the definition of the basis functions in local coordinates.

3.5.2 Dipole Emitter: Background Green's Tensor

The electric field produced by a dipole emitter, with dipole moment along the direction α, in a homogeneous space is the αth column of the background Green's tensor, $\mathbf{G}_{\mathrm{B}}(\mathbf{r},\mathbf{r}_{\mathrm{d}})$, with $\mathbf{r}_{\mathrm{d}}$ at the position of the emitter [24, Chap. 2]. In analogy, the field produced by the same dipole emitter in the homogeneous space including the spherical scatterers is the αth column of the Green's tensor, $\mathbf{G}(\mathbf{r},\mathbf{r}_{\mathrm{d}})$, which satisfies Dyson's equation [28]

$$\mathbf{G}(\mathbf{r},\mathbf{r}_{\mathrm{d}}) = \mathbf{G}_{\mathrm{B}}(\mathbf{r},\mathbf{r}_{\mathrm{d}}) + \int_V \mathbf{G}_{\mathrm{B}}(\mathbf{r},\mathbf{r}'') k_0^2 \Delta\epsilon(\mathbf{r}'') \mathbf{G}(\mathbf{r}'',\mathbf{r}_{\mathrm{d}})\, \mathrm{d}\mathbf{r}'', \tag{3.44}$$

where for brevity we omit the Principal value and the source dyadic, cf. Eq. (2.17). This relation is completely analogous to the Dyson's equation satisfied by Green's functions in many-body quantum theory, where the interaction potential, which here is represented by $\Delta\epsilon(\mathbf{r}'')$, for instance may be the Coulomb interaction between electrons [35]. More importantly, Eq. (3.44) is the Lippmann-Schwinger equation, if we treat $\mathbf{G}_{\mathrm{B}}(\mathbf{r},\mathbf{r}_{\mathrm{d}})$ and $\mathbf{G}(\mathbf{r},\mathbf{r}_{\mathrm{d}})$ columnwise, so we may use the machinery developed in this chapter to determine the Green's tensor.

To that end, we need an expansion of the background Green's tensor on the background basis functions. This is done by applying a slightly modified version of Eq. (3.36) for expressing the scalar Green's function, $g_{\mathrm{B}}(\mathbf{r}, \mathbf{r}_{\mathrm{d}})$

$$g_{\mathrm{B}}(\mathbf{r}, \mathbf{r}_{\mathrm{d}}) = ik_{\mathrm{B}} \sum_{\nu,\mu} (-1)^{\mu} \tilde{\psi}^{j,\mathrm{B}}_{\nu,\mu}(\mathbf{r}_j) \varphi^{\mathrm{B}}_{\nu,-\mu}(\mathbf{r}_{\mathrm{d}}). \tag{3.45}$$

We then, at our convenience, express the elements of the background Green's tensor by acting the differential operators on $\varphi^{\mathrm{B}}_{\nu,-\mu}(\mathbf{r}_{\mathrm{d}})$ and replace $\tilde{\psi}^{j,\mathrm{B}}_{\nu,\mu}(\mathbf{r}_j)$, cf. its definition (Eq. (3.8b))

$$\begin{aligned}\mathbf{G}^{\alpha\alpha'}_{\mathrm{B}}(\mathbf{r}, \mathbf{r}_{\mathrm{d}}) = ik_{\mathrm{B}} \sum_{\nu,\mu} (-1)^{\mu} \psi^{j,\mathrm{B}}_{\nu,\mu}(\mathbf{r}_j) / \left(N^{j,\mathrm{B}}_{\nu}\right) \\ \times \left(\delta_{\alpha\,\alpha'} \varphi^{\mathrm{B}}_{\nu,-\mu}(\mathbf{r}_{\mathrm{d}}) + \frac{1}{k^2_{\mathrm{B}}} \sum_{\gamma_{\alpha,\alpha'}} g_{\gamma_{\alpha,\alpha'}} \varphi^{\mathrm{B}}_{\nu(\gamma_{\alpha,\alpha'}),\mu^*(\gamma_{\alpha,\alpha'})}(\mathbf{r}_{\mathrm{d}}) \right),\end{aligned} \tag{3.46}$$

where $\mu^*(\gamma_{\alpha,\alpha'}) \equiv -\mu + \gamma''_{\alpha,\alpha'}$. The above relation is what we wanted: An expansion of the elements of the background Green's tensor on $\psi^{j,\mathrm{B}}_{\nu,\mu}(\mathbf{r}_j)$. The expansion coefficients are thus

$$e^{\mathrm{B}}_{j\alpha lm} = ik_{\mathrm{B}}(-1)^m / \left(N^{j,\mathrm{B}}_{l}\right) \left(\delta_{\alpha\,\alpha'} \varphi^{\mathrm{B}}_{l,-m}(\mathbf{r}_{\mathrm{d}}) + \frac{1}{k^2_{\mathrm{B}}} \sum_{\gamma_{\alpha,\alpha'}} g_{\gamma_{\alpha,\alpha'}} \varphi^{\mathrm{B}}_{l(\gamma_{\alpha,\alpha'}),m^*(\gamma_{\alpha,\alpha'})}(\mathbf{r}_{\mathrm{d}}) \right). \tag{3.47}$$

The explicit expressions for the g-coefficients are, as mentioned earlier, given in Appendix A.5.

Using this, we in Section 5.4 present example calculations of the Green's tensor in the gap between two metallic scatterers.

3.5.3 Quasinormal Modes: No Background Field

In the context of optical microcavities, trapping of light at increasingly smaller volumes has has received significant attention in recent years, and important concepts such as cavity modes, the Purcell effect and high-Q cavities have been investigated and analyzed from many different angles [21]. The cavity modes can be rigorously described as quasinormal modes, $\mathbf{f}_i(\mathbf{r}; \tilde{\omega}_i)$, that are modes with complex eigenfrequencies, $\tilde{\omega}_i$, satisfying an "excitation-free" Lippmann-Schwinger equation [36]

$$\mathbf{f}_i(\mathbf{r}; \tilde{\omega}_i) = k_0^2(\tilde{\omega}_i) \int_V \mathbf{G}_{\mathrm{B}}(\mathbf{r}, \mathbf{r}'; \tilde{\omega}_i) \Delta\epsilon(\mathbf{r}'; \tilde{\omega}_i) \mathbf{f}_i(\mathbf{r}'; \tilde{\omega}_i)\, \mathrm{d}\mathbf{r}'. \tag{3.48}$$

In the above, we have absorbed the technical detail of the source dyadic, introduced in Eq. (2.16), in the integral for brevity.

Using the expansion technique developed in this chapter, these quasinormal modes satisfy the following equations

$$\mathbf{G}_{\mathrm{QN}}(\tilde{\omega}_i) \mathbf{f}_i(\tilde{\omega}_i) = \frac{1}{k_0^2(\tilde{\omega}_i)} \mathbf{f}_i(\tilde{\omega}_i), \tag{3.49a}$$

$$\mathbf{G}_{\mathrm{QN}}(\tilde{\omega}_i) \equiv \mathbf{G}(\tilde{\omega}_i) \boldsymbol{\Delta\epsilon}(\tilde{\omega}_i) - \frac{1}{k_0^2(\tilde{\omega}_i)} \frac{L}{\epsilon_{\mathrm{B}}} \boldsymbol{\Delta\epsilon}(\tilde{\omega}_i), \tag{3.49b}$$

where $\mathbf{f}_i(\tilde{\omega}_i)$ holds the expansion coefficients of the ith quasinormal mode, $\mathbf{f}_i(\mathbf{r};\tilde{\omega}_i)$. This equation is a generalized eigenvalue equation, with $1/k_0^2(\tilde{\omega}_i)$ being the eigenvalue, and the quasinormal modes are the corresponding self-consistent solutions that we later determine iteratively. The associated Q-factor may be expressed as follows [24, 36]

$$Q_i = -\frac{\mathrm{Re}(\tilde{\omega}_i)}{2\mathrm{Im}(\tilde{\omega}_i)}. \tag{3.50}$$

3.6 Cross Sections – Revisited

In Section 2.4, we introduced the extinction, scattering and absorption cross sections, and we in particular developed expressions for their evaluation when the electric field is determined, see Eqs. (2.31), (2.32) and (2.34). In this section, we express these explicitly using the results from the previous parts of this chapter.

With the orthonormality of the basis functions, Eq. (3.11a), and the expansion of the field, Eq. (3.13a), the absorption cross section becomes

$$C_{\mathrm{abs}} = \frac{k_{\mathrm{B}}}{\epsilon_{\mathrm{B}}} \frac{\sum_{j=1}^{N} \mathrm{Im}(\epsilon_j) \sum_{\alpha} \sum_{l,m} |e_{j\alpha lm}|^2}{|E_0|^2}. \tag{3.51}$$

The determination of the expansion coefficients is always the starting point, and the associated value of C_{abs} is subsequently easily evaluated by the above result.

To determine the extinction and absorption cross sections, we need to express the scattering amplitude, $\mathbf{f}(\theta,\phi)$, cf. Eq. (2.23). The scattered field is represented by the second term in Eq. (3.40a), and to express the scattering amplitude explicitly we have to extract the $\exp(ik_{\mathrm{B}}r)/r$ dependence from this. To that end, we return to the expressions for $H_j^{\alpha\alpha'}(\mathbf{r})$ that are given explicitly in Appendix C.2; These contain sums over terms that are all proportional to one of the spherical outgoing wavefunctions, $\varphi_{l,m}^{\mathrm{B}}(\mathbf{r}_j)$. These, in turn, contain the spherical Hankel functions, $h_l^{(1)}(k_{\mathrm{B}}r_j)$, and expanding these asymptotically as $k_{\mathrm{B}}r_j \to \infty$ we find [37]

$$h_l^{(1)}(k_{\mathrm{B}}r_j) \simeq \frac{(-i)^{l+1}\exp(-i\mathbf{k}_{\mathrm{B}}\cdot\mathbf{r}_j^0)}{k_{\mathrm{B}}} \frac{\exp(ik_{\mathrm{B}}r)}{r}, \qquad 1 \ll k_{\mathrm{B}}r. \tag{3.52}$$

So in $H_j^{\alpha\alpha'}(\mathbf{r})$ we replace the spherical Hankel functions by $(-i)^{l+1}\exp(-i\mathbf{k}_{\mathrm{B}}\cdot\mathbf{r}_j^0)/k_{\mathrm{B}}$, and thus have the scattering amplitude

$$\mathbf{f}^{\alpha}(\theta,\phi) = k_0^2 \sum_{j=1}^{N} \Delta\epsilon_j \exp(-i\mathbf{k}_{\mathrm{B}}\cdot\mathbf{r}_j^0) \sum_{\alpha'} H_j^{\alpha\alpha'}(\mathbf{r}) \left(\varphi_{l,m}^{\mathrm{B}}(\mathbf{r}_j) \to \Phi_{l,m}^{j}(\mathbf{r}_j)\right), \tag{3.53}$$

where $\Phi_{l,m}^{j}(\mathbf{r}_j)$ is defined in Appendix C.3.

With the scattering amplitude at hand, the extinction and scattering cross sections may be computed, cf. Eqs. (2.31)-(2.32). However, the contributions in $\mathbf{f}(\theta,\phi)$ from each scatterer are, as we see above, defined in the local coordinates and to perform the solid angle integrations in the expression for C_{scat}, a slight, but tedious modification is needed. We present the details of this in Appendix C.3.

In the following chapter, we in a few cases compute C_{ext}, C_{scat} and C_{abs} independently to verify that $C_{\mathrm{ext}} = C_{\mathrm{scat}} + C_{\mathrm{abs}}$. Subsequently, we merely compute C_{ext} from Eqs. (2.32) and (3.53) and C_{abs} from Eq. (3.51), and then determine $C_{\mathrm{scat}} = C_{\mathrm{ext}} - C_{\mathrm{abs}}$ from these.

3.7 Small Scatterer Limit: Dipole Approximation

When the scatterers are sufficiently small, they may be interpreted as small polarizable dipoles, with dipole moments proportional to the constant local fields. In that case, the Lippmann-Schwinger equation may be expressed as an algebraic equation, which greatly simplifies the determination of the field. Below we present the outline for proceeding in this way, but we already note that the approach has certain limitations: The size of the scatterers must be much smaller than the wavelength, and the scatterers must not be too close to each other [38, Chap. 8]. In the next chapter, we analyze its validity by comparison with the full solution from the formalism developed earlier in this chapter.

We set the field inside scatterer j equal to the value at its center:

$$\mathbf{E}(\mathbf{r}_j) \simeq \mathbf{E}(\mathbf{r}_j^0), \tag{3.54}$$

and express Lippmann-Schwinger equation for a collection of N scatterers, Eq. (3.1), using this

$$\mathbf{E}^{\mathrm{D}}(\mathbf{r}_j^0) = \mathbf{E}_{\mathrm{B}}(\mathbf{r}_j^0) + k_0^2 \sum_{j'=1}^{N} \mathbf{G}^{\mathrm{D}}_{jj'} \Delta\epsilon_{j'} \mathbf{E}^{\mathrm{D}}(\mathbf{r}_{j'}^0) - \frac{\Delta\epsilon_j}{\epsilon_{\mathrm{B}}} \mathbf{L}\mathbf{E}^{\mathrm{D}}(\mathbf{r}_j^0), \tag{3.55a}$$

$$\mathbf{G}^{\mathrm{D}}_{jj'} \equiv \int_{V_{j'}-\delta V_{j'}} \mathbf{G}_{\mathrm{B}}(\mathbf{r}_j^0, \mathbf{r}')\, \mathrm{d}\mathbf{r}'. \tag{3.55b}$$

Superscripts D have been applied to stress that we are working in the dipole approximation. The integrals defining the tensor $\mathbf{G}_{jj'}$ are expressed analytically in Appendix C.4, and the above equations are essentially those used in a similar procedure in [38, Chap. 8]. Eqs. (3.55) constitute $3N$ algebraic equations for the field components at the N small scatterers, and we solve them as follows

$$\mathbf{e}^{\mathrm{D}} = \left(\mathbf{I} + \frac{L}{\epsilon_{\mathrm{B}}} \boldsymbol{\Delta\epsilon} - k_0^2 \mathbf{G}^{\mathrm{D}} \boldsymbol{\Delta\epsilon} \right)^{-1} \mathbf{e}^{\mathrm{D}}_{\mathrm{B}}, \tag{3.56}$$

where $\mathbf{e}^{\mathrm{D}}$ ($\mathbf{e}^{\mathrm{D}}_{\mathrm{B}}$) holds the $3N$ components of the electric field (background field) at the centers of the N scatterers. The diagonal matrix $\boldsymbol{\Delta\epsilon}$ holds the dielectric contrasts, $\Delta\epsilon_j$, and $\mathbf{G}^{\mathrm{D}}$ is a matrix with $N \times N$ submatrices of the form as $\mathbf{G}^{\mathrm{D}}_{jj'}$, see Eq. (3.55b).

Once we have solved for $\mathbf{e}^{\mathrm{D}}$, we may compare this result with that from the full formalism. This is done by integrating the difference between the true field, $\mathbf{E}(\mathbf{r}'_j)$, and the constant dipole field, $\mathbf{E}^{\mathrm{D}}(\mathbf{r}_j^0)$, over all scatterers and normalizing this to the total integrated field

$$\mathcal{E}^{\mathrm{D}}_{\mathrm{G}} \equiv \sum_{j\alpha} \frac{\int_{V_j} \left| \mathbf{E}(\mathbf{r}'_j) - \mathbf{E}^{\mathrm{D}}(\mathbf{r}_j^0) \right| \, \mathrm{d}\mathbf{r}'_j}{\int_{V_j} \left| \mathbf{E}(\mathbf{r}'_j) \right| \, \mathrm{d}\mathbf{r}'_j}, \tag{3.57}$$

where the summations are over all scatterers and polarizations, respectively. We later assess the quality and validity of the dipole approximation using this integrated relative deviation as a quantitative measure.

3.8 Summary

The main result of the previous chapter, the Lippmann-Schwinger equation, has been solved analytically in the specific case of spherical scatterers in a homogeneous 3D

background. The main results for determining the electric field in this geometry are summarized by the boxed equations in the chapter. The overall ideas in evaluating the important Green's tensor matrix elements were given, which involved a number of technical details. Many of the resulting and bulky expressions are given explicitly in appendices, as stated in the chapter. Additionally, we have expressed the field outside the scatterers and presented three different types of background fields, namely a plane wave, the background Green's tensor giving the field from a dipole emitter and no background field, giving rise to the so-called quasinormal modes. Finally, we have explicitly expressed the cross sections, in the language of the present formalism, and we have derived a set of algebraic equations for solving the Lippmann-Schwinger equation in the limit of small scatterers.

All of the above has been implemented in a MATLAB software package, from which simulations of the electric field and related quantities can be carried out. We in the following chapters explore different configurations and present and analyze related results.

Chapter 4

Error Estimates and Benchmarking

> *Remember that all models are wrong; the practical question is how wrong do they have to be to not be useful.*
>
> George E. P. Box, *Empirical Model-Building and Response Surfaces*

For the formalism developed in the previous chapter and its numerical implementation, this chapter validates the computations by analyzing the convergence and through benchmarking of the cross section calculations. Firstly, the local and global error estimates from the Lippmann-Schwinger equation are analyzed for a geometry of two scatterers. Next, the dipole approximation is investigated, as function of the size of the scatterers and the distance between these, and the cross sections are computed in two specific cases for validation against known results from the literature. Finally, a section addressing computation times and scalability of the present formalism concludes the chapter.

4.1 Convergence of Field and Error Estimates

In this section, we present some preliminary results from the formalism developed in the previous chapter. We use these to assess the convergence for the geometry of two scatterers, a so-called dimer, that we analyze in more detail in the next chapter.

Fig. 4.1 shows a schematic of the dimer: It consists of two Ag scatterers aligned along the y-axis. The scatterers have radius R and the distance between them is d. The structure is illuminated by a plane wave with wave vector $\mathbf{k}_\mathrm{B}$, and the resulting scattered field is indicated by the dashed red arrows. The green line is the plot line along which we present results below.

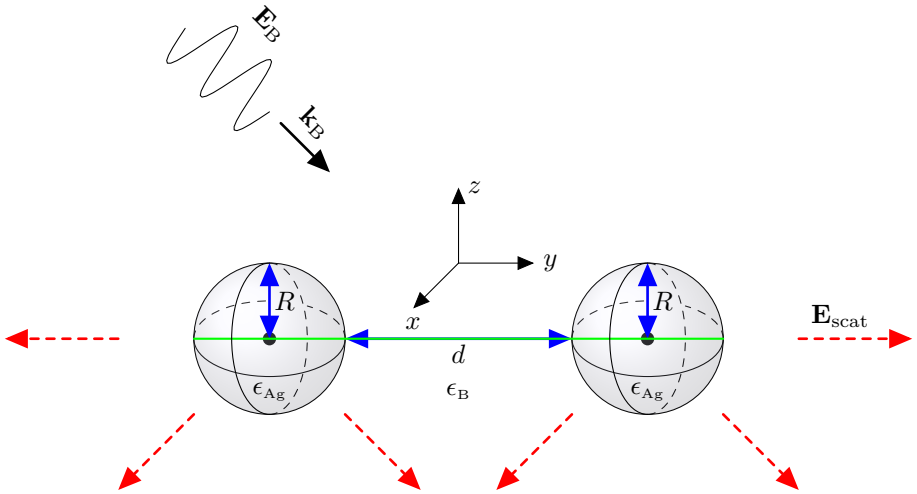

Figure 4.1 Schematic diagram of two Ag scatterers of permittivity ϵ_{Ag}, embedded in a homogeneous background medium of permittivity ϵ_B. The scatterers have radius R and are spaced a distance d from each other. The incoming field, $\mathbf{E}_\mathrm{B}$, with wave vector $\mathbf{k}_\mathrm{B}$ is indicated. The green line is the line along which results are shown in Figs. 4.2-4.3.

In the first place, we consider oblique incidence ($\theta_k = \phi_k = \pi/3$, cf. Eqs. (3.41)-(3.42)), which implies that the incoming field has three non-zero components. We later consider symmetric cases, e.g. with $\mathbf{E}_\mathrm{B}$ polarized along the scatterer axis, y, and see that this may give rise to strong, local field enhancements, but for now we deliberately avoid such symmetries.

We note that this configuration has three characteristic length scales: The wavelength of the incoming radiation (λ_B), the size of the scatterers (R) and the spacing between the scatterers (d), and we in this section analyze the impact of their relative magnitudes. Intuitively, we expect that more basis functions are needed when R is increased with respect to λ_B, to account for the possibly stronger variations of the field inside the larger scatterers, but the impact of the size of d with respect to R also plays a prominent role, as we shall see. We fix $\lambda_\mathrm{B} = \lambda_0/\sqrt{\epsilon_\mathrm{B}} = 800$ nm$/1.5 = 533$ nm and $R = 25$ nm in the following sections.

4.1.1 Field

In Fig. 4.2, we show the absolute values of $\mathbf{E}^x$, $\mathbf{D}^y$ and $\mathbf{E}^z$ along the green line in Fig. 4.1. From the electromagnetic boundary conditions, Eqs. (2.22), we expect these quantities to be continuous everywhere on this line and in particular at the interfaces between the spheres and the background material.

The subfigures show the field components for two different values of the gap distance: $d/R = 4$ in Fig. 4.2(a) and $d/R = 0.4$ in Fig. 4.2(b). The top panel in each figure shows the permittivity profiles along the y-axis: The real part is indicated by the full blue lines, and the imaginary part by dashed red lines. In each subfigure, we show the field profiles resulting from three truncations of the sets of basis functions: $l_{\mathrm{max}} \in \{2, 5, 8\}$, giving rise to 9, 36 and 81, respectively, basis functions per polarization per scatterer, cf. Eq. (3.14).

We first consider the field distributions of Fig. 4.2(a), where the scatterers are spaced

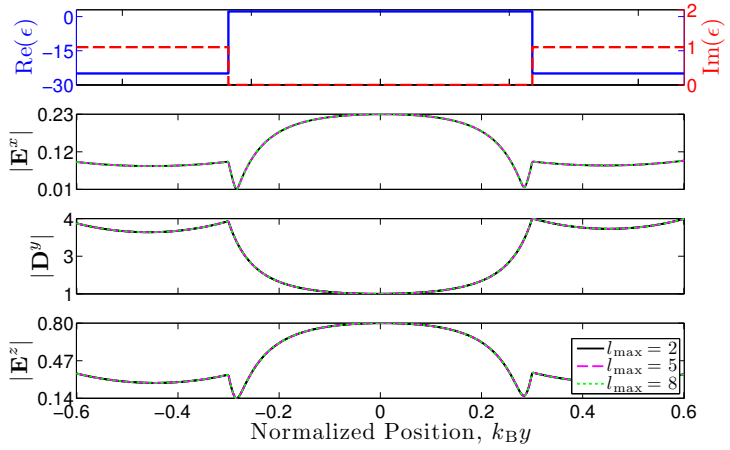

(a) $d/R = 4$.

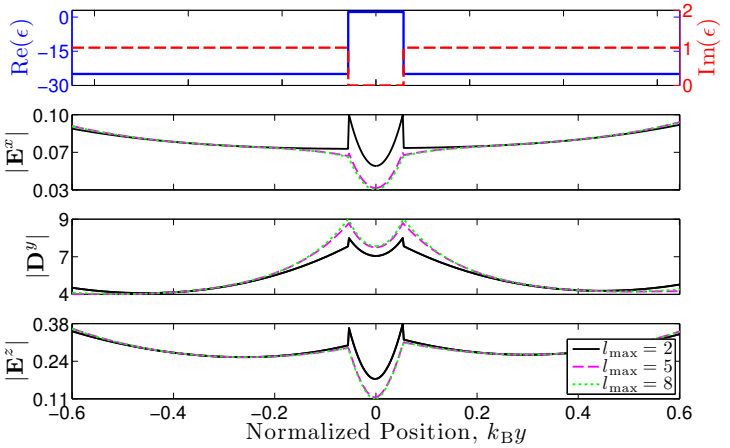

(b) $d/R = 0.4$.

Figure 4.2 Absolute values of components of electric field along y-axis, cf. the green line in Fig. 4.1. The radius of the two Ag scatterers is in all cases $R = 25$ nm nm, while the spacing between the scatterers, d, is varied in the plots. The wavelength of the incident plane wave is $\lambda_B = \lambda_0/\sqrt{\epsilon_B} = 800$ nm$/1.5 = 533$ nm. The top panel in all figures shows the real (full blue) and imaginary (dashed red) part of the permittivity.

the furthest from each other. Looking at the interface points, located where the permittivity profile changes discontinuously in the top panel, we see that the boundary conditions are satisfied: The tangential components of $\mathbf{E}$ and the normal component of $\mathbf{D}$ are continuous. Likewise, we note that at this choice of the scatterer spacing, $d/R = 4$, the field converges rapidly, since the curves for the three different truncations lie on top of each other.

In contrast, when $d/R = 0.4$, Fig. 4.2(b), the picture is different. We first note that the field profiles are altered by the reduction of the spacing, but more importantly we see that the field does not converge as rapidly as in the previous setup; The curves with $l_{\max} = 2$ (full black lines) are discontinuous at the interfaces and deviate substantially

from the $l_{\max} = 5$ (dashed magenta lines) and the $l_{\max} = 8$ (dotted green lines) curves.

So a first conclusion can be drawn: The closer the scatterers are, the more basis functions are needed to obtain convergent results in the computation of the electric field. In Section 3.2.1, we discussed the choice of basis functions, and we noted that when using the pulse basis expansion, a large number of basis functions was required when trying to resolve features of dimensions much smaller than the wavelength. Even though this is less apparent when using the more sophisticated spherical basis functions, the same concept applies: The truncation in the number of basis functions sets a lower limit for the resolvable features. So when d decreases, we need increasingly more basis functions to correctly resolve the field over this length scale.

4.1.2 Local Relative Error

Another way of illustrating the convergence is to consider the local relative error of the Lippmann-Schwinger equation, $\mathcal{E}_{\mathrm{L}}(\mathbf{r})$, see Eq. (2.20b). This quantity measures how well the approximated field satisfies the self-consistent Lippmann-Schwinger equation, Eq. (2.18a), and its investigation is therefore of principal importance when discussing the convergence.

We stress that the local relative error is defined inside the scatterers, since the Lippmann-Schwinger equation is only implicit for the field in these regions. In Fig. 4.3, we show the local relative error, along the parts of the green line in Fig. 4.1 that are inside the scatterers. We, as in the previous figure, plot it for three different truncations, $l_{\max}$, and at two different scatterer spacings, d, still with fixed R and λ_{B}.

The overall trend is the same for all values of $l_{\max}$ and d/R: The local relative error is smallest in the middle of the scatterers and increases as we go towards the boundary of the scatterer. As discussed in Section 3.2, the basis functions inside each scatterer are defined relative to the center of the scatterers, and the field is expanded around these local Origos. This implies that convergence is best at or close to the centers, explaining the overall picture in Fig. 4.3. We also note that generally the local relative error decreases when $l_{\max}$ is increased, and considering first Fig. 4.3(a), with the largest scatterer spacing, we see that we gain approximately two to three orders of magnitude in all points when $l_{\max}$ is increased by three units.

As we then decrease the scatterer spacing by one order of magnitude, Fig. 4.3(b), the picture is the same in the center of the scatterers. But the same is no longer the case, as we approach the boundary of the scatterers where the local relative error only decreases slightly when $l_{\max}$ is increased. That is, the local relative error of the Lippmann-Schwinger equation confirms what we observed indirectly in Fig. 4.2: The convergence of the field, for fixed truncations $l_{\max}$, becomes substantially slower as the scatterer spacing is decreased below the scatterer radius, $d/R < 1$.

In the view of this, we focus on the local relative error at the boundary of the scatterers. In Fig. 4.4, we plot the average of the local relative error at these two points (green dots in inset) for five different values of d/R and at the same three values of $l_{\max}$ as in the previous figures. We note that both axes in the plot are logarithmic. The plot supports the overall conclusions from the field plots and plots of the local relative error, namely that the local relative error at the boundary increases, for fixed $l_{\max}$, as d/R is decreased.

4.1.3 Global Relative Error

Finally, we in Fig. 4.5 show the global relative error of the Lippmann-Schwinger equation, $\mathcal{E}_{\mathrm{G}}$, for the two-scatterer geometry. The overall trend in this plot is as in Fig. 4.4, and

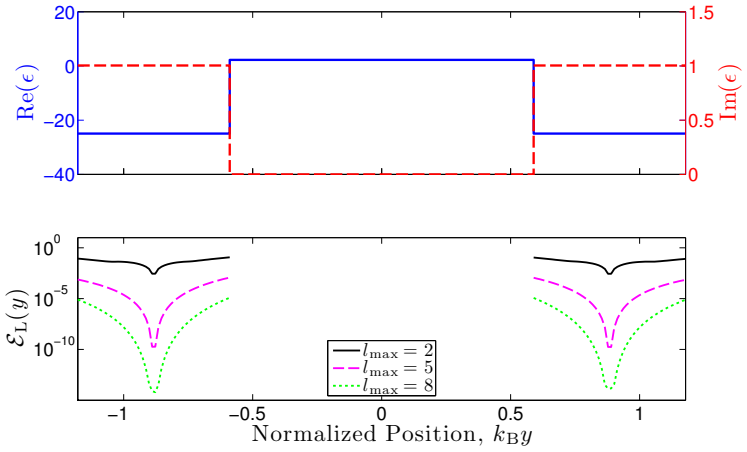

(a) $d/R = 4$.

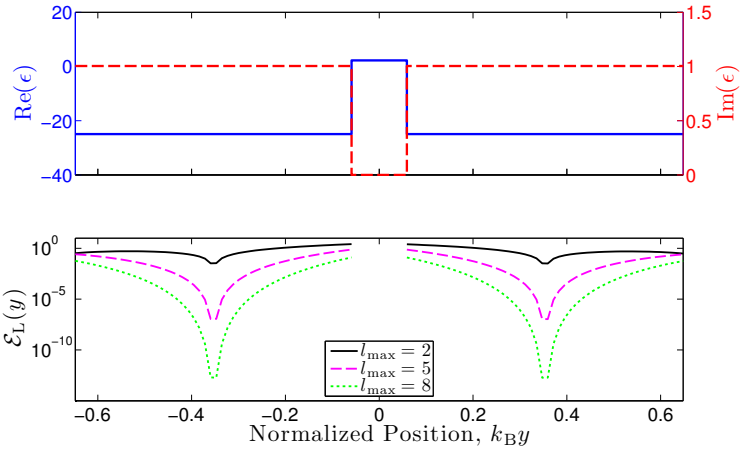

(b) $d/R = 0.4$.

Figure 4.3 Local relative error of Lippmann-Schwinger equation, $\mathcal{E}_L(\mathbf{r})$, along y-axis, cf. the green line in Fig. 4.1. The parameters are as those in Fig. 4.2, and the top panel in all subfigures shows the real (full blue) and imaginary (dashed red) part of the permittivity.

this inspires us to plot the ratio of $\mathcal{E}_G$ and $\mathcal{E}_L(R)$ which is done in the inset in the figure. As discussed in Section 2.2.2, the global relative error is the local relative error averaged over all points inside the scatterers, and since the local relative error on the boundary is generally larger than for points inside the scatterers, as shown in Fig. 4.3, the ratio of the two is smaller than unity. But we note that the ratio is on the order of 0.1–0.5, so the global relative error is approximately one half to one order of magnitude smaller than the local relative error on the boundary. We may therefore readily use the local relative error on the boundary of the scatterers, in the place of the global relative error, to estimate the accuracy of the computed fields.

In conclusion concerning convergence and error estimates: We could, in principle, always compute $\mathcal{E}_G$ and check that it is smaller than some predefined value, but the computation of it is demanding due to the involved 3D numerical quadrature. The

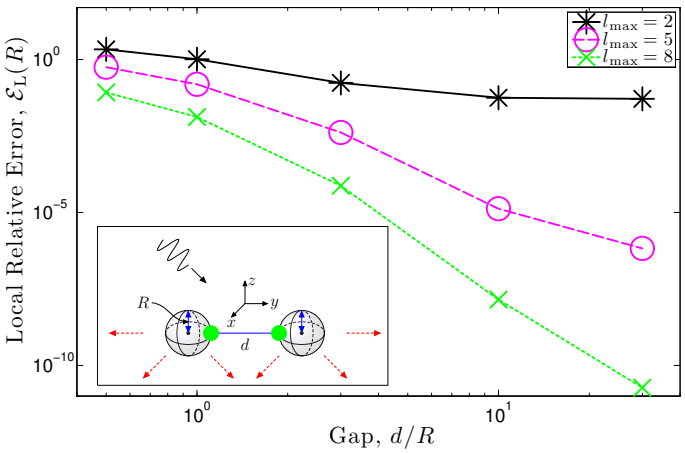

Figure 4.4 Local relative error of Lippmann-Schwinger equation, $\mathcal{E}_L(R)$, at boundaries of scatterers, as indicated by the green dots in the inset. The parameters are as those in Fig. 4.2, and $\mathcal{E}_L(R)$ is plotted as function of scatterer spacing, d/R, for different truncations, l_{max}.

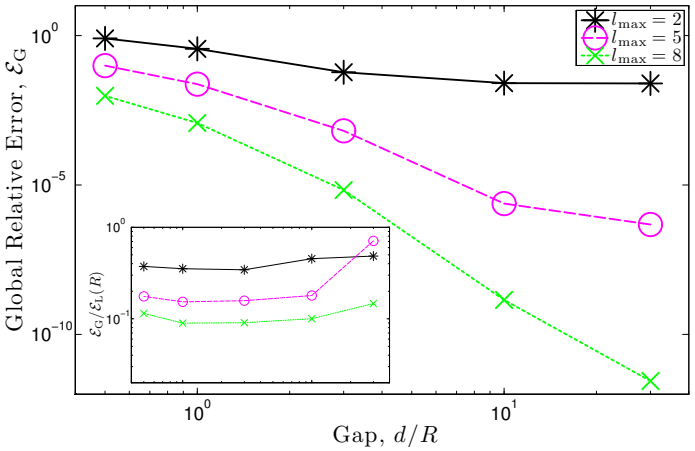

Figure 4.5 Global relative error of Lippmann-Schwinger equation, $\mathcal{E}_G$, for the two-scatterer geometry of Fig. 4.1. The parameters are as those in Fig. 4.2, and $\mathcal{E}_G$ is plotted as function of scatterer spacing, d/R, for different truncations, l_{max}. The inset shows the ratio between the global relative error and the local relative error (Fig. 4.4).

present results show that the local relative error on the boundary of the scatterers is a conservative estimate that can be used in the place of $\mathcal{E}_G$. We also in conclusion of this section note that increasing the distance between the scatterers yields faster convergence, that is, accurate results can be obtained with lower values of l_{max} for increasing values of d. This last conclusion is also observed in a similar type of calculation in [39].

4.2 Dipole Approximation

In this section, we investigate the dipole approximation for solving the Lippmann-Schwinger equation which we developed in Section 3.7.

We return to the configuration from Section 4.1 and use it to assess the validity of the dipole approximation for solving the Lippmann-Schwinger equation. The incoming field and the permittivities are as described in that section, and the radius of the two scatterers, R, and the gap distance between these, d, see inset in Fig. 4.6, will be varied. These specific choices of parameters; Choice of materials, choice of wavelength of the incoming field and choice of direction and polarization of the incoming field, imply that the analyses will not be exhaustive with respect to all parameters, but they will nevertheless provide a guideline for the region of validity of the dipole approximation.

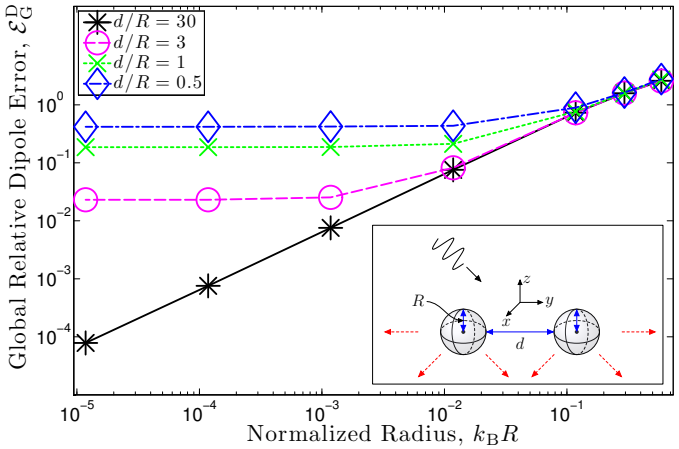

Figure 4.6 Global relative dipole error, $\mathcal{E}_{\mathrm{G}}^{\mathrm{D}}$, as function of the radius of the two scatterers, R. The incoming field and the permittivities are as described in Section 4.1. The different curves correspond to different gaps between the scatterers, d/R.

In Fig. 4.6, we plot the global relative error from the dipole approximation, $\mathcal{E}_{\mathrm{G}}^{\mathrm{D}}$, as function of the normalized radius of the scatterers, $k_{\mathrm{B}}R$. The parametric dependence on the gap distance, d/R, is represented by the four different curves in the figure. The integrated error, $\mathcal{E}_{\mathrm{G}}^{\mathrm{D}}$, is computed as defined in Eq. (3.57), and the integral therein is computed numerically by increasing $l_{\max}$ until a relative error of 10^{-6} is obtained. From Section 4.1, we know that we need increasing $l_{\max}$ when d decreases to obtain this convergence, even if $k_{\mathrm{B}}R < 1$. For instance, with $k_{\mathrm{B}}R = 0.12$ we need $l_{\max} = 5, 9, 10$ and 15 for $d/R = 30, 3, 1$ and 0.5, respectively.

Considering first the full black curve, corresponding to $d/R = 30$, we see that as the size of the scatterers decreases, the accuracy of the dipole approximation for solving the Lippmann-Schwinger equation increases: We gain approximately one order of magnitude in accuracy when we decrease $k_{\mathrm{B}}R$ by one order of magnitude. We then on the dashed magenta curve reduce the gap distance by a factor of 10, $d/R = 3$, and the picture for the four largest values of $k_{\mathrm{B}}R$ is roughly the same as for $d/R = 30$. However, as $k_{\mathrm{B}}R$ is decreased below 10^{-2}, the relative error starts to saturate and eventually converges to approximately 2%. That is, when the two scatterers are spaced three radii from each other, the relative error of the dipole approximation never becomes smaller than 2%, even when $k_{\mathrm{B}}R \ll 1$. As we further decrease the gap distance, $d/R = 1$ (dotted green curve)

and $d/R = 0.5$ (dashed-dotted blue curve), the picture is the same: The global relative dipole error saturates, at 19% and 42%, respectively. The dipole approximation has thus broken down for all values of $k_{\mathrm{B}}R$ with these two gap distances. Additionally, we note that the dipole error, with $d/R = 30$ and $d/R = 3$, only goes below 10% at $k_{\mathrm{B}}R = 0.01$, corresponding to $R = 1$ nm.

In conclusion, we have observed that the dipole approximation, in the specific case that we considered, broke down at all scatterer radii, R, when the gap distance between the scatterers, d, was one radius or less. At larger gap distances, $d/R \geq 3$, we saw that that relative error was below 10% first when $k_{\mathrm{B}}R = 0.01$, implying that the approximation is only valid for scatterers with radii of $R = 1$ nm or less. If one needs a field with a relative error less than 10%, even smaller radii must be applied in the dipole approximation. The authors of Ref. [15] perform dispersion calculations for chains of metallic spheres, and they reach the conclusion that the dipole contribution in these calculations is *"...reasonably accurate..."* when $d/R \geq 1$. They do not give an exact number for this accuracy, but their conclusion supports our findings in this section: When $d/R \lesssim 1$ the dipole approximation is invalid. As stated in the beginning of this section, the analyses presented here are not exhaustive with respect to all the parameters, but in spite of this they give an idea of the scatterer sizes, R, and spacings, d, that can be accurately modeled by the dipole approximation.

4.3 Benchmarking of Cross Sections

In the following sections, we benchmark the calculations of the cross sections in two different geometries. The purpose of these calculations is twofold: To validate the results obtained with the formalism developed in the previous chapter, and to introduce the spectral features of metal particles, that we analyze in detail in the next chapter.

4.3.1 Mie Scattering

As discussed earlier, the scattering of a plane wave on a single spherical scatterer was analyzed and solved by Mie [12], and these results constitute a first and simple platform for benchmarking the multiple-scattering formalism developed in this thesis. Standard references, e.g. [25, Chap. 10] or [26, Chap. 13], cover this theory, and we do not go into the details here. We simply note that the extinction, scattering and absorption cross sections can be expressed analytically, and we may therefore readily compare the cross sections of the formalism of this work to these in the special case $N = 1$. The Mie scattering results used in the following are obtained using a MATLAB software package developed by Christian Mätzler [40].

In Fig. 4.7, we plot the spectra of Q_{ext}, Q_{scat} and Q_{abs} in the wavelength range 200 nm $\leq \lambda_0 \leq$ 800 nm. The colored graphs are the results from Mie scattering theory, and the black dashed graphs are the corresponding efficiencies obtained using the formalism from Chapter 3. We use the Drude parameters from Eqs. (2.37a) and $\epsilon_{\mathrm{B}} = 2.25$, and show the spectra for a sphere of radius $R = 10$ nm and $R = 25$ nm in Figs. 4.7(a) and 4.7(b), respectively. The insets in the figures schematically show the situation. The calculations are performed in both cases with $l_{\max} = 5$.

Concerning the benchmarking, the results from the multiple-scattering formalism are in perfect agreement with the Mie results: The black curves lie on top of the colored curves for both extinction, scattering and absorption efficiencies at both radii.

From a physical point of view, the spectra also contain important information, and we later refer to these results when we perform calculations with $N > 1$ scatterers. The

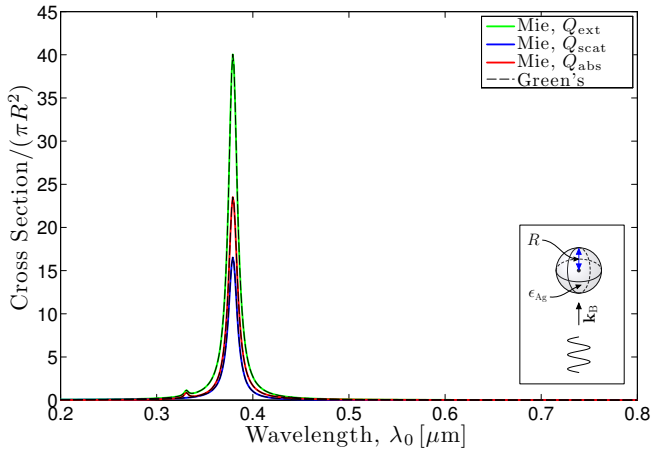

(a) $R = 10$ nm.

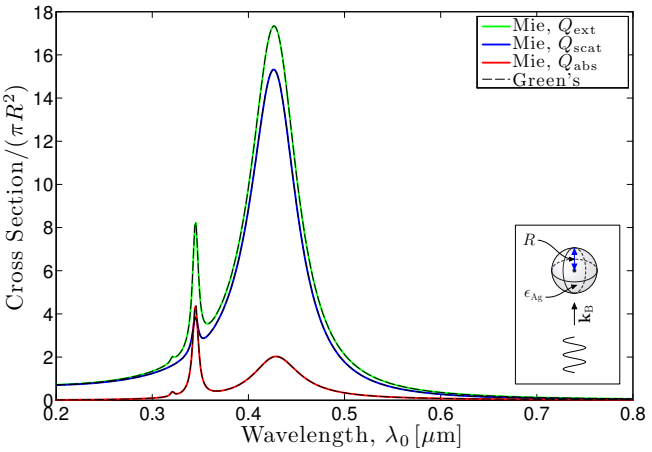

(b) $R = 25$ nm.

Figure 4.7 Spectra of the extinction, scattering and absorption efficiencies, Q_{ext}, Q_{scat} and Q_{abs}, for the scattering of a plane wave on a single spherical Ag scatterer with dielectric function ϵ_{Ag}. The colored curves are obtained using Mie scattering theory, and the black dashed curves are obtained using formalism developed in this work. The results for spheres of two radii, R, are shown.

resonances in the plots correspond to the excitation of localized surface plasmons on the particle. We later show field distributions in the vicinity of the scatterers at these resonances to visualize the field confinement at the surface of the scatterers.

The spectrum in Fig. 4.7(a) with $R = 10$ nm has one pronounced resonance around $\lambda_0 = 370$ nm. To lowest order in the size of the scatterer, R, the resonance appears when the polarizability of the particle has a maximum which happens when $\text{Re}(\epsilon_{\text{Ag}}(\omega)) = -2\epsilon_{\text{B}}$. Solving this equation for ω (or λ_0) yields $\lambda_0^{\text{D}} = 368$ nm, where the superscript D denotes the dipole resonance. So the resonance for the $R = 10$ nm scatterer occurs exactly where we expect. We also note that absorption dominates over scattering at this resonance,

$Q_{\text{scat}} < Q_{\text{abs}}$, which follows from the fact that $Q_{\text{abs}} \propto R$ and $Q_{\text{scat}} \propto R^4$ for small scatterers. Finally, we observe the first sign of the quadrupole resonance, at approximately $\lambda_0^{\text{H}} = 330$ nm, where superscript H indicates a higher-order resonance.

Proceeding to the $R = 25$ nm spectrum, we note that the dominant dipole resonance has redshifted due to the increased size of the scatterer, occurring now at approximately $\lambda_0^{\text{D}} = 425$ nm. This redshift in resonance wavelength is characteristic when increasing the size of the scatterer and can, in a simple picture, be explained by the longer distance between the charges on opposite sites of the particle; This decreases the restoring force inside the particle which effectively reduces the resonance frequency, that is, redshifts the resonance. Additionally, the dipole resonance has spectrally broadened which originates from an increase in radiative damping: The collective oscillations of the electrons in the metal particle emit more photons when the particle size increases, broadening the resonance. [14, Chap. 5]. Finally, we observe that the quadrupole resonance has increased in magnitude, and that scattering now clearly dominates over absorption at the dipole resonance.

In the next chapter, we proceed to calculations and analyses of cross section spectra for multiple-scatterer geometries. This inherently introduces another important length scale, namely the distance between the scatterers, and we analyze the effect of varying this parameter. Likewise, the polarization of the incoming field, that the single spherical scatterer is independent of, is analyzed.

4.3.2 García de Abajo Configuration

In the previous section, we benchmarked the cross section calculations in a single-scatterer geometry, but the real test of the multiple-scattering formalism requires calculations with more than one scatterer. We therefore in the following consider the geometry from the second topmost plot in [17, Fig. 6(a)]: It consists of $N = 2$ Al scatterers, each of radius $R = 19$ nm, and spaced $d = 2$ nm from each other, that are illuminated by a right circularly polarized (RCP) plane wave ($\mathbf{e}_{\text{B}} = 1/\sqrt{2}(\hat{x} - i\hat{y})$) as shown in the inset in Fig. 4.8. They are embedded in vacuum, $\epsilon_{\text{B}} = 1$, and the Al spheres are modeled by the Drude parameters in Eqs. (2.37b). In compliance with the reference, the spectrum in the figure is presented as function of the photon energy, $E = \hbar\omega$. In all other places in this work, the spectra are computed as function of the wavelength, λ_0, and resulting from linearly polarized incoming fields.

Comparing firstly with the plot in the reference, we see that both the extinction and scattering cross section curves have the same shapes as therein. Comparing secondly, to the extent that it is possible, e.g., the peak values of the two curves in the present plot and in the reference, good agreement is found.

In the figure, the scattering cross section has been determined in two independent ways: A direct calculation (dashed blue), based on Eq. (2.31) and the expression for the scattering amplitude, $\mathbf{f}(\theta, \phi)$, from Appendix C.3, and an indirect calculation as $C_{\text{scat}} = C_{\text{ext}} - C_{\text{abs}}$ (full red curve). As the plot reveals, these two routes for obtaining the scattering cross section yield the same results (the integrated relative difference is approximately 10^{-4}). The direct calculation of this quantity is computationally demanding (see Appendix C.3 for details), so we base all following analyses and plots on the indirect calculation of C_{scat}.

With the results from this and the previous section, we have validated the calculations of the cross sections with the present formalism against results from the literature. With this at hand, we in the next chapter, as mentioned earlier, delve into detailed analyses of these quantities.

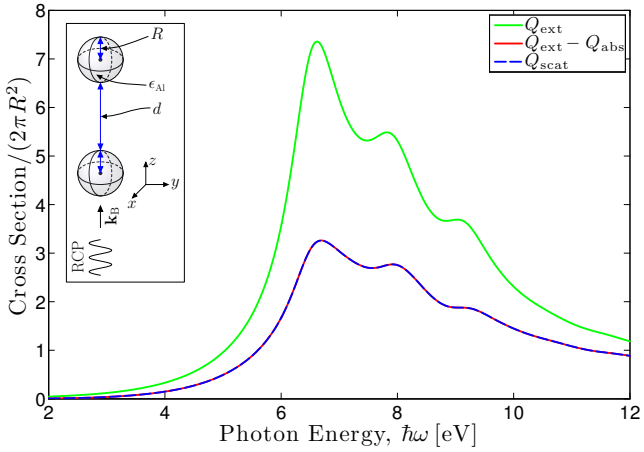

Figure 4.8 Extinction and scattering cross sections, $Q_{\rm ext}$ and $Q_{\rm scat}$, as function of photon energy, $E = \hbar\omega$, for the two-scatterer geometry shown in the inset. The background medium is vacuum, $\epsilon_{\rm B} = 1$, and the radii and scatterer spacing are $R = 19$ nm and $d = 2$ nm, respectively. The scattering cross section has been obtained by two routes: By direct calculation (blue dashed) and indirectly as $C_{\rm scat} = C_{\rm ext} - C_{\rm abs}$ (full red).

4.4 Scalability of Formalism

In this concluding section, we review the computation time and scalability of the formalism developed in the previous chapter. We in particular estimate the computation time and propose several means for decreasing it.

The starting point for a scattering analysis is the construction of the matrices and vectors in the equation giving the expansion coefficients, $\mathbf{e}$, see Eq. (3.16). As discussed in Chapter 3, these quantities have all been expressed analytically, and this, in principle, prompts for rapid evaluation of the expansion coefficients. In practice, all matrices and vectors except the Green's tensor matrix, $\mathbf{G}$, can be computed almost instantaneously, so the evaluation of $\mathbf{G}$ at present represents the bottleneck in the computations. $\mathbf{G}$ contains a total of $3N(l_{\rm max}+1)^2 \times 3N(l_{\rm max}+1)^2 = 9N^2(l_{\rm max}+1)^4$ elements, and using this the solution time for obtaining the expansion coefficients, at a single frequency, is

$$\text{Computation time}(N, l_{\rm max}) \simeq AN^2(l_{\rm max}+1)^4 \tag{4.1}$$

where $A \sim 0.002$ s (Intel Core 2 Duo at 3.00 GHz). This relation has been verified for $1 \leq N \leq 10$ and $0 \leq l_{\rm max} \leq 9$ and except for the limiting cases $N = 1$ and $l_{\rm max} = 0$, it is accurate to within a factor of two. As examples, it takes 3.3 seconds to solve with $l_{\rm max} = 3$ and $N = 3$, 47 seconds to solve with $l_{\rm max} = 8$ and $N = 2$, and 1150 seconds to solve with $l_{\rm max} = 9$ and $N = 6$. So the quartic dependence of the computation time on $l_{\rm max}+1$ is particularly severe, and we in the following review what causes the long computation time, and propose how this can be improved.

In the present implementation, several things have been integrated to decrease the computation time. For identical scatterers, of the same permittivity and radius, the diagonal submatrices in $\mathbf{G}$, $\mathbf{G}_{jj}$, are the same and are consequently reused for all scatterers. Likewise for identical scatterers, the submatrices $\mathbf{G}_{jj'} = (-1)^{\nu}\mathbf{G}_{j'j}$, where ν is a composite variable holding all the indices that the individual matrix elements depend on. In effect, this implies that we only have to compute half of the scattering submatrices, $\mathbf{G}_{jj'}$. Upon

analyzing periodic arrangements of identical scatterers, e.g. a chain of scatterers, even more of the involved scattering submatrices would be identical, and this could further decrease the computation time. This has not been implemented, but in particular if one wants to perform simulations with $N \gg 10$ scatterers, arranged periodically, this improvement would be feasible.

At a more fundamental level, we may address the computation times of the individual elements in $\mathbf{G}$, and we proceed to this in the following.

The detailed expressions for the elements of $\mathbf{G}$ are, as stated earlier, given in Appendix B. At first sight these look cumbersome to evaluate, depending each on a total of eight indices, but all involved quantities can be computed almost instantaneously with the exception of the separation matrices, $S_{l,l'}^{m,m'}(\mathbf{b})$; The evaluation of these constitute more than 90% of the total computation time. The separation matrices enter in the two-center expansion of the scalar Green's function, $g_{\mathrm{B}}(\mathbf{R})$ (see Eq. (3.23)) and allow for simultaneous representation in local coordinates of scatterers j and j' of the Green's tensor, $\mathbf{G}_{\mathrm{B}}(\mathbf{r}, \mathbf{r}')$. The separation matrix is defined in Appendix B.1 in closed form, but in spite of this, efficient evaluation of it is complicated by the fact that it depends on seven inputs (four indices and three components of the vector $\mathbf{b}$).

The use of the separation matrices is well-known in scattering calculations, and as reviewed in Ref. [41] the direct evaluation of these for many indices, as is done in the present implementation, is an inefficient scheme. In that reference, several alternative routes for more efficient evaluations of the separation matrices are proposed, and upon extending to configurations with $N \gg 10$ it may be worthwhile to pursue one of these for decreasing the computation time further. We do not go into the details here, but simply note that improvements, allowing for scaling of the formalism to larger systems, are possible, as discussed above.

As a final remark, we note that eventually, for sufficiently large N and/or $l_{\max}$, the explicit evaluation of the inverse matrix in Eq. (3.16) will become the bottleneck, and by then iterative schemes for computing it will be necessary.

4.5 Summary

The purpose of the present chapter has been to investigate the convergence of the computations and to benchmark the calculations of the cross sections. Concerning convergence, we established that the local relative error, evaluated at the boundaries of the scatterers, is a sufficient measure for verifying convergence. Likewise, we concluded that convergence becomes increasingly harder to obtain as the distance between the scatterers is decreased. Investigation of the dipole approximation revealed that it breaks down when the distance between the scatterers decreases below the scatterer radius, $d/R \lesssim 1$. These two points emphasize the necessity for the present formalism when analyzing closely spaced metal particles, as we do in the following chapter, and question the use of simpler methods, such as the dipole approximation and the quasistatic approximation. Finally, we in the last section of the chapter discussed the computation times of the present implementation and gave several suggestions for decreasing this time.

Chapter 5

Properties of Plasmonic Dimers and Chains

> *Plasmonics is one of those small-scale topics where good people can do interesting things with modest resources, that too is one of the lures.*
>
> Bill Barnes, *Plasmonics: Fundamentals and Applications*

In this chapter, we explore the formalism developed in Chapter 3 for analyzing plasmonic dimers and chains. Specifically, we analyze cross section spectra, resulting from incoming fields with different polarizations and for scatterers of different sizes. We investigate and quantify how the resonances of the two types of systems depend on the distance between the metal particles for the dimer, and on the number of particles for the chain. Likewise, we visualize some of the associated localized surface plasmons, in the form of quasinormal modes, and finally compute the Green's tensor, the field from a dipole emitter, for the dimer configuration.

5.1 Setting

5.1.1 Parameter Choices

The possible variations, i.e. choice of materials, sizes of scatterers, relative positioning of scatterers, direction and polarization of the incoming field etc., are many and we shall fix some of these and vary others. We consider again $\epsilon_{\text{B}} = 2.25$ and let the scatterers be made of Ag, modeled by the Drude parameters in Eqs. (2.37a). Furthermore, we will consider scatterers aligned along one axis, the y-axis and henceforth termed the scatterer

axis, and with two different radii, $R = 10$ nm and $R = 25$ nm. In Section 5.2, we consider a dimer, $N = 2$, and vary the gap between the spheres, d, while in Section 5.3 we fix the gap, $d = R$, and consider chains of different lengths by varying N.

Concerning the incoming field, we will consider two configurations, specified by the direction of $\mathbf{k}_\mathrm{B}$ and the polarization:

> **Longitudinal:** $\mathbf{k}_\mathrm{B}$ perpendicular to scatterer axis, polarization parallel to scatterer axis: $\mathbf{k}_\mathrm{B} = k_\mathrm{B}\hat{z}$, $\mathbf{e}_\mathrm{B} = \hat{y}$.
>
> **Transverse:** $\mathbf{k}_\mathrm{B}$ perpendicular to scatterer axis, polarization perpendicular to scatterer axis: $\mathbf{k}_\mathrm{B} = k_\mathrm{B}\hat{z}$, $\mathbf{e}_\mathrm{B} = \hat{x}$.

We stress that the names of the two configurations refer to the polarization of the incoming field with respect to the scatterer axis. The overall polarization state of the incoming plane wave is in both cases transverse. As we shall see, the different polarizations give rise to different phenomena, and they are shown schematically as insets in the figures on the following pages.

As for the Mie scattering calculations (Section 4.3.1), we focus on the wavelengths 200 nm $\leq \lambda_0 \leq$ 800 nm and all spectra are computed with a total of 500 points within this range.

5.1.2 Data Representation

For each fixed N, R, d and choice of incoming field we have computed the spectrum of Q_scat and Q_abs in the wavelength range specified above. Even though we have made some specific choices about the parameters this has yielded many spectra; These are all included for reference in Appendix D. We refer the reader to the overview of the contents of that appendix on p. 89.

We shall a few times refer to some of the specific spectra, but in general we condensate the information from these and map the resonance wavelengths from the spectra as function of the relevant parameter (d/R or N). In the plots, each resonance is indicated by a circular marker (blue: scattering resonance, red: absorption resonance), and the size of the marker is proportional to the value of the relevant resonance efficiency, Q_scat or Q_abs. So the largest markers correspond to the dominant resonances in the spectra. The exact values that the markers are scaled to are included in Appendix D.3.

In the figures on the following pages, the top and the bottom panels show the results for longitudinal and transverse polarization, respectively. The insets in the figures schematically show the geometry, and the double-headed arrows indicate the polarizations of the incoming fields. In the caption of each figure, we list in brackets the exact appendix and page number where the complete set of spectra can be found.

5.2 Analyses of Plasmonic Dimers

As described above, we in this section focus on a dimer, $N = 2$, and with fixed R vary the gap between these relative to the radius, $0.1 \leq d/R \leq 15$. All simulations in the analyses of the dimer are performed with $l_\mathrm{max} = 8$.

5.2.1 $R = 10$ nm

The resonance wavelengths when $R = 10$ nm are shown for longitudinal and transverse polarization in Figs. 5.1(a) and 5.1(b), respectively.

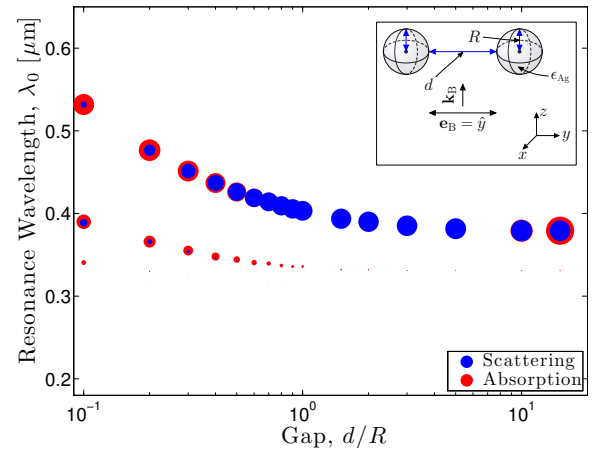

(a) Longitudinal: $\mathbf{k}_{\mathrm{B}} = k_{\mathrm{B}}\hat{z}$, $\mathbf{e}_{\mathrm{B}} = \hat{y}$ (Appendix D.1.1, p. 90ff).

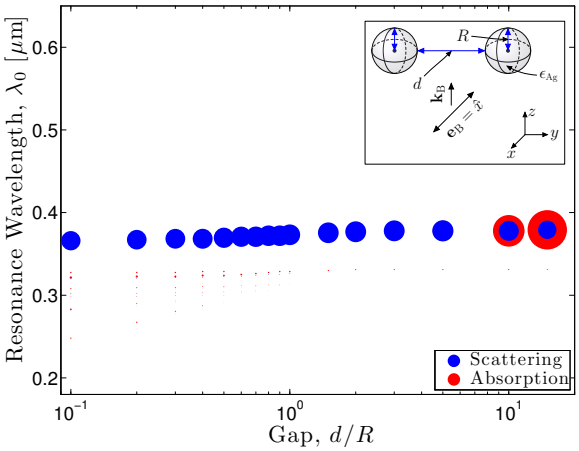

(b) Transverse: $\mathbf{k}_{\mathrm{B}} = k_{\mathrm{B}}\hat{z}$, $\mathbf{e}_{\mathrm{B}} = \hat{x}$ (Appendix D.1.1, p. 92ff).

Figure 5.1 Resonance wavelengths for the scattering and absorption cross sections for a dimer of Ag spheres. The gap distance between the scatterers, d, is varied for a fixed radius, R, and the marker sizes are proportional to the value of Q_{scat} (blue) and Q_{abs} (red) at the resonances. The background medium has $\epsilon_{\mathrm{B}} = 2.25$ and the radius is $R = 10$ nm. The incoming fields are as shown in the insets.

Examining first the longitudinal results, we see that at the largest scatterer spacing, $d/R = 15$, we essentially have the single-particle spectrum, Fig. 4.7(a), with a dipole resonance around $\lambda_0^{\mathrm{D}} = 370$ nm dominated by absorption and a tiny quadrupole around $\lambda_0^{\mathrm{H}} = 330$ nm. When the scatterers are far away from each other, we expect their mutual interaction to be weak which consequently explains this observation.

Subsequently, we decrease the scatterer spacing, and several changes occur: The scattering cross section in the intermediate range, $0.6 \lesssim d/R \lesssim 5$, becomes larger than the absorption cross section, implying that the dimer in this range is a more efficient scatterer than absorber. Secondly, the quadrupole resonance increases in magnitude

and is dominated by absorption, and looking very carefully in the range $d/R \lesssim 1$ other higher-order resonances also occur. Finally, and most importantly, the dipole resonance undergoes a distinct redshift, ending at the shortest gap, $d/R = 0.1$, at approximately $\lambda_0^{\mathrm{D}} = 525$ nm. The same happens for the quadrupole resonance, even though the absolute change in resonance wavelength is less pronounced than for the dipole resonance. Below we explain this behavior, but we first consider the results for the transverse polarization.

As in the longitudinal case, we at the largest gap roughly have the single-scatterer results. But as we then decrease the gap, the behavior is quite different from what we observed above: The dipole resonance remains almost at the same wavelength, undergoing, however, a slight blueshift, ending at $\lambda_0^{\mathrm{D}} = 365$ nm. We also note that scattering for $d/R \leq 5$ dominates, and that the higher-order resonances, while small, more clearly occur; The spectra at $d/R \lesssim 1$ look qualitatively like the energy states of an atom or a quantum dot. The gap distance in this analogy plays the role of the inverse size of the atom/quantum dot that has an increasing number of discrete states as the size increases. The results presented above, namely redshift and slight blueshift of the resonance wavelength under longitudinal and transverse polarizations, respectively, are in agreement with similar analyses in the literature [39, 42, 43].

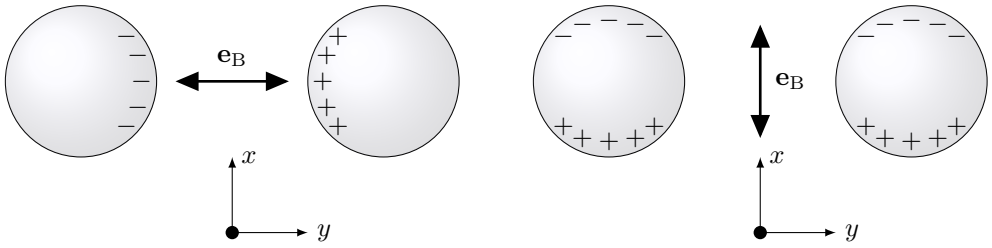

(a) Longitudinal polarization. (b) Transverse polarization.

Figure 5.2 Top view of two scatterers under longitudinal and transverse polarization. The double-headed arrows indicate the polarization of the incoming fields, and the distribution of charges on the surfaces of the scatterers is schematically indicated in the two cases.

We sketch a top view of the two scatterers under the two types of polarizations in Fig. 5.2. When the scatterers are sufficiently close to each other, and the incoming field oscillates in the longitudinal direction of the dimer, free charges in the metal, of opposite signs, accumulate on the surfaces of the scatterers. This charge difference across the gap may be interpreted as a small dipole [42] whose dipole moment, and potential energy, is proportional to the gap distance. Decreasing d/R thus decreases the potential energy which in effect redshifts the resonance of the system. Conversely, for a field oscillating in the transverse direction, charges of opposite signs are *not* induced on the surfaces in the gap, as shown in Fig. 5.2(b). It is less clear how to interpret the charge distributions in this case, but the slight blueshift, in the picture of induced dipoles, suggests a small repulsion across the gap. The repulsion of induced dipoles is used to explain the blueshift in Ref. [42]. The redistribution of charges in the latter case may also give rise to a plasmon, but a plasmon located on the individual spheres with no apparent interaction across the gap. In the next section, with $R = 25$ nm, we visualize this difference in the two cases by means of the associated quasinormal modes.

5.2.2 $R = 25$ nm

We have performed the same calculations for spheres with $R = 25$ nm, and later in this section we present results similar to those in Fig. 5.1. But we first return to the charge distributions explained in relation to Fig. 5.2.

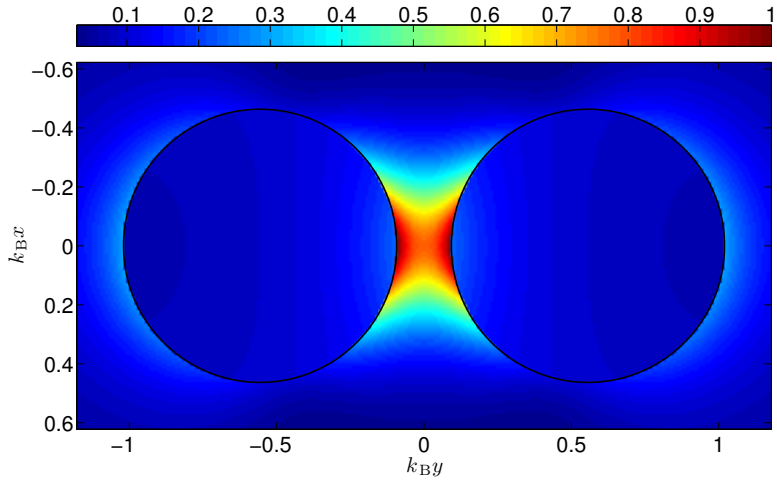

(a) Longitudinal quasinormal mode, $|\mathbf{f}_L(\mathbf{r})|$, at $\lambda_0^L = 505$ nm.

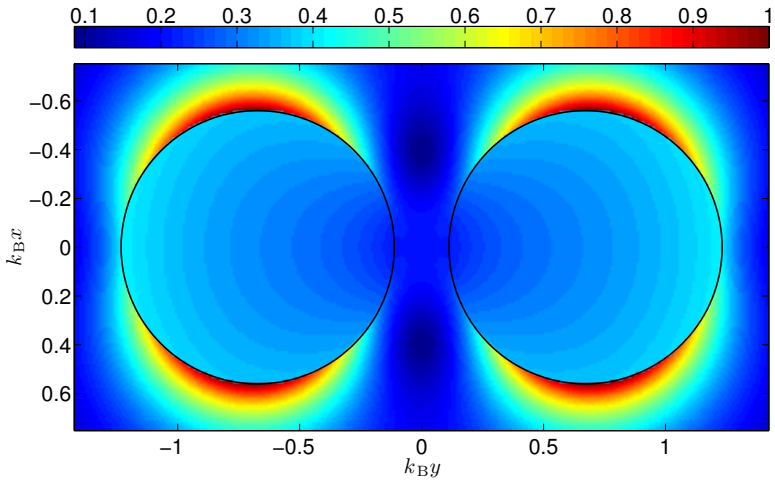

(b) Transverse quasinormal mode, $|\mathbf{f}_T(\mathbf{r})|$, at $\lambda_0^T = 415$ nm.

Figure 5.3 Absolute value of quasinormal modes, plotted in the $z = 0$-plane, in and around a dimer with radii $R = 25$ nm, and gap $d/R = 0.4$.

To visualize the fundamental difference between the two polarizations, it is customary in the literature to plot the field distributions from the scattering calculations, at resonances, inside and around the spheres. The resonances and associated plasmons may, however, be described and visualized more generally using the quasinormal modes, that we introduced in Section 3.5.3. They are self-consistent solutions of an "exciation-free" Lippmann-Schwinger equation, and the iterations to find the modes are particularly simple when we

have the spectra discussed in this section; We iterate from the resonance wavelengths and quickly obtain convergence.

For two scatterers with radii $R = 25$ nm and spaced the distance $d/R = 0.4$, we look for a quasinormal mode at $\lambda_0^{\mathrm{D}} = 0.505$ nm and for a mode at $\lambda_0^{\mathrm{D}} = 0.415$ nm; These correspond to the dipole resonances, for this choice of parameters, in Figs. 5.4(a) and 5.4(b), respectively, for the two polarizations. We therefore, based on the discussion in connection to Fig. 5.2, expect the former to be highly localized in the gap, and the latter to vanish (or at least be weak) in the gap, but localized on the surfaces of the individual spheres.

We determine the modes and plot their magnitudes in the $z = 0$-plane in Figs. 5.3(a) and 5.3(b), respectively. The modes can be normalized rigorously [36], but we choose a more pragmatic normalization: We divide the modes by their maximum magnitude in the domain shown in the figures. Since we are only looking at the qualitative features, this ad hoc normalization is justified. In the figures, the circumferences of the spheres are outlined in black.

The plots of the two modes are as expected: The quasinormal mode corresponding to the longitudinal polarization is highly localized in the gap between the scatterers, stemming from the charge difference across the gap (Fig. 5.2(a)). In contrast, the transverse quasinormal mode essentially vanishes in the gap, but is highly localized on the individual spheres, away from the gap (due to the charge distribution shown in Fig. 5.2(b)). As a side note, the two modes have Q-factors of $Q_{\mathrm{L}} = 5.7$ and $Q_{\mathrm{T}} = 4.2$, cf. Eq. (3.50), which are very small values in comparison with semiconductor microcavities [44]. Their extremely small mode volumes, in turn, imply that the important figure of merit Q-factor per mode volume can be comparable with the aforementioned microcavities [4]. The quasinormal mode $\mathbf{f}_{\mathrm{L}}(\mathbf{r})$ is also analyzed in [32] where the same Q-factor is indicated.

In conclusion for the quasinormal modes, their visualization have supported the ideas that were used to explain the resonance wavelength shifts, and we later visualize similar modes for $N > 2$ scatterers to further build upon this.

The resonance wavelengths for the two polarizations with $R = 25$ nm are shown in Fig. 5.4. The picture is essentially the same as in the previous case: For longitudinal polarization, the dipole resonance wavelength is clearly redshifted, while for transverse polarization a slight blueshift is observed. Likewise, we again observe the formation of many higher-order plasmons in the latter case as d/R decreases.

More interestingly, we note that the relative shift in resonance wavelength under longitudinal polarization is roughly the same as in the $R = 10$ nm-case, see Fig. 5.1(a). So the increase in radius of the scatterers has apparently not changed the way in which the dipole resonance redshifts. Inspired by this observation, we in the following section quantify how the resonance wavelengths, under longitudinal polarization, varies with gap distance. As we have seen in the spectra above, the dipole resonances for the scattering and absorption cross sections occur roughly at the same wavelengths, and we therefore base the following analyses on just one of them, the scattering cross section.

5.2.3 Resonance Peak Shift Ratio

We introduce the peak shift ratio via [39]

$$\Delta\lambda_0^{\mathrm{Res}} \equiv \frac{\lambda_0^{\mathrm{D}} - \lambda_0^{\mathrm{D,single}}}{\lambda_0^{\mathrm{D,single}}}, \tag{5.1}$$

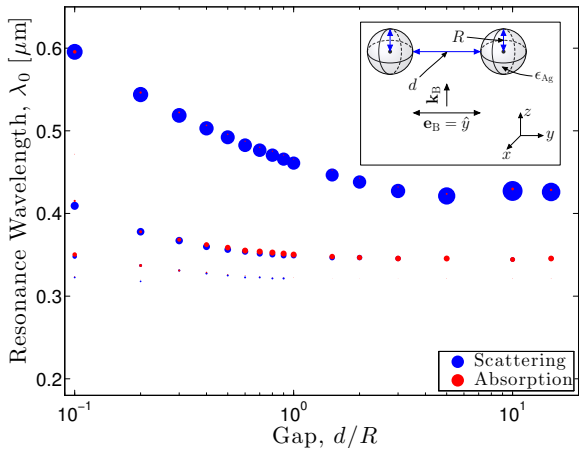

(a) Longitudinal: $\mathbf{k}_\mathrm{B} = k_\mathrm{B}\hat{z}$, $\mathbf{e}_\mathrm{B} = \hat{y}$ (Appendix D.1.2, p. 94ff).

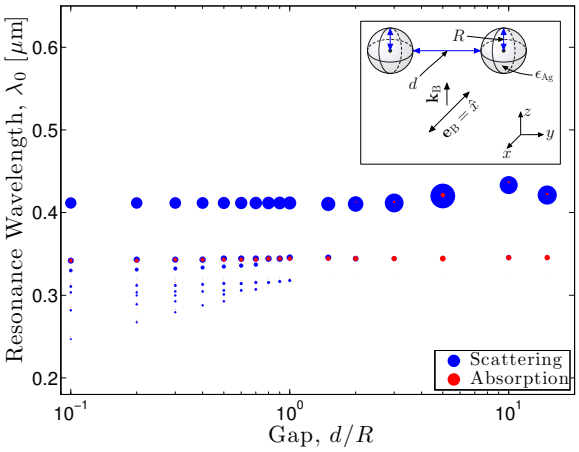

(b) Transverse: $\mathbf{k}_\mathrm{B} = k_\mathrm{B}\hat{z}$, $\mathbf{e}_\mathrm{B} = \hat{x}$ (Appendix D.1.2, p. 96ff).

Figure 5.4 Same description as for Fig. 5.1, but with $R = 25$ nm.

where $\lambda_0^{\mathrm{D,single}}$ is the dipole resonance wavelength for a single scatterer, i.e., the peaks in the Mie scattering calculations in Fig. 4.7. λ_0^{D} is the resonance wavelength, for longitudinal polarization, and as we have seen above, this quantity varies with the scatterer spacing. Later, we investigate its dependence on the number of scatterers in the chain, N, but here we have $\Delta\lambda_0^{\mathrm{Res}} \equiv \Delta\lambda_0^{\mathrm{Res}}(N, d) = \Delta\lambda_0^{\mathrm{Res}}(2, d)$.

The dependence of $\Delta\lambda_0^{\mathrm{Res}}$ on d has been investigated in the literature, with different outcomes: Jain *et al.* in Ref. [42] derive a so-called "Plasmon ruler equation" stating that $\Delta\lambda_0^{\mathrm{Res}} = A\exp\left(-(d/R)/\eta\right)$, where A is an amplitude and η is a characteristic decay length. The latter represents the distance over which the near-fields of the spheres effectively interact, and this model consequently has an appealing form. The authors derive the relation on the basis of both experimental results and simulations based on the discrete dipole approximation [45] (not to be confused with the dipole approximation

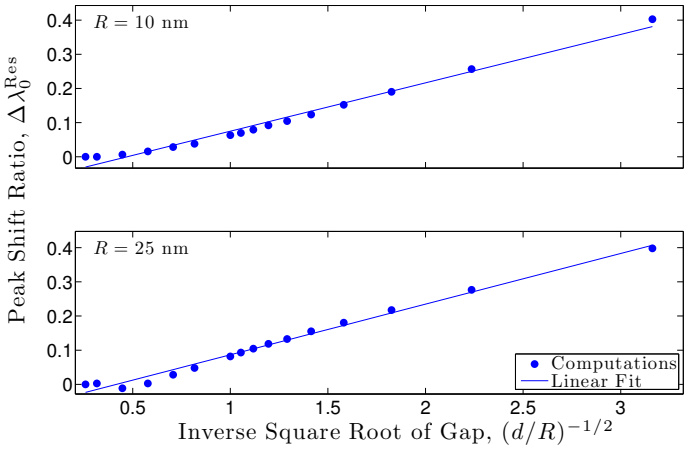

Figure 5.5 Peak shift ratios, $\Delta\lambda_0^{\mathrm{Res}}$, as function of $(d/R)^{-1/2}$, for the dimer under longitudinal polarization. Results for two radii, $R = 10$ nm and $R = 25$ nm, are shown.

used earlier in this work). Harris *et al.* in Ref. [39] perform similar analyses using a **T**-matrix approach [46]. They try to fit their results for $\Delta\lambda_0^{\mathrm{Res}}$ to an exponential of the above form, but do not find good agreement. In turn, they fit their peak shift ratios to an inverse dependence on the gap distance, $\Delta\lambda_0^{\mathrm{Res}} \sim 1/(d/R)$, and explain this behavior by the van der Waals forces between the induced dipoles between the spheres, that for small spacings also scale as $1/(d/R)$. Nevertheless, they do see some deviations from this overall behavior when simulating different systems.

In this context, we have computed the peak shift ratios, both for $R = 10$ nm and $R = 25$ nm, and tried to fit them both to an exponential dependence and to an inverse dependence; Neither, however, fit particularly well to these models. These attempts, that we do not show here, revealed that a slower decay for increasing d/R would be more suitable, and the fits to an inverse square root dependence

$$\Delta\lambda_0^{\mathrm{Res}}(2,d) = \eta_d \left(\frac{1}{d/R}\right)^{1/2}, \tag{5.2}$$

are shown in Fig. 5.5. In the figure, the dots are the data points, and the lines are the corresponding fits. We find $\eta_d = 0.14$ and $\eta_d = 0.15$ in the two cases. The fits are not perfect, but acceptable, with $R^2 = 0.983$ and $R^2 = 0.988$, respectively. What these results suggest, as compared to the aforementioned references, is a longer interaction distance of the plasmonic resonances on the spheres; The deviation from the single-scatterer resonance wavelength persists for larger scatterer spacings, than in the other proposed models.

There might be several reasons for the discrepancies between our results and those in the references. The size of the scatterers are smaller in Ref. [39] and larger in Ref. [42]. Likewise, the other references consider Au particles (we use Ag spheres), and the use of different background media might also influence. In the present calculations, the investigation of more configurations, e.g. with scatterers of different radii, made of different materials and embedded in different media, would be needed to establish any general law. However, the empirical relation in Eq. (5.2), verified for two different configurations, is a first contribution to the quantification of the effective interaction length of plasmons using the formalism developed in this work. For now we content

ourselves with this, and in the following sections proceed to chains of varying number of scatterers.

5.3 Analyses of Plasmonic Chains

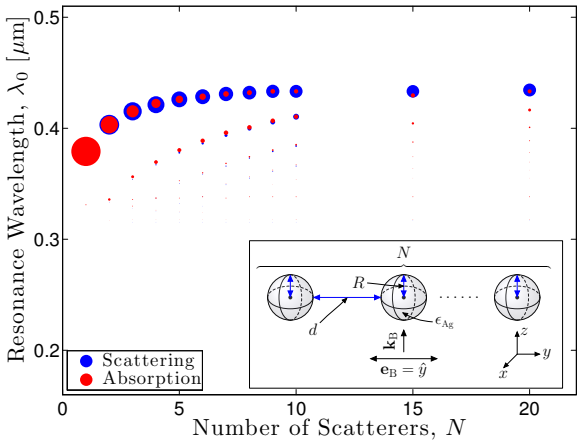

(a) Longitudinal: $\mathbf{k}_{\mathrm{B}} = k_{\mathrm{B}}\hat{z}$, $\mathbf{e}_{\mathrm{B}} = \hat{y}$ (Appendix D.2.1, p. 98ff).

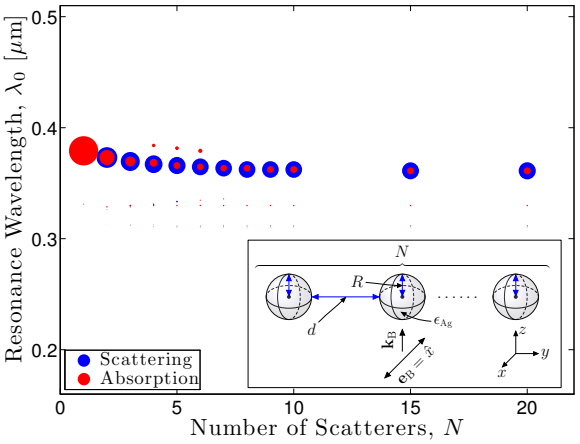

(b) Transverse: $\mathbf{k}_{\mathrm{B}} = k_{\mathrm{B}}\hat{z}$, $\mathbf{e}_{\mathrm{B}} = \hat{x}$ (Appendix D.2.1, p. 100ff).

Figure 5.6 Resonance wavelengths for the scattering and absorption cross sections for a chain of N Ag spheres. The gap distance between the scatterers is $d = R$ and the radius of the scatterers is $R = 10$ nm. The marker sizes are proportional to the value of Q_{scat} (blue) and Q_{abs} (red) at the resonances. The background medium has $\epsilon_{\mathrm{B}} = 2.25$, and the incoming fields are as shown in the insets.

We fix the gap between the scatterers at $d/R = 1$, with the same two radii as in the previous sections, and investigate the effect of adding more scatterers to the chain, $1 \leq N \leq 20$. As we saw in Section 4.4, the computation time scales as N^2 and as $(l_{\max} + 1)^4$, so the relatively large spacing between the scatterers, $d/R = 1$, is chosen to

allow simulations with a lower value of $l_{\max} = 3$. In the $N = 2$ case, we may compare these results with those from the previous section, performed with $l_{\max} = 8$, and this comparison reveals that the $l_{\max} = 3$ and $d/R = 1$ results are accurate to within a relative error of less than 10^{-3} on the peak cross sections. The resonance wavelengths are the same for the two choices of $l_{\max}$.

5.3.1 $R = 10$ nm

We first consider the results with $R = 10$ nm, shown in Figs. 5.6(a) and 5.6(b) for longitudinal and transverse polarizations, respectively. The results show the same type of behavior for increasing N as we saw for decreasing d/R in the previous section: The dipole resonance in the longitudinal case redshifts, while the transverse resonance undergoes a slight blueshift. We also in both cases note the transition from dominant absorption to dominant scattering upon increasing N, and this can be explained by analogy with the single-scatterer situation: When the size of the single scatterer increases, scattering starts to dominate over absorption, as we saw in Fig. 4.7. Likewise, the appearance of higher-order resonances is observed, and in the transverse case three "sub-dipole resonances" occur for $N = 4, 5$ and 6. These manifest themselves as peaks in the spectra occuring at longer wavelengths than the dipole resonance, but this seems peculiar and is probably rather a numerical artifact than an actual physical state of the system.

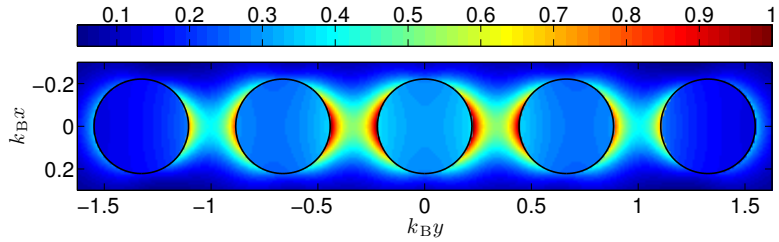

(a) Longitudinal quasinormal mode, $|\mathbf{f}_{\mathrm{L}}(\mathbf{r})|$, at $\lambda_0^{\mathrm{L}} = 426$ nm.

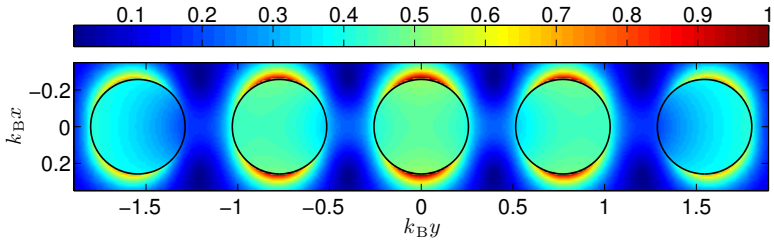

(b) Transverse quasinormal mode, $|\mathbf{f}_{\mathrm{T}}(\mathbf{r})|$, at $\lambda_0^{\mathrm{T}} = 366$ nm.

Figure 5.7 Absolute value of quasinormal modes, plotted in the $z = 0$-plane, in and around $N = 5$ scatterers of radii $R = 10$ nm, spaced a distance $d/R = 1$ from each other.

The results in the figure can essentially be explained in the same way that we explained those in Fig. 5.1: In the longitudinal case, charges of opposite signs are induced on the surfaces of the scatterers which in the gaps can be considered as small dipoles (see Fig. 5.2(a)). These result in attractive forces between the spheres, which effectively lowers the resonance energy, that is, redshifts the resonance wavelengths. However, the redshift saturates when a certain number of scatterers have been added, implying a maximum

interaction length along the chain. Conversely, the transverse case does not induce small dipoles in the gaps between the spheres (see Fig. 5.2(b)), which results in a slight blueshift. This overall picture under the two types of polarizations is found in similar analyses in Ref. [39].

To further appreciate this fundamental difference between the two cases, and in particular the different types of plasmons that they give rise to, we in Fig. 5.7 show the magnitude of two quasinormal modes for the $N = 5$ geometry under investigation. The quasinormal modes are as in Fig. 5.3 plotted in the $z = 0$-plane, and they are again normalized to have magnitudes between 0 and 1. The modes are found around the dipole resonances at $\lambda_0^{\mathrm{L}} = 426$ nm (longitudinal) $\lambda_0^{\mathrm{T}} = 0.366$ nm (transverse), cf. Fig. 5.6.

The picture is essentially the same as for the $N = 2$-modes that we considered earlier: Localization of the mode in the gaps in the longitudinal case, and localization on the particles, but not in the gaps, in the transverse case. The modes have Q-factors of $Q_{\mathrm{L}} = 17$ and $Q_{\mathrm{T}} = 17$.

5.3.2 $R = 25$ nm

We have performed the same calculations with spheres of radius $R = 25$ nm, and the resonance wavelengths in the two cases are shown in Fig. 5.8.

In the transverse case, Fig. 5.8(b), the picture is qualitatively the same as for $R = 10$ nm, namely a blueshift of the resonance wavelength for increasing number of scatterers. In the longitudinal case, Fig. 5.8(a), the similarity with the $R = 10$ nm-results is less obvious: The dipole resonance does redshift, but not in a monotonic way. In particular around $N = 6$-8, it is unclear why the dipole resonance wavelength suddenly drops. Going to the source, the spectra (see Appendix D.2.2, p. 102ff), it looks as if the dipole and the quadrupole resonances merge into one resonance, the new dipole resonance, loosely speaking, which at the intermediate chain lengths gives rise to a shorter resonance wavelength. However, these results are not well-understood and we do not analyze them further in the following.

5.3.3 Resonance Peak Shift Ratio

In contrast to the unclear results discussed above, the dipole resonances with $R = 10$ nm and longitudinal polarization, Fig. 5.6(a), appear to converge exponentially to an asymptotic value for large N. We therefore, inspired by the work in Ref. [39], assume that the peak shift ratio in this case can be described as follows

$$\Delta\lambda_0^{\mathrm{Res}}(N, R) = \Delta\lambda_0^{\mathrm{Asymp}} \exp\left(-\eta_N/(N-1)\right), \tag{5.3}$$

where $\Delta\lambda_0^{\mathrm{Asymp}}$ and η_N are the asymptotic peak shift ratio and the plasmon interaction length, respectively. The latter is given in units of chain periods, $N - 1$, and signifies the number of particles along the chain that the individual particle interacts with.

We have computed the peak shift ratios in the $R = 10$ nm-case, and we in Fig. 5.9 plot the logarithm of these against the inverse chain period, $1/(N-1)$. The dots are the data points, and the line is the corresponding linear fit. The fit is not excellent, $R^2 = 0.970$, but the data points follow the linear trend acceptably well. The general trend for the results presented in Ref. [39] is that the fit to the exponential dependence becomes more accurate, as d/R is decreased, and the fits therein for $d/R \sim 1$ have lower R^2 than the one found here. So the choice of $d/R = 1$ in the present calculations might be suboptimal for testing the validity of Eq. (5.3), but as explained in the beginning of this section,

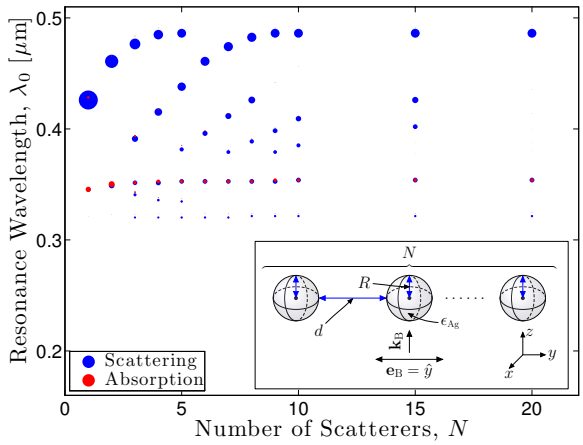

(a) Longitudinal: $\mathbf{k}_{\mathrm{B}} = k_{\mathrm{B}}\hat{z}$, $\mathbf{e}_{\mathrm{B}} = \hat{y}$ (Appendix D.2.2, p. 102ff).

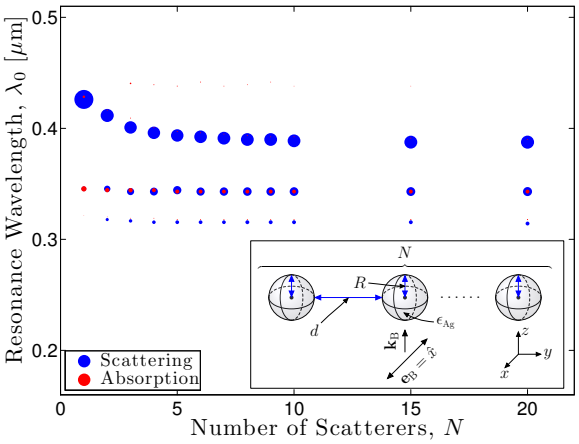

(b) Transverse: $\mathbf{k}_{\mathrm{B}} = k_{\mathrm{B}}\hat{z}$, $\mathbf{e}_{\mathrm{B}} = \hat{x}$ (Appendix D.2.2, p. 104ff).

Figure 5.8 Same description as for Fig. 5.6, but with $R = 25$ nm.

this choice was a trade-off with computation time. The fit yields $\eta_N = 1.87$, signifying interaction with approximately the two nearest neighbors in the chain.

As an outlook, it would be interesting to verify the dependence of $\Delta\lambda_0^{\mathrm{Res}}$ on the chain period for different scatterer spacings. In the view of the findings from the previous section, we would expect the asymptotic peak shift ratio to increase for decreasing values of d/R, and this assumption is supported by corresponding results in Ref. [39]. Furthermore, it would be of interest to investigate different choices of materials, and particles with different radii, to verify if the exponential behavior observed here is generally valid in a larger part of the parameter space.

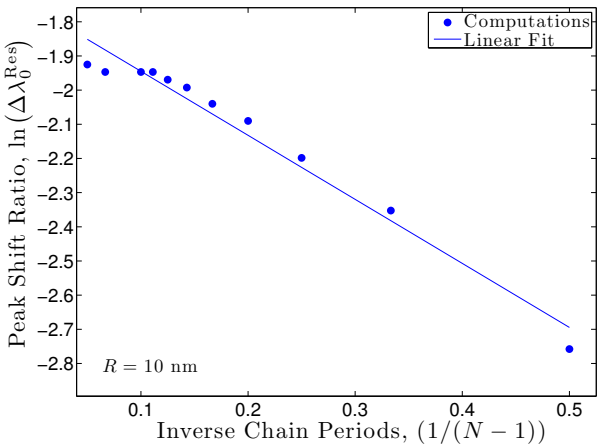

Figure 5.9 Logarithm of peak shift ratios, $\ln\left(\Delta\lambda_0^{\mathrm{Res}}\right)$, as function of the inverse chain period, $1/(N-1)$, for scatterers of radii $R = 10$ nm, spaced $d/R = 1$ and under longitudinal polarization.

5.4 Dipole Field for Resonant Dimer

As a final exploration of the plasmonic dimer, and the possibilities with the formalism, we in this section compute the Green's tensor that, as discussed in Section 3.5.2, is proportional to the field produced by a dipole emitter. Specifically, an emitter with dipole moment oriented along the direction α radiates a field described by the αth column in the Green's tensor. We may use the αth column of the background Green's tensor, $\mathbf{G}_{\mathrm{B}}(\mathbf{r}, \mathbf{r}_{\mathrm{d}})$, with $\mathbf{r}_{\mathrm{d}}$ at the position of the emitter, as the background field, and thus determine the dipole field using the formalism of Chapter 3.

We consider the geometry, for which we found quasinormal modes in Fig. 5.3, and orient the dipole moment along the y-axis and the x-axis, corresponding to the longitudinal and transverse polarizations, respectively. The real part of the Green's tensor diverges at $\mathbf{r} = \mathbf{r}_{\mathrm{d}}$, so to avoid this singularity we present the imaginary parts of the relevant elements of the Green's tensor. We compute the Green's tensor at the quasinormal frequencies given in Fig. 5.3, and in the former case plot $|\mathrm{Im}\left(\mathbf{G}^{yy}(\mathbf{r}, \mathbf{r}_{\mathrm{d}})\right)|$ and in the latter case plot $|\mathrm{Im}\left(\mathbf{G}^{xx}(\mathbf{r}, \mathbf{r}_{\mathrm{d}})\right)|$, see Figs. 5.10(a) and 5.10(b), respectively. The orientation of the dipole moment of the emitter in the two cases is schematically shown.

We first note that the dipole field along the dipole axis in Fig. 5.10(a) is very similar to the longitudinal quasinormal mode shown in Fig. 5.3(a): They are both highly localized in the gap. For the transverse orientation of the emitter, Fig. 5.10(b), the resemblance with the transverse quasinormal mode, Fig. 5.3(b), is likewise observed, being both strongly localized on the surfaces of the particles away from the gap. However, the dipole field, in contrast to the transverse quasinormal mode, is also moderately localized in the gap, in the vicinity of the emitter.

Another observation from the dipole fields is there relative magnitude: The longitudinal emitter produces a field that at the maximum is almost two orders of magnitude larger than that of the transverse emitter. The local density of states and the Purcell factor for an emitter oriented along the direction α is proportional to $\mathrm{Im}\left(\mathbf{G}^{\alpha\alpha}(\mathbf{r}_{\mathrm{d}}, \mathbf{r}_{\mathrm{d}})\right)$ [24, Chap. 8]. Consequently, this last observation implies that it is substantially more beneficial to orient an emitter along the longitudinal than the transverse direction to obtain large Purcell enhancement in this geometry. This is not a surprising conclusion, but the above

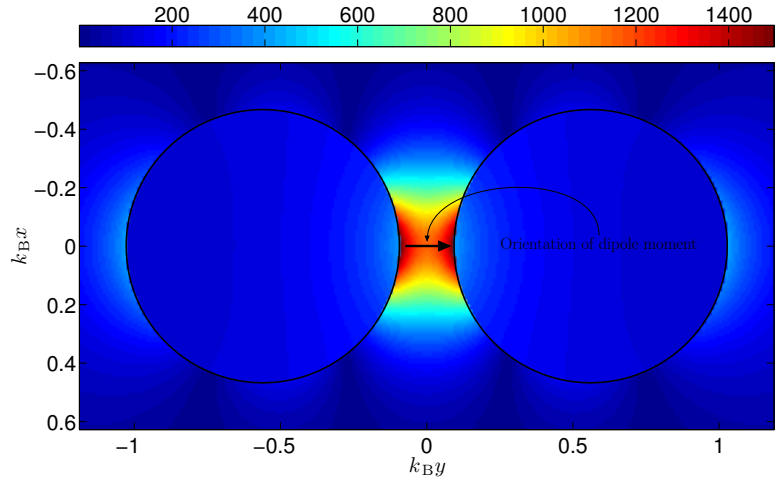

(a) $|\mathrm{Im}\,(\mathbf{G}^{yy}(\mathbf{r},\mathbf{r}_{\mathrm{d}}))|$ at $\lambda_0 = 505$ nm.

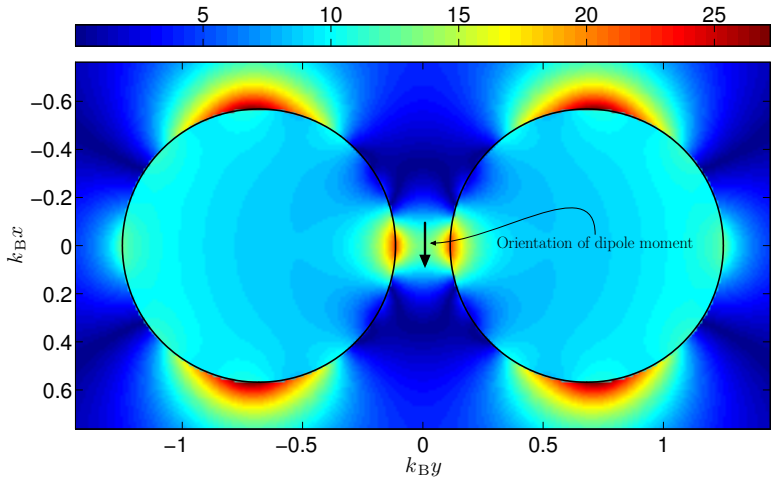

(b) $|\mathrm{Im}\,(\mathbf{G}^{xx}(\mathbf{r},\mathbf{r}_{\mathrm{d}}))|$ at $\lambda_0 = 415$ nm.

Figure 5.10 Absolute value of imaginary part of Green's tensor, $|\mathrm{Im}\,(\mathbf{G}^{\alpha\alpha}(\mathbf{r},\mathbf{r}_{\mathrm{d}}))|$, corresponding to the field produced by a dipole at $\mathbf{r}_{\mathrm{d}}$ and oriented along the direction α. Shown in the $z = 0$-plane, for two scatterers of radius $R = 25$ nm, spaced a distance $d/R = 0.4$.

calculation shows it quantitatively.

5.5 Summary

This chapter has served to explore the possibilities with the formalism developed in Chapter 3. The specific analyses were concerned with plasmonic dimers and chains, and we in detail analyzed how the resonances of such systems depend on various parameters. Specifically, we considered incident fields polarized along the dimer/chain axis (longi-

tudinal) and perpendicular to this axis (transverse), and saw how the former produces redshifts in the spectra, while the latter gives rise to blueshifts. This was explained by the induced charges on the metal particles, that in the longitudinal case produce small dipole-like states in the gaps between the particles, prompting an attraction between the particles.

We quantified how the resonance wavelengths, under longitudinal polarization, vary with gap size for the dimer, but agreement with models from the literature was not found. For the chains, in turn, we found an exponential convergence to an asymptotic redshifted resonance wavelength, that has been reported in the literature. The specific results suggested a next-nearest neighbor interaction length along the chain, also in agreement with similar results from the literature. We visualized the localized surface plasmons, which qualitatively supported the charge distribution-description mentioned above, and finally computed the Green's tensor, under resonant conditions, for the dimer.

The last calculation of the Green's tensor displays the possibilities with the present formalism. For optical microstructures, e.g. micropillars and photonic crystals, important concepts such as the local density of states and the Purcell factor are easily extractable upon calculation of the Green's tensor. So while we, in this and the previous chapter, have focused on systems of metallic spheres, the transition to analyses of microstructured semiconductor materials is easily done.

CHAPTER 6

Conclusion and Outlook

> *I am awaiting the day when people remember the fact that discovery does not work by deciding what you want and then discovering it.*
>
> N. David Mermin, *Physics Today: How not to create tigers*

In this final chapter of the thesis, we review the work presented in the preceding chapters, and provide an outlook for future work.

6.1 Review of Thesis

The outcome of the work presented in this thesis can be summarized in the following two points:

- A formalism for simulating the electric field, taken fully the vectorial nature of the field into account, for spherical scatterers embedded in a homogeneous 3D background medium. The formalism is based on the Lippmann-Schwinger equation and the electromagnetic Green's tensor, and all parts have been expressed analytically, the only approximation being imposed by the truncations of the sets of basis functions in the numerical implementation. As compared to similar solution techniques, e.g. from Refs. [16, 17], the use of the Lippmann-Schwinger equation provides an explicit error estimate which is an important tool in validating the computations. Likewise, as we return to in the following section, the use of the Green's tensor provides an intuitive way of extending the formalism to more complicated geometries, e.g. a layered geometry, which makes it an interesting candidate for modeling plasmonic solar cells.

- The use of the above formalism for analyzing dimers and chains of nanosize metallic particles. These systems exhibit highly localized and enhanced fields, and similarly very tunable spectral properties which, e.g., makes them promising candidates in applications as molecular and biosensing [42]. To realize technologies of this kind, a fundamental understanding of the properties of nanosize metal particles and their mutual interaction are important, and the results presented in the previous chapters are a step towards this.

In Chapter 2, we established the theoretical foundation that was build upon in the following chapters. Specifically, we presented the Lippmann-Schwinger equation that all following analyses were based on, and we introduced the cross sections used in the quantitative studies of metal particles in later chapters. The use of the Green's tensor gave an analytical expression for the far-field radiation pattern (scattering amplitude) from which the cross sections were expressed. Equally important, the error estimate of the Lippmann-Schwinger equation was introduced. The access to an explicit error estimate makes the formalism interesting in comparison with similar schemes, e.g. FDTD and FEM where the accuracy of the computations cannot be assessed in such a direct manner.

Chapter 3 presented a solution technique for the Lippmann-Schwinger equation in the specific geometry of spherical scatterers in a homogeneous 3D background medium. The field was expanded on spherical wavefunctions, and the associated expansion coefficients were found as solutions of a matrix equation. Most of the involved matrices were diagonal, but the matrix associated with the Green's tensor was non-diagonal. Nevertheless, all matrix elements were expressed analytically, and the procedure for achieving this with the Green's tensor matrix was outlined in some detail. Finally, the Lippmann-Schwinger equation was solved by assuming constant fields inside the scatterers, which produced an algebraic equation for these field values.

The error estimate was analyzed for a geometry of two scatterers in the beginning of Chapter 4, and these analyses revealed that convergence in the computations becomes increasingly harder to obtain as the distance between the scatterers is decreased. This was explained by the introduction of an increasingly smaller length scale in the problem, which required the inclusion of still more basis functions to be correctly resolved. In the limit of touching spheres, a non-local description for the fields is required [47], and while we did not address this problem further, the results, as expected, suffered from our local description in this limit. Subsequently, we compared the results from the constant-field approach to those from the full formalism, and this revealed two important things about the validity of the simpler approach: The radius of the scatterers must be $R \lesssim 1$ nm, and the distance between the scatterers has to be at least a couple of radii, $d \gtrsim 3R$. The simple approach of constant fields is often taken, in particular when $R \ll \lambda_0$, due to its simplicity. But our results showed that this produces faulty results if the spacing between the scatterers is $d \lesssim 3R$, which is often disregarded in the literature. We presented calculations of cross sections for benchmarking against known results in the literature, and the chapter was concluded by an analysis of the computation time and scalability of the present implementation of the formalism. This time scales as the number of scatterers squared, $t \propto N^2$, but more severely it scales as $t \propto (l_{\max} + 1)^4$. The latter fact currently puts the most restrictive limitations on the sizes and complexity of the systems we can treat, and suggestions were given for possible improvements.

Finally, we in Chapter 5 focused on dimers and chains of nanosize Ag particles. For the dimers, we analyzed scattering and absorption cross section spectra by varying the polarization of the incoming field and the distance between the scatterers. Under

polarization parallel with the dimer axis, a pronounced redshift of the resonance wavelength was found upon decreasing the distance between the particles. We quantified the relative redshift, through the peak shift ratio, $\Delta\lambda_0^{\mathrm{Res}}$, and for two different radii of the scatterers, $R = 10$ nm and $R = 25$ nm, we found that $\Delta\lambda_0^{\mathrm{Res}} \sim (d/R)^{-1/2}$, which is a softer dependence on the particle spacing than reported earlier. The correlation of the resonance variation and the distance between the particles may be used to measure distances on the nanoscale, by monitoring the spectra of the dimer. A possible application could be real-time monitoring in biological systems [48]. For the chains, we varied the number of particles and observed, under polarization along the chain axis, a redshift in resonance wavelength as more particles were added. Additionally, an exponential saturation of this redshift appeared, and a fit of the data revealed a next nearest-neighbor interaction of the particles on the chain. For both the dimer and the chain, we explained the redshift by the induction of charges of opposite signs in the gaps, and this was visualized through the associated quasinormal modes, corresponding to the localized surface plasmons. Finally, we computed the Green's tensor for the dimer, that is, the field produced by a dipole emitter between the two particles. It was computed at wavelengths corresponding to resonances of the system, and for a dipole emitter oriented along the dimer axis, this gave rise to a large and highly localized field, and connection to the local density of states and the Purcell factor was made. The last point ties closely with the outlook for the present work which we present in the following section.

6.2 Outlook

We have in the specific calculations in this thesis focused on nanosize plasmonic particles. This, as discussed briefly in the introductory chapter, is a very active field of research, and much effort is being put into the understanding of the properties of metal objects on the nanoscale. However, the formalism developed in Chapter 3 may equally well be applied for studying optical microstructures. With the restriction to spherical scatterers, an obvious system is photonic crystals where the localization or guiding of light, through the formation of photonic bandgaps, are interesting phenomena [49]. As discussed above and shown in the previous chapter, important quantities like the local density of states and the Purcell factor can, without doing new algebra or writing new MATLAB code, be computed with the present formalism. We omit more details here, but simply a last time stress that both optical microstructures and plasmonic nanostructures may be modeled with the formalism developed in this thesis.

Modeling of plasmonic solar cells using dyadic Green's functions has been investigated in Ref. [50]. The authors embed a dipole emitter in a three-layer geometry and analyze the effect of varying, e.g., the position and orientation of this emitter. As mentioned in the first chapter, the formalism developed in this work cannot simulate a realistic plasmonic thin-film solar cell that inherently involves a layered geometry. To address this, we in the following outline how the extension to layered geometries may be carried out.

A layered geometry can in its simplest form be represented by two infinite half-spaces, as shown schematically in Fig. 6.1. The interface is positioned at $z = 0$, and the half-space at $z > 0$ ($z < 0$) has permittivity $\epsilon_{\mathrm{B,U}}$ ($\epsilon_{\mathrm{B,L}}$). For visual clarity, the lower half-space is shown as a slab, but it extends over the entire xy-plane. In the sketch, two scatterers, spaced a distance d_{s}, are positioned a distance d_{i} above the interface. The effect of impinging plane waves in this system are then considered, in particular to investigate how to increase the transmission into the lower half space, e.g. by varying d_{s} and d_{i}.

The introduction of the interface quite naturally alters the Green's tensor describing

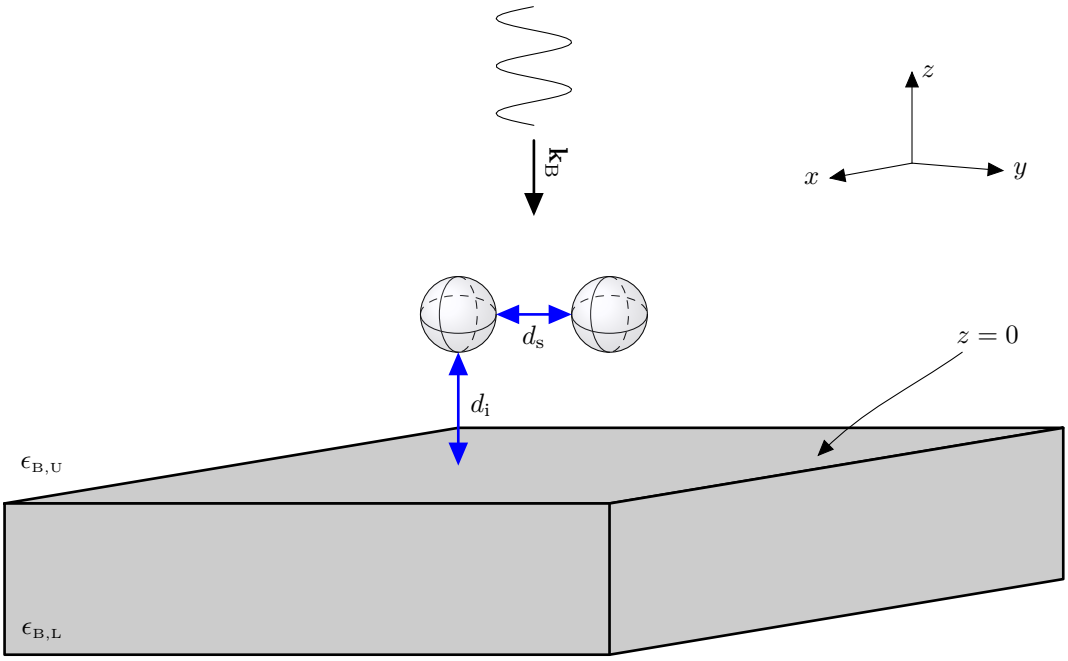

Figure 6.1 Sketch of a layered geometry, consisting of two infinite half-spaces of permittivities $\epsilon_{\mathrm{B,U}}$ ($z > 0$) and $\epsilon_{\mathrm{B,L}}$ ($z < 0$), respectively. Two spherical scatterers, spaced the distance d_s, are embedded a distance d_i above the interface. An incoming plane wave, impinging along the negative z-axis, is indicated.

the system; The field no longer only scatters on the spherical scatterers, but also at the interface. The reflections and transmissions at the interface can be accounted for via so-called generalized Fresnel coefficients, and if we restrict ourselves to scatterers in the upper half-space, as shown in the figure, the Green's tensors for the two half-spaces take the following forms [24, Chap. 10]

$$\mathbf{G}_\mathrm{U}(\mathbf{r},\mathbf{r}') = \mathbf{G}_\mathrm{B}(\mathbf{r},\mathbf{r}') + \mathbf{G}_\mathrm{refl}(\mathbf{r},\mathbf{r}'), \tag{6.1a}$$

$$\mathbf{G}_\mathrm{L}(\mathbf{r},\mathbf{r}') = \mathbf{G}_\mathrm{trans}(\mathbf{r},\mathbf{r}'). \tag{6.1b}$$

where $\mathbf{G}_\mathrm{B}(\mathbf{r},\mathbf{r}')$ is the Green's tensor for a homogeneous space with permittivity $\epsilon_{\mathrm{B,U}}$. $\mathbf{G}_\mathrm{refl}(\mathbf{r},\mathbf{r}')$ and $\mathbf{G}_\mathrm{trans}(\mathbf{r},\mathbf{r}')$ are the Green's tensors stemming from reflections and transmissions at the interface, respectively, and these are expressed via two-dimensional k-space integrals in the above reference. These are Sommerfeld-type integrals that cannot be solved analytically, and we omit the detailed expressions here. In turn, we note that the addition of an interface can be described, in the regions where the scatterers are embedded, by adding a secondary Green's tensor. This implies that we can reuse the matrix elements derived in Chapter 3 and determine the expansion coefficients for the field inside the scatterers by writing a new version of Eq. (3.16)

$$\mathbf{e} = \left[\mathbf{I} + \frac{L}{\epsilon_\mathrm{B}}\boldsymbol{\Delta\epsilon} - k_0^2\left(\mathbf{G} + \mathbf{G}_\mathrm{refl}\right)\boldsymbol{\Delta\epsilon}\right]^{-1}\mathbf{M}_\mathrm{B}\mathbf{e}_\mathrm{B}, \tag{6.2}$$

where $\mathbf{G}_\mathrm{refl}$ is a matrix with elements as in Eq. (3.17), with the change from $\mathbf{G}_\mathrm{B}$ to $\mathbf{G}_\mathrm{refl}$.

So the extension to a layered geometry can be carried out in an intuitive way, but the practical evaluation of the elements in $\mathbf{G}_{\text{refl}}$ may be very challenging. Paulus *et al.* in Ref. [51] propose a scheme for efficient numerical evaluation of the k-space integrals defining $\mathbf{G}_{\text{refl}}$, but even if this is achieved, the two integrations over scatterer volumes still remain. Secondly, the evaluation of the k-space integrals are performed in cylindrical coordinates which is not directly compatible with the spherical coordinates used in this work. One route for circumventing the remaining integrals is to apply the dipole approximation, as outlined in Section 3.7. We have already discussed the limitations of this approximation, but as a first approach to the more complicated layered geometry it might be feasible.

APPENDIX A

Basis Functions and Wavefunctions

In this appendix, we provide definitions of functions used in developing the formalism in Chapter 3. Likewise, various integral and differential results for these are presented. Where no other reference is given, definitions and results from Ref. [34, Chap. 3] are used.

A.1 Spherical Bessel and Hankel Functions

The radial parts of the basis functions are described by spherical Bessel functions defined as follows

$$j_l(x) \equiv \sqrt{\frac{\pi}{2x}} J_{l+1/2}(x), \tag{A.1}$$

where $J_{l+1/2}(x)$ is the Bessel function of the first kind of order $l + 1/2$. In analogy, the spherical Hankel functions of the first kind, used to describe the radial part of the outgoing spherical wavefunctions in Eq. (3.7), are defined as follows

$$h_l^{(1)}(x) \equiv \sqrt{\frac{\pi}{2x}} H_{l+1/2}^{(1)}(x), \tag{A.2}$$

where $H_{l+1/2}^{(1)}(x)$ is the Hankel function of the first kind of order $l + 1/2$.

A.2 Spherical Harmonics

The angular parts of the basis functions are described by normalized spherical harmonics that we define below. Likewise, we present various properties of these.

The normalized spherical harmonics are defined as

$$Y_l^m(\theta,\phi) \equiv (-1)^m \sqrt{\frac{2l+1}{4\pi}} \sqrt{\frac{(l-m)!}{(l+m)!}} P_l^m(\cos(\theta)) \exp(im\phi), \tag{A.3}$$

where $P_l^m(\cos(\theta_j))$ is the associated Legendre function of degree l and order m, that vanishes for $l < |m|$.

The normalized spherical harmonics satisfy the following orthonormality relation

$$\int_\Omega \{Y_l^m(\theta,\phi)\}^* Y_{l'}^{m'}(\theta,\phi)\, \mathrm{d}\Omega = \int_0^\pi \int_0^{2\pi} \{Y_l^m(\theta,\phi)\}^* Y_{l'}^{m'}(\theta,\phi) \sin(\theta)\, \mathrm{d}\phi\, \mathrm{d}\theta = \delta_{l\,l'}\delta_{m\,m'}, \tag{A.4}$$

where we introduced the solid angle element, $\mathrm{d}\Omega \equiv \sin(\theta)\, \mathrm{d}\phi\, \mathrm{d}\theta$. The integral of the Spherical harmonics over the solid angle vanishes unless $l = m = 0$

$$\int_\Omega Y_l^m(\theta,\phi)\, \mathrm{d}\Omega = \sqrt{4\pi}\delta_{0l}\delta_{0m}. \tag{A.5}$$

A.3 Normalization of Basis Functions

In Section 3.2.1, we introduced the spherical basis functions and in this appendix we express the radial normalization constants, N_l^j and $N_l^{j,\mathrm{B}}$, introduced Eqs. (3.3)-(3.5), to satisfy Eqs. (3.11). We write out the integral

$$\begin{aligned}
\langle \psi_{m,j}^l | \psi_{m',j'}^{l'} \rangle &= \int \{\psi_{l,m}^j(\mathbf{r}_j)\}^{Y^*} \psi_{l',m'}^{j'}(\mathbf{r}_{j'})\, \mathrm{d}\mathbf{r} \\
&= \int \{S_j(\mathbf{r}) N_l^j j_l(k_j r_j) Y_l^m(\theta_j,\phi_j)\}^{Y^*} S_{j'}(\mathbf{r}) N_{l'}^{j'} j_{l'}(k_{j'} r_{j'}) Y_{l'}^{m'}(\theta_{j'},\phi_{j'})\, \mathrm{d}\mathbf{r} \\
&= \delta_{j\,j'} N_l^j N_{l'}^j \int_\Omega \{Y_l^m(\theta_j,\phi_j)\}^* Y_{l'}^{m'}(\theta_j,\phi_j)\, \mathrm{d}\Omega \int_0^{R_j} j_l(k_j r_j) j_{l'}(k_j r_j) r_j^2\, \mathrm{d}r_j \\
&= \delta_{j\,j'}\delta_{l\,l'}\delta_{m\,m'} \left(N_l^j\right)^2 \int_0^{R_j} j_l^2(k_j r_j) r_j^2\, \mathrm{d}r_j.
\end{aligned} \tag{A.6}$$

The orthonormality of the basis function, Eqs. (3.11), is then obtained if

$$N_l^j = \left(I_l^j\right)^{-1/2}, \tag{A.7a}$$

where [37]

$$\begin{aligned}
I_l^j &= \int_0^{R_j} j_l^2(k_j r_j) r_j^2\, \mathrm{d}r_j = \frac{\pi}{2k_j} \int_0^{R_j} J_{l+1/2}^2(k_j r_j) r_j\, \mathrm{d}r_j \\
&= \frac{\pi}{2k_j} R_j^2 \left[\frac{1}{2} J_{l+3/2}^2(k_j R_j) - \frac{(l+1/2)}{k_j R_j} J_{l+1/2}(k_j R_j) J_{l+3/2}(k_j R_j) + \frac{1}{2} J_{l+1/2}^2(k_j R_j)\right].
\end{aligned} \tag{A.7b}$$

The normalization of the background basis functions follows in the exact same way, and we thus have

$$N_l^{j,\mathrm{B}} = N_l^j(k_j \to k_\mathrm{B}). \tag{A.7c}$$

A.4 Overlap Between Basis Functions and Background Basis Functions

In this section, we express the overlap integral between the basis functions, $\psi^j_{l,m}(\mathbf{r}_j)$, and the background basis functions, $\psi^{j',\mathrm{B}}_{l',m'}(\mathbf{r}_{j'})$, expressed in Eq. (3.11c)

$$\begin{aligned}
\langle \psi^j_{l,m} | \psi^{j',\mathrm{B}}_{l',m'} \rangle &= \int \{\psi^j_{l,m}(\mathbf{r}_j)\}^{Y^*} \psi^{j',\mathrm{B}}_{l',m'}(\mathbf{r}_{j'}) \,\mathrm{d}\mathbf{r} \\
&= \int \{S_j(\mathbf{r}) N^j_l j_l(k_j r_j) Y^m_l(\theta_j,\phi_j)\}^{Y^*} S_{j'}(\mathbf{r}) N^{j',\mathrm{B}}_{l'} j_{l'}(k_{\mathrm{B}} r_{j'}) Y^{m'}_{l'}(\theta_{j'},\phi_{j'}) \,\mathrm{d}\mathbf{r} \\
&= \delta_{jj'} N^j_l N^{j,\mathrm{B}}_{l'} \int_\Omega \{Y^m_l(\theta_j,\phi_j)\}^* Y^{m'}_{l'}(\theta_j,\phi_j) \,\mathrm{d}\Omega \int_0^{R_j} j_l(k_j r_j) j_{l'}(k_{\mathrm{B}} r_j) r_j^2 \,\mathrm{d}r_j \\
&= \delta_{jj'} \delta_{ll'} \delta_{mm'} M^j_l
\end{aligned} \tag{A.8}$$

where [37]

$$\begin{aligned}
M^j_l &= N^j_l N^{j,\mathrm{B}}_l \int_0^{R_j} j_l(k_j r_j) j_l(k_{\mathrm{B}} r_j) r_j^2 \,\mathrm{d}r_j, \\
&= N^j_l N^{j,\mathrm{B}}_{l'} \frac{\pi}{2} \sqrt{\frac{1}{k_j k_{\mathrm{B}}}} \int_0^{R_j} J_{l+1/2}(k_j r_j) J_{l+1/2}(k_{\mathrm{B}} r_j) r_j \,\mathrm{d}r_j \\
&= N^j_l N^{j,\mathrm{B}}_{l'} \frac{\pi}{2} \sqrt{\frac{1}{k_j k_{\mathrm{B}}}} \Bigg\{ \frac{1}{k_j^2 - k_{\mathrm{B}}^2} \\
&\quad \times \Big[k_j R_j J_{l+1/2}(k_{\mathrm{B}} R_j) J_{l+3/2}(k_j R_j) - k_{\mathrm{B}} R_j J_{l+1/2}(k_j R_j) J_{l+3/2}(k_{\mathrm{B}} R_j) \Big] \Bigg\}.
\end{aligned} \tag{A.9}$$

A.5 Cartesian Derivatives of Spherical Wavefunctions

In this section, we express the results of acting two Cartesian partial derivatives, $\partial_\alpha \partial_{\alpha'}$, on the spherical wavefunctions. To that end we introduce the function $\Omega_{l,m}(\mathbf{r})$ which is any of the spherical wavefunctions we introduced in Chapter 3

$$\Omega_{l,m}(\mathbf{r}) \in \Big\{ \tilde{\psi}^j_{l,m}(\mathbf{r}_j),\, \tilde{\psi}^{j,\mathrm{B}}_{l,m}(\mathbf{r}_j),\, \varphi^{\mathrm{B}}_{l,m}(\mathbf{r}) \Big\}. \tag{A.10}$$

The results for the derivatives of the basis functions, $\psi^j_{l,m}(\mathbf{r}_j)$ and $\psi^{j,\mathrm{B}}_{l,m}(\mathbf{r}_j)$, are obtained by multiplication of the below identities with the radial normalization constants, cf. Eqs. (3.8). In the following, we suppress the explicit spatial dependence, $\Omega_{l,m} \equiv \Omega_{l,m}(\mathbf{r})$, and find

$$\begin{aligned}
\partial_x \partial_x \Omega_{l,m} = \frac{k^2}{4} \Big\{ & g^{+2,+2}_{++}(l,m) \Omega_{l+2,m+2} + g^{0,+2}_{++}(l,m) \Omega_{l,m+2} + g^{-2,+2}_{++}(l,m) \Omega_{l-2,m+2} \\
& + g^{+2,-2}_{--}(l,m) \Omega_{l+2,m-2} + g^{0,-2}_{--}(l,m) \Omega_{l,m-2} + g^{-2,-2}_{--}(l,m) \Omega_{l-2,m-2} \\
& + 2 \Big[g^{+2,0}_{-+}(l,m) \Omega_{l+2,m} + g^{0,0}_{-+}(l,m) \Omega_{l,m} + g^{-2,0}_{-+}(l,m) \Omega_{l-2,m} \Big] \Big\},
\end{aligned} \tag{A.11aa}$$

$$\partial_x \partial_y \Omega_{l,m} = \frac{k^2}{4i} \Big\{ g^{+2,+2}_{++}(l,m) \Omega_{l+2,m+2} + g^{0,+2}_{++}(l,m) \Omega_{l,m+2} + g^{-2,+2}_{++}(l,m) \Omega_{l-2,m+2}$$

$$- \left[g_{--}^{+2,-2}(l,m)\Omega_{l+2,m-2} + g_{--}^{0,-2}(l,m)\Omega_{l,m-2} + g_{--}^{-2,-2}(l,m)\Omega_{l-2,m-2} \right] \Bigg\}, \tag{A.11ab}$$

$$\partial_x \partial_z \Omega_{l,m} = \frac{k^2}{2} \Bigg\{ g_{0+}^{+2,+1}(l,m)\Omega_{l+2,m+1} + g_{0+}^{0,+1}(l,m)\Omega_{l,m+1} + g_{0+}^{-2,+1}(l,m)\Omega_{l-2,m+1} + g_{-0}^{+2,-1}(l,m)\Omega_{l+2,m-1} + g_{-0}^{0,-1}(l,m)\Omega_{l,m-1} + g_{-0}^{-2,-1}(l,m)\Omega_{l-2,m-1} \Bigg\}, \tag{A.11ac}$$

$$\begin{aligned} \partial_y \partial_y \Omega_{l,m} = -\frac{k^2}{4} \Bigg\{ & g_{++}^{+2,+2}(l,m)\Omega_{l+2,m+2} + g_{++}^{0,+2}(l,m)\Omega_{l,m+2} + g_{++}^{-2,+2}(l,m)\Omega_{l-2,m+2} \\ & + g_{--}^{+2,-2}(l,m)\Omega_{l+2,m-2} + g_{--}^{0,-2}(l,m)\Omega_{l,m-2} + g_{--}^{-2,-2}(l,m)\Omega_{l-2,m-2} \\ & - 2\left[g_{-+}^{+2,0}(l,m)\Omega_{l+2,m} + g_{-+}^{0,0}(l,m)\Omega_{l,m} + g_{-+}^{-2,0}(l,m)\Omega_{l-2,m} \right] \Bigg\}, \end{aligned} \tag{A.11ad}$$

$$\partial_y \partial_z \Omega_{l,m} = \frac{k^2}{2i} \Bigg\{ g_{0+}^{+2,+1}(l,m)\Omega_{l+2,m+1} + g_{0+}^{0,+1}(l,m)\Omega_{l,m+1} + g_{0+}^{-2,+1}(l,m)\Omega_{l-2,m+1} - \left[g_{-0}^{+2,-1}(l,m)\Omega_{l+2,m-1} + g_{-0}^{0,-1}(l,m)\Omega_{l,m-1} + g_{-0}^{-2,-1}(l,m)\Omega_{l-2,m-1} \right] \Bigg\}, \tag{A.11ae}$$

$$\partial_z \partial_z \Omega_{l,m} = k^2 \Bigg\{ g_{00}^{+2,0}(l,m)\Omega_{l+2,m} + g_{00}^{0,0}(l,m)\Omega_{l,m} + g_{00}^{-2,0}(l,m)\Omega_{l-2,m} \Bigg\}, \tag{A.11af}$$

where k refers to the wave number of the particular $\Omega_{l,m}$; For the background functions $k = k_{\mathrm{B}}$ and for the scatterer functions $k = k_j$. The g-coefficients are

$$g_{++}^{+2,+2}(l,m) = \sqrt{\frac{(l+m+2)(l+m+1)}{(2l+1)(2l+3)}} \sqrt{\frac{(l+m+4)(l+m+3)}{(2l+3)(2l+5)}}, \tag{A.11ba}$$

$$\begin{aligned} g_{++}^{0,+2}(l,m) = & \sqrt{\frac{(l+m+2)(l+m+1)}{(2l+1)(2l+3)}} \sqrt{\frac{(l-m)(l-m-1)}{4(l+1)^2-1}} \\ & + \sqrt{\frac{(l-m)(l-m-1)}{4l^2-1}} \sqrt{\frac{(l+m+2)(l+m+1)}{(2l-1)(2l+1)}}, \end{aligned} \tag{A.11bb}$$

$$g_{++}^{-2,+2}(l,m) = \sqrt{\frac{(l-m)(l-m-1)}{4l^2-1}} \sqrt{\frac{(l-m-2)(l-m-3)}{4(l-1)^2-1}}, \tag{A.11bc}$$

$$g_{--}^{+2,-2}(l,m) = \sqrt{\frac{(l-m+2)(l-m+1)}{(2l+1)(2l+3)}} \sqrt{\frac{(l-m+4)(l-m+3)}{(2l+3)(2l+5)}}, \tag{A.11bd}$$

$$\begin{aligned} g_{--}^{0,-2}(l,m) = & \sqrt{\frac{(l-m+2)(l-m+1)}{(2l+1)(2l+3)}} \sqrt{\frac{(l+m)(l+m-1)}{4(l+1)^2-1}} \\ & + \sqrt{\frac{(l+m)(l+m-1)}{4l^2-1}} \sqrt{\frac{(l-m+2)(l-m+1)}{(2l-1)(2l+1)}}, \end{aligned} \tag{A.11be}$$

$$g_{--}^{-2,-2}(l,m) = \sqrt{\frac{(l+m)(l+m-1)}{4l^2-1}}\sqrt{\frac{(l+m-2)(l+m-3)}{4(l-1)^2-1}}, \tag{A.11bf}$$

$$g_{-+}^{+2,0}(l,m) = -\sqrt{\frac{(l+m+2)(l+m+1)}{(2l+1)(2l+3)}}\sqrt{\frac{(l-m+1)(l-m+2)}{(2l+3)(2l+5)}}, \tag{A.11bg}$$

$$\begin{aligned} g_{-+}^{0,0}(l,m) = &-\sqrt{\frac{(l+m+2)(l+m+1)}{(2l+1)(2l+3)}}\sqrt{\frac{(l+m+2)(l+m+1)}{4(l+1)^2-1}} \\ &-\sqrt{\frac{(l-m)(l-m-1)}{4l^2-1}}\sqrt{\frac{(l-m)(l-m-1)}{(2l-1)(2l+1)}}, \end{aligned} \tag{A.11bh}$$

$$g_{-+}^{-2,0}(l,m) = -\sqrt{\frac{(l-m)(l-m-1)}{4l^2-1}}\sqrt{\frac{(l+m)(l+m-1)}{4(l-1)^2-1}}, \tag{A.11bi}$$

$$g_{0+}^{+2,+1}(l,m) = -\sqrt{\frac{(l+m+2)(l+m+1)}{(2l+1)(2l+3)}}\sqrt{\frac{(l+2)^2-(m+1)^2}{(2l+3)(2l+5)}}, \tag{A.11bj}$$

$$\begin{aligned} g_{0+}^{0,+1}(l,m) = &\sqrt{\frac{(l+m+2)(l+m+1)}{(2l+1)(2l+3)}}\sqrt{\frac{(l+1)^2-(m+1)^2}{4(l+1)^2-1}} \\ &-\sqrt{\frac{(l-m)(l-m-1)}{4l^2-1}}\sqrt{\frac{l^2-(m+1)^2}{(2l-1)(2l+1)}}, \end{aligned} \tag{A.11bk}$$

$$g_{0+}^{-2,+1}(l,m) = \sqrt{\frac{(l-m)(l-m-1)}{4l^2-1}}\sqrt{\frac{(l-1)^2-(m+1)^2}{4(l-1)^2-1}}, \tag{A.11bl}$$

$$g_{-0}^{+2,-1}(l,m) = \sqrt{\frac{(l+1)^2-m^2}{(2l+1)(2l+3)}}\sqrt{\frac{(l-m+3)(l-m+2)}{(2l+3)(2l+5)}}, \tag{A.11bm}$$

$$\begin{aligned} g_{-0}^{0,-1}(l,m) = &\sqrt{\frac{(l+1)^2-m^2}{(2l+1)(2l+3)}}\sqrt{\frac{(l+m+1)(l+m)}{4(l+1)^2-1}} \\ &-\sqrt{\frac{l^2-m^2}{4l^2-1}}\sqrt{\frac{(l-m+1)(l-m)}{(2l-1)(2l+1)}}, \end{aligned} \tag{A.11bn}$$

$$g_{-0}^{-2,-1}(l,m) = -\sqrt{\frac{l^2-m^2}{4l^2-1}}\sqrt{\frac{(l+m-1)(l+m-2)}{4(l-1)^2-1}}, \tag{A.11bo}$$

$$g_{00}^{+2,0}(l,m) = \sqrt{\frac{(l+1)^2-m^2}{(2l+1)(2l+3)}}\sqrt{\frac{(l+2)^2-m^2}{(2l+3)(2l+5)}}, \tag{A.11bp}$$

$$g_{00}^{0,0}(l,m) = -\sqrt{\frac{(l+1)^2-m^2}{(2l+1)(2l+3)}}\sqrt{\frac{(l+1)^2-m^2}{4(l+1)^2-1}}$$

$$- \sqrt{\frac{l^2 - m^2}{4l^2 - 1}} \sqrt{\frac{l^2 - m^2}{(2l-1)(2l+1)}}, \tag{A.11bq}$$

$$g_{00}^{-2,0}(l,m) = \sqrt{\frac{l^2 - m^2}{4l^2 - 1}} \sqrt{\frac{(l-1)^2 - m^2}{4(l-1)^2 - 1}}. \tag{A.11br}$$

Using [34, Theorem 3.25, p. 86], the above coefficients may be expressed more compactly in terms of Gaunt coefficients (see discussion of these in Appendix B.1), but since these are computationally demanding to obtain, we prefer the above explicit expressions that are easily evaluated numerically for many indices. On top of that, the above coefficients automatically vanish if they are evaluated for a "forbidden" basis function. Consider, for instance, the term $g_{00}^{-2,0}(l,m)\Omega_{l-2,m}$; For $l = 3$ and $m = 3$, $\Omega_{l-2,m} = \Omega_{1,3} = 0$, but this fact, in the general procedure of the following section, is not handled automatically. However, since $g_{00}^{-2,0}(3,3) = 0$, the use of the above coefficients ensures such terms to vanish.

APPENDIX B

Matrix Elements

This appendix presents the separation matrices and gives explicit expressions for the elements of the Green's tensor matrix, $\mathbf{G}$. Where no other reference is given, we refer to [34, Chap. 3].

B.1 Separation Matrices

In Section 3.3.2, we introduced the separation matrix, $S^{t,\mu}_{p,\nu}(\mathbf{b})$, in the two-center expansion of the scalar Green's functions, $g_{\mathrm{B}}(\mathbf{R})$, see Eq. (3.23). This quantity can be expressed as follows.

$$S^{t,\mu}_{p,\nu}(\mathbf{b}) = 4\pi(-1)^{\nu+\mu+Q}\sum_{q=0}^{Q}(-1)^{q}\varphi^{\mathrm{B}}_{q_0+2q,t-\mu}(\mathbf{b})\mathcal{G}(p,t;\nu,-\mu;q_0+2q), \tag{B.1}$$

where $\varphi^{\mathrm{B}}_{q_0+2q,t-\mu}(\mathbf{b})$ is an outgoing spherical background wavefunction. In the above, we have employed the following definitions

$$Q = \frac{p+\nu-q_0}{2}, \tag{B.2a}$$

$$q_0 = q_0(p,t;\nu,-\mu), \tag{B.2b}$$

$$q_0(p,t;\nu,\mu) = \begin{cases} |p-\nu| & \text{if } |p-\nu| \geq |t+\mu| \\ |p+\mu| & \text{if } |p-\nu| < |t+\mu| \text{ and } p+\nu+|t+\mu| \text{ is even} \\ |p+\mu|+1 & \text{if } |p-\nu| < |t+\mu| \text{ and } p+\nu+|t+\mu| \text{ is odd} \end{cases}, \tag{B.2c}$$

$$\mathcal{G}(p,t;\nu,\mu;q) = (-1)^{t+\mu}\int_{\Omega} Y^{t}_{p}(\theta,\phi)Y^{\mu}_{\nu}(\theta,\phi)Y^{-t-\mu}_{q}(\theta,\phi)\,\mathrm{d}\Omega, \tag{B.2d}$$

where $\mathcal{G}$ is a Gaunt coefficient. In the practical implementation of the present formalism, we compute the Gaunt coefficients by using the following expression

$$\mathcal{G}(p,t;\nu,\mu;q) = (-1)^{t+\mu}\sqrt{\frac{(2p+1)(2\nu+1)(2q+1)}{4\pi}}\begin{pmatrix} p & \nu & q \\ 0 & 0 & 0 \end{pmatrix}\begin{pmatrix} p & \nu & q \\ t & \mu & -t-\mu \end{pmatrix}, \tag{B.2e}$$

where the $\begin{pmatrix}\ldots\end{pmatrix}$ are so-called Wigner 3-j symbols. These, in the general case, can be expressed as sums of a finite number of terms, and Martin in Ref. [34] presents a thorough discussion of this and closed-form expressions in various special cases. We do not go more into detail about the specific expressions, but note that the defining integral, Eq. (B.2d), may be computed numerically and compared with a closed-form evaluation of a Gaunt coefficient.

Finally, we introduce another type of separation matrix, $\hat{S}^{t,\mu}_{p,\nu}(\mathbf{b})$, used to expand a basis function in scatterer j around the point $\mathbf{r}_j$ inside the scatterer (see Eq. (3.31))

$$\hat{S}^{t,\mu}_{p,\nu}(\mathbf{b}) = 4\pi(-1)^{\nu+\mu+Q}\sum_{q=0}^{Q}(-1)^q\tilde{\psi}^j_{q_0+2q,t-\mu}(\mathbf{b})\mathcal{G}(p,t;\nu,-\mu;q_0+2q). \tag{B.3}$$

B.2 Scattering Matrix Elements

In Section 3.3.2, we derived a generic scattering matrix element of the Green's tensor matrix, and we in this appendix write the matrix elements explicitly. Combining Eq. (3.28) and the expressions for the derivatives of the spherical wavefunctions from Appendix A.5, this is straightforward

$$\begin{aligned}\left[\mathbf{G}^{xx}_{j,j'}\right]^{m,m'}_{l,l'} &= ik_{\mathrm{B}}M^{j'}_{l'}M^{j}_{l}\Big/\left(N^{j',\mathrm{B}}_{l'}N^{j,\mathrm{B}}_{l}\right)\Big\{S^{m',m}_{l',l}(\mathbf{b}) + \frac{1}{4}\Big[g^{+2,+2}_{++}(l-2,m-2)S^{m',m-2}_{l',l-2}(\mathbf{b}) \\ &+ g^{0,+2}_{++}(l,m-2)S^{m',m-2}_{l',l}(\mathbf{b}) + g^{-2,+2}_{++}(l+2,m-2)S^{m',m-2}_{l',l+2}(\mathbf{b}) \\ &+ g^{+2,-2}_{--}(l-2,m+2)S^{m',m+2}_{l',l-2}(\mathbf{b}) + g^{0,-2}_{--}(l,m+2)S^{m',m+2}_{l',l}(\mathbf{b}) \\ &+ g^{-2,-2}_{--}(l+2,m+2)S^{m',m+2}_{l',l+2}(\mathbf{b}) + 2\Big(g^{+2,0}_{-+}(l-2,m)S^{m',m}_{l',l-2}(\mathbf{b}) \\ &+ g^{0,0}_{-+}(l,m)S^{m',m}_{l',l}(\mathbf{b}) + g^{-2,0}_{-+}(l+2,m)S^{m',m}_{l',l+2}(\mathbf{b})\Big)\Big]\Big\},\end{aligned} \tag{B.4a}$$

$$\begin{aligned}\left[\mathbf{G}^{xy}_{j,j'}\right]^{m,m'}_{l,l'} &= ik_{\mathrm{B}}M^{j'}_{l'}M^{j}_{l}\Big/\left(N^{j',\mathrm{B}}_{l'}N^{j,\mathrm{B}}_{l}\right)\frac{1}{4i}\Big\{g^{+2,+2}_{++}(l-2,m-2)S^{m',m-2}_{l',l-2}(\mathbf{b}) \\ &+ g^{0,+2}_{++}(l,m-2)S^{m',m-2}_{l',l}(\mathbf{b}) + g^{-2,+2}_{++}(l+2,m-2)S^{m',m-2}_{l',l+2}(\mathbf{b}) \\ &- \Big[g^{+2,-2}_{--}(l-2,m+2)S^{m',m+2}_{l',l-2}(\mathbf{b}) + g^{0,-2}_{--}(l,m+2)S^{m',m+2}_{l',l}(\mathbf{b}) \\ &+ g^{-2,-2}_{--}(l+2,m+2)S^{m',m+2}_{l',l+2}(\mathbf{b})\Big]\Big\},\end{aligned} \tag{B.4b}$$

$$\begin{aligned}\left[\mathbf{G}^{xz}_{j,j'}\right]^{m,m'}_{l,l'} &= ik_{\mathrm{B}}M^{j'}_{l'}M^{j}_{l}\Big/\left(N^{j',\mathrm{B}}_{l'}N^{j,\mathrm{B}}_{l}\right)\frac{1}{2}\Big\{g^{+2,+1}_{0+}(l-2,m-1)S^{m',m-1}_{l',l-2}(\mathbf{b}) \\ &+ g^{0,+1}_{0+}(l,m-1)S^{m',m-1}_{l',l}(\mathbf{b}) + g^{-2,+1}_{0+}(l+2,m-1)S^{m',m-1}_{l',l+2}(\mathbf{b})\end{aligned}$$

$$+ g_{-0}^{+2,-1}(l-2,m+1)S_{l',l-2}^{m',m+1}(\mathbf{b}) + g_{-0}^{0,-1}(l,m+1)S_{l',l}^{m',m+1}(\mathbf{b}) + g_{-0}^{-2,-1}(l+2,m+1)S_{l',l+2}^{m',m+1}(\mathbf{b})\Big\}, \tag{B.4c}$$

$$\left[\mathbf{G}_{j,j'}^{yy}\right]_{l,l'}^{m,m'} = ik_{\mathrm{B}}M_{l'}^{j'}M_{l}^{j}\Big/\left(N_{l'}^{j',\mathrm{B}}N_{l}^{j,\mathrm{B}}\right)\Big\{S_{l',l}^{m',m}(\mathbf{b}) - \frac{1}{4}\Big[g_{++}^{+2,+2}(l-2,m-2)S_{l',l-2}^{m',m-2}(\mathbf{b}) + g_{++}^{0,+2}(l,m-2)S_{l',l}^{m',m-2}(\mathbf{b}) + g_{++}^{-2,+2}(l+2,m-2)S_{l',l+2}^{m',m-2}(\mathbf{b}) + g_{--}^{+2,-2}(l-2,m+2)S_{l',l-2}^{m',m+2}(\mathbf{b}) + g_{--}^{0,-2}(l,m+2)S_{l',l}^{m',m+2}(\mathbf{b}) + g_{--}^{-2,-2}(l+2,m+2)S_{l',l+2}^{m',m+2}(\mathbf{b}) - 2\Big(g_{-+}^{+2,0}(l-2,m)S_{l',l-2}^{m',m}(\mathbf{b}) + g_{-+}^{0,0}(l,m)S_{l',l}^{m',m}(\mathbf{b}) + g_{-+}^{-2,0}(l+2,m)S_{l',l+2}^{m',m}(\mathbf{b})\Big)\Big]\Big\}, \tag{B.4d}$$

$$\left[\mathbf{G}_{j,j'}^{yz}\right]_{l,l'}^{m,m'} = ik_{\mathrm{B}}M_{l'}^{j'}M_{l}^{j}\Big/\left(N_{l'}^{j',\mathrm{B}}N_{l}^{j,\mathrm{B}}\right)\frac{1}{2i}\Big\{g_{0+}^{+2,+1}(l-2,m-1)S_{l',l-2}^{m',m-1}(\mathbf{b}) + g_{0+}^{0,+1}(l,m-1)S_{l',l}^{m',m-1}(\mathbf{b}) + g_{0+}^{-2,+1}(l+2,m-1)S_{l',l+2}^{m',m-1}(\mathbf{b}) - \Big[g_{-0}^{+2,-1}(l-2,m+1)S_{l',l-2}^{m',m+1}(\mathbf{b}) + g_{-0}^{0,-1}(l,m+1)S_{l',l}^{m',m+1}(\mathbf{b}) + g_{-0}^{-2,-1}(l+2,m+1)S_{l',l+2}^{m',m+1}(\mathbf{b})\Big]\Big\}, \tag{B.4e}$$

$$\left[\mathbf{G}_{j,j'}^{zz}\right]_{l,l'}^{m,m'} = ik_{\mathrm{B}}M_{l'}^{j'}M_{l}^{j}\Big/\left(N_{l'}^{j',\mathrm{B}}N_{l}^{j,\mathrm{B}}\right)\Big\{S_{l',l}^{m',m}(\mathbf{b}) + g_{00}^{+2,0}(l-2,m)S_{l',l-2}^{m',m}(\mathbf{b}) + g_{00}^{0,0}(l,m)S_{l',l}^{m',m}(\mathbf{b}) + g_{00}^{-2,0}(l+2,m)S_{l',l+2}^{m',m}(\mathbf{b})\Big\}. \tag{B.4f}$$

B.3 Proper and Improper Radial Integrals

In this section, we express the radial integrals needed for expressing the self terms of the Green's tensor matrix.

We first consider the integral $I_l^{\mathbb{R}^3-\delta V_j}$ which is defined as

$$I_l^{\mathbb{R}^3-\delta V_j} \equiv \lim_{\delta R'\to 0}\left(\int_{\delta R'}^{\infty} h_l^{(1)}(k_{\mathrm{B}}r')j_l(k_j r')r'^2\,\mathrm{d}r'\right). \tag{B.5}$$

Expanding the integrand for small arguments, we find

$$\lim_{r'\to 0}\left(h_l^{(1)}(k_{\mathrm{B}}r')j_l(k_j r')r'^2\right) = 0. \tag{B.6}$$

This implies that the integrand is bounded in the limit $r' \to 0$, and consequently we may evaluate the limit before expressing the integral

$$\begin{aligned} I_l^{\mathbb{R}^3-\delta V_j} &= \int_0^{\infty} h_l^{(1)}(k_{\mathrm{B}}r')j_l(k_j r')r'^2\,\mathrm{d}r' \\ &= \frac{\pi}{2\sqrt{k_{\mathrm{B}}k_j}}\int_0^{\infty} H_{l+1/2}(k_{\mathrm{B}}r')J_{l+1/2}(k_j r')r'\,\mathrm{d}r'. \end{aligned} \tag{B.7}$$

The remaining integral has been expressed in [52], and using this we finally have

$$I_l^{\mathbb{R}^3-\delta V_j} = -\frac{i}{k_{\mathrm{B}}}\frac{1}{k_j^2-k_{\mathrm{B}}^2}\left(\frac{k_j}{k_{\mathrm{B}}}\right)^l. \tag{B.8}$$

The general result in [52] contains two distributions, a Dirac delta function and a Cauchy Principal value, but since in our case $k_j \neq k_{\mathrm{B}}$, these terms can be discarded [53], leaving the above as the final result.

Next, we express the finite part radial integral [37]

$$\begin{aligned} I_l^{V_j} &\equiv \int_0^{R_j} h_l^{(1)}(k_{\mathrm{B}}r')j_l(k_j r')r'^2\,\mathrm{d}r' \\ &= \frac{M_l^j}{N_j^l N_j^{l,\mathrm{B}}} + i\frac{\pi}{2}\sqrt{\frac{1}{k_j k_{\mathrm{B}}}}\frac{1}{k_j^2-k_{\mathrm{B}}^2}\Big\{\Big[k_j R_j Y_{l+1/2}(k_{\mathrm{B}}R_j)J_{l+3/2}(k_j R_j) \\ &\quad - k_{\mathrm{B}}R_j J_{l+1/2}(k_j R_j)Y_{l+3/2}(k_{\mathrm{B}}R_j)\Big] - k_j^{l+1/2}k_{\mathrm{B}}^{-l-1/2}\frac{2}{\pi}\Big\}. \end{aligned} \tag{B.9}$$

Finally, using the integrals expressed above, we have the radial integral needed to express the B-integrals

$$I_l^{\mathbb{R}^3-V_j} \equiv \int_{R_j}^{\infty} h_l^{(1)}(k_{\mathrm{B}}r')j_l(k_j r')r'^2\,\mathrm{d}r' = I_l^{\mathbb{R}^3-\delta V_j} - I_l^{V_j}. \tag{B.10}$$

B.4 Self Terms: A-Integrals

We here present explicit expressions for the A-integrals, using the generic expression in Eq. (3.35).

Before we give the matrix elements, it is worthwhile to express the separation matrix involved in the A-integrals as follows

$$\hat{S}_{l',l}^{m',m}(\mathbf{r}_j) = \sum_{q=0}^{Q}\xi\,(l',m';l,m;q)\,\tilde{\psi}^j_{[q_0]_{l',l}^{m',m}+2q,m'-m}(\mathbf{r}_j), \tag{B.11}$$

where by comparison with Eq. (B.3)

$$\xi\,(l',m';l,m;q) \equiv 4\pi(-1)^{l+m+Q}(-1)^q\mathcal{G}(l',m';l,-m;q_0+2q), \tag{B.12}$$

and where Q and q_0 are defined as in Eq. (B.2). The point in writing the separation matrix in this way is to be able to track the indices involved in the inner product in Eq. (3.35). Combining this generic expression, the above expression for the separation matrix and the explicit expressions for Cartesian derivatives from Appendix A.5, we find

$$\begin{aligned} \left[A_{j,j}^{xx}\right]_{l,l'}^{m,m'} &= \frac{ik_{\mathrm{B}}}{\sqrt{4\pi}}N_{l'}^j/\left(N_l^j\right)\Big\{\xi\left(l',m';0,0;1/2(l-[q_0]_{l',0}^{m',0})\right)I_0^{\mathbb{R}^3-\delta V_j}\delta_{m\,m'} \\ &\quad + \frac{1}{4}\Big[\xi\left(l',m';2,-2;1/2(l-[q_0]_{l',2}^{m',-2})\right)g_{++}^{+2,+2}(0,0)I_2^{\mathbb{R}^3-\delta V_j}\delta_{m\,m'+2} \\ &\qquad + \xi\left(l',m';2,2;1/2(l-[q_0]_{l',2}^{m',2})\right)g_{--}^{+2,-2}(0,0)I_2^{\mathbb{R}^3-\delta V_j}\delta_{m\,m'-2} \\ &\qquad + 2\left(\xi\left(l',m';2,0;1/2(l-[q_0]_{l',2}^{m',0})\right)g_{-+}^{+2,0}(0,0)I_2^{\mathbb{R}^3-\delta V_j}\delta_{m\,m'}\right. \end{aligned}$$

$$+\xi\left(l',m';0,0;1/2(l-[q_0]^{m',0}_{l',0})\right)g^{0,0}_{-+}(0,0)I_0^{\mathbb{R}^3-\delta V_j}\delta_{m\,m'}\Big)\Big]\Big\}, \tag{B.13a}$$

$$\left[A^{xy}_{j,j}\right]^{m,m'}_{l,l'} = \frac{ik_{\mathrm{B}}}{\sqrt{4\pi}}N^j_{l'}/\left(N^j_l\right)\frac{1}{4i} \times\Big\{\xi\left(l',m';2,-2;1/2(l-[q_0]^{m',-2}_{l',2})\right)g^{+2,+2}_{++}(0,0)I_2^{\mathbb{R}^3-\delta V_j}\delta_{m\,m'+2} -\xi\left(l',m';2,2;1/2(l-[q_0]^{m',2}_{l',2})\right)g^{+2,-2}_{--}(0,0)I_2^{\mathbb{R}^3-\delta V_j}\delta_{m\,m'-2}\Big\}, \tag{B.13b}$$

$$\left[A^{xz}_{j,j}\right]^{m,m'}_{l,l'} = \frac{ik_{\mathrm{B}}}{\sqrt{4\pi}}N^j_{l'}/\left(N^j_l\right)\frac{1}{2} \times\Big\{-\xi\left(l',m';2,-1;1/2(l-[q_0]^{m',-1}_{l',2})\right)g^{+2,+1}_{0+}(0,0)I_2^{\mathbb{R}^3-\delta V_j}\delta_{m\,m'+1} -\xi\left(l',m';2,1;1/2(l-[q_0]^{m',1}_{l',2})\right)g^{+2,-2}_{--}(0,0)I_2^{\mathbb{R}^3-\delta V_j}\delta_{m\,m'-1}\Big\}, \tag{B.13c}$$

$$\begin{aligned}\left[A^{yy}_{j,j}\right]^{m,m'}_{l,l'} = \frac{ik_{\mathrm{B}}}{\sqrt{4\pi}}N^j_{l'}/\left(N^j_l\right)\Big\{&\xi\left(l',m';0,0;1/2(l-[q_0]^{m',0}_{l',0})\right)I_0^{\mathbb{R}^3-\delta V_j}\delta_{m\,m'}\\ &-\frac{1}{4}\Big[\xi\left(l',m';2,-2;1/2(l-[q_0]^{m',-2}_{l',2})\right)g^{+2,+2}_{++}(0,0)I_2^{\mathbb{R}^3-\delta V_j}\delta_{m\,m'+2}\\ &\quad+\xi\left(l',m';2,2;1/2(l-[q_0]^{m',2}_{l',2})\right)g^{+2,-2}_{--}(0,0)I_2^{\mathbb{R}^3-\delta V_j}\delta_{m\,m'-2}\\ &\quad-2\Big(\xi\left(l',m';2,0;1/2(l-[q_0]^{m',0}_{l',2})\right)g^{+2,0}_{-+}(0,0)I_2^{\mathbb{R}^3-\delta V_j}\delta_{m\,m'}\\ &\qquad+\xi\left(l',m';0,0;1/2(l-[q_0]^{m',0}_{l',0})\right)g^{0,0}_{-+}(0,0)I_0^{\mathbb{R}^3-\delta V_j}\delta_{m\,m'}\Big)\Big]\Big\},\end{aligned} \tag{B.13d}$$

$$\left[A^{yz}_{j,j}\right]^{m,m'}_{l,l'} = \frac{ik_{\mathrm{B}}}{\sqrt{4\pi}}N^j_{l'}/\left(N^j_l\right)\frac{1}{2i} \times\Big\{-\xi\left(l',m';2,-1;1/2(l-[q_0]^{m',-1}_{l',2})\right)g^{+2,+1}_{0+}(0,0)I_2^{\mathbb{R}^3-\delta V_j}\delta_{m\,m'+1} +\xi\left(l',m';2,1;1/2(l-[q_0]^{m',1}_{l',2})\right)g^{+2,-2}_{--}(0,0)I_2^{\mathbb{R}^3-\delta V_j}\delta_{m\,m'-1}\Big\}, \tag{B.13e}$$

$$\begin{aligned}\left[A^{zz}_{j,j}\right]^{m,m'}_{l,l'} = \frac{ik_{\mathrm{B}}}{\sqrt{4\pi}}N^j_{l'}/\left(N^j_l\right)\Big\{&\xi\left(l',m';0,0;1/2(l-[q_0]^{m',0}_{l',0})\right)I_0^{\mathbb{R}^3-\delta V_j}\delta_{m\,m'}\\ &+\xi\left(l',m';2,0;1/2(l-[q_0]^{m',0}_{l',2})\right)g^{+2,0}_{00}(0,0)I_2^{\mathbb{R}^3-\delta V_j}\delta_{m\,m'}\end{aligned}$$

$$+\xi\left(l',m';0,0;1/2(l-[q_0]^{m',0}_{l',0})\right)g^{0,0}_{00}(0,0)I_0^{\mathbb{R}^3-\delta V_j}\delta_{m\,m'}\Big\}. \quad \text{(B.13f)}$$

As discussed after Eq. (3.35), the inner product under the $\gamma_{\alpha,\alpha'}$-sum only contributes if the function $\tilde{\psi}^j_{l,m}(\mathbf{r}_j)$ is contained in the sum defining the separation matrix. To reflect this, the terms not satisfying this condition must vanish which can be ensured by imposing the following auxiliary definition of $\xi\,(l',m';l,m;q)$

$$\xi\,(l',m';l,m;q)=\begin{cases}4\pi(-1)^{l+m+Q}(-1)^q\mathcal{G}(l',m';l,-m;q_0+2q) & \text{if } 0\leq q\leq Q\\ 0 & \text{otherwise}\end{cases}, \quad \text{(B.14)}$$

which must be applied when expressing these in the A-integrals.

B.5 Self Terms: B-Integrals

In this section, we present explicitly the B-integrals, for which a generic expression was given in Eq. (3.39). We merely combine this with the expressions for the Cartesian derivatives of the wavefunctions (see Appendix A.5) and find

$$\begin{aligned}\left[B^{xx}_{j,j}\right]^{m,m'}_{l,l'} &= ik_{\mathrm{B}}M^j_l I_{l'}^{\mathbb{R}^3-V_j}N^j_{l'}/\left(N^{j,\mathrm{B}}_l\right)\Big\{\delta_{l\,l'}\delta_{m\,m'}+\frac{1}{4}\Big[g^{+2,+2}_{++}(l-2,m-2)\delta_{l-2\,l'}\delta_{m-2\,m'}\\ &+g^{0,+2}_{++}(l,m-2)\delta_{l\,l'}\delta_{m-2\,m'}+g^{-2,+2}_{++}(l+2,m-2)\delta_{l+2\,l'}\delta_{m-2\,m'}\\ &+g^{+2,-2}_{--}(l-2,m+2)\delta_{l-2\,l'}\delta_{m+2\,m'}+g^{0,-2}_{--}(l,m+2)\delta_{l\,l'}\delta_{m+2\,m'}\\ &+g^{-2,-2}_{--}(l+2,m+2)\delta_{l+2\,l'}\delta_{m+2\,m'}+2\Big(g^{+2,0}_{-+}(l-2,m)\delta_{l-2\,l'}\delta_{m\,m'}\\ &+g^{0,0}_{-+}(l,m)\delta_{l\,l'}\delta_{m\,m'}+g^{-2,0}_{-+}(l+2,m)\delta_{l+2\,l'}\delta_{m\,m'}\Big)\Big]\Big\}, \quad \text{(B.15a)}\end{aligned}$$

$$\begin{aligned}\left[B^{xy}_{j,j}\right]^{m,m'}_{l,l'} &= ik_{\mathrm{B}}M^j_l I_{l'}^{\mathbb{R}^3-V_j}N^j_{l'}/\left(N^{j,\mathrm{B}}_l\right)\frac{1}{4i}\Big\{g^{+2,+2}_{++}(l-2,m-2)\delta_{l-2\,l'}\delta_{m-2\,m'}\\ &+g^{0,+2}_{++}(l,m-2)\delta_{l\,l'}\delta_{m-2\,m'}+g^{-2,+2}_{++}(l+2,m-2)\delta_{l+2\,l'}\delta_{m-2\,m'}\\ &-\Big[g^{+2,-2}_{--}(l-2,m+2)\delta_{l-2\,l'}\delta_{m+2\,m'}+g^{0,-2}_{--}(l,m+2)\delta_{l\,l'}\delta_{m+2\,m'}\\ &+g^{-2,-2}_{--}(l+2,m+2)\delta_{l+2\,l'}\delta_{m+2\,m'}\Big]\Big\}, \quad \text{(B.15b)}\end{aligned}$$

$$\begin{aligned}\left[B^{xz}_{j,j}\right]^{m,m'}_{l,l'} &= ik_{\mathrm{B}}M^j_l I_{l'}^{\mathbb{R}^3-V_j}N^j_{l'}/\left(N^{j,\mathrm{B}}_l\right)\frac{1}{2}\Big\{g^{+2,+1}_{0+}(l-2,m-1)\delta_{l-2\,l'}\delta_{m-1\,m'}\\ &+g^{0,+1}_{0+}(l,m-1)\delta_{l\,l'}\delta_{m-1\,m'}+g^{-2,+1}_{0+}(l+2,m-1)\delta_{l+2\,l'}\delta_{m-1\,m'}\\ &+g^{+2,-1}_{-0}(l-2,m+1)\delta_{l-2\,l'}\delta_{m+1\,m'}+g^{0,-1}_{-0}(l,m+1)\delta_{l\,l'}\delta_{m+1\,m'}\\ &+g^{-2,-1}_{-0}(l+2,m+1)\delta_{l+2\,l'}\delta_{m+1\,m'}\Big\}, \quad \text{(B.15c)}\end{aligned}$$

$$\left[B^{yy}_{j,j}\right]^{m,m'}_{l,l'} = ik_{\mathrm{B}}M^j_l I_{l'}^{\mathbb{R}^3-V_j}N^j_{l'}/\left(N^{j,\mathrm{B}}_l\right)\Big\{\delta_{l\,l'}\delta_{m\,m'}-\frac{1}{4}\Big[g^{+2,+2}_{++}(l-2,m-2)\delta_{l-2\,l'}\delta_{m-2\,m'}$$

$$
\begin{aligned}
&+ g_{++}^{0,+2}(l,m-2)\delta_{l\,l'}\delta_{m-2\,m'} + g_{++}^{-2,+2}(l+2,m-2)\delta_{l+2\,l'}\delta_{m-2\,m'} \\
&+ g_{--}^{+2,-2}(l-2,m+2)\delta_{l-2\,l'}\delta_{m+2\,m'} + g_{--}^{0,-2}(l,m+2)\delta_{l\,l'}\delta_{m+2\,m'} \\
&+ g_{--}^{-2,-2}(l+2,m+2)\delta_{l+2\,l'}\delta_{m+2\,m'} - 2\left(g_{-+}^{+2,0}(l-2,m)\delta_{l-2\,l'}\delta_{m\,m'}\right. \\
&\left.+g_{-+}^{0,0}(l,m)\delta_{l\,l'}\delta_{m\,m'} + g_{-+}^{-2,0}(l+2,m)\delta_{l+2\,l'}\delta_{m\,m'}\right)\Big]\Big\}, \qquad \text{(B.15d)}
\end{aligned}
$$

$$
\begin{aligned}
\left[B_{j,j}^{yz}\right]_{l,l'}^{m,m'} &= ik_{\mathrm{B}}M_l^j I_{l'}^{\mathbb{R}^3-V_j} N_{l'}^j / \left(N_l^{j,\mathrm{B}}\right) \frac{1}{2i}\Big\{ g_{0+}^{+2,+1}(l-2,m-1)\delta_{l-2\,l'}\delta_{m-1\,m'} \\
&+ g_{0+}^{0,+1}(l,m-1)\delta_{l\,l'}\delta_{m-1\,m'} + g_{0+}^{-2,+1}(l+2,m-1)\delta_{l+2\,l'}\delta_{m-1\,m'} \\
&- \Big[g_{-0}^{+2,-1}(l-2,m+1)\delta_{l-2\,l'}\delta_{m+1\,m'} + g_{-0}^{0,-1}(l,m+1)\delta_{l\,l'}\delta_{m+1\,m'} \\
&+ g_{-0}^{-2,-1}(l+2,m+1)\delta_{l+2\,l'}\delta_{m+1\,m'}\Big]\Big\}, \qquad \text{(B.15e)}
\end{aligned}
$$

$$
\begin{aligned}
\left[B_{j,j}^{zz}\right]_{l,l'}^{m,m'} &= ik_{\mathrm{B}}M_l^j I_{l'}^{\mathbb{R}^3-V_j} N_{l'}^j / \left(N_l^{j,\mathrm{B}}\right) \Big\{ \delta_{l\,l'}\delta_{m\,m'} + g_{00}^{+2,0}(l-2,m)\delta_{l-2\,l'}\delta_{m\,m'} \\
&+ g_{00}^{0,0}(l,m)\delta_{l\,l'}\delta_{m\,m'} + g_{00}^{-2,0}(l+2,m)\delta_{l+2\,l'}\delta_{m\,m'}\Big\}. \qquad \text{(B.15f)}
\end{aligned}
$$

APPENDIX C

Miscellaneous from Lippmann-Schwinger Equation

This appendix gives various derivations and explicit expressions that for brevity were omitted in Chapter 3.

C.1 Matrix Equation for Expansion Coefficients

In this section, we derive the matrix equation for the expansion coefficients, Eq. (3.15).

We start by inserting the expansions in Eqs. (3.13a)-(3.13b) into the Lippmann-Schwinger equation, Eq. (3.1), and rearrange slightly

$$\left(1+\frac{\Delta\epsilon_j}{\epsilon_{\mathrm{B}}}\mathbf{L}\right)\sum_{\alpha}\sum_{l,m}e_{j\alpha lm}\psi^{j}_{l,m}(\mathbf{r}_j)\,\mathbf{e}_\alpha=\sum_{\alpha}\sum_{l,m}e^{\mathrm{B}}_{j\alpha lm}\psi^{j,\mathrm{B}}_{l,m}(\mathbf{r}_j)\,\mathbf{e}_\alpha + k_0^2\sum_{j'=1}^{N}\Delta\epsilon_{j'}\int_{V_{j'}}\mathbf{G}_{\mathrm{B}}(\mathbf{r}_j,\mathbf{r}'_{j'})\left(\sum_{\alpha'}\sum_{l',m'}e_{j'\alpha'l'm'}\psi^{j'}_{l',m'}(\mathbf{r}'_{j'})\,\mathbf{e}_{\alpha'}\right)\mathrm{d}\mathbf{r}'_{j'}. \tag{C.1}$$

We then project this equation onto $\psi^{\tilde{j}}_{\tilde{l},\tilde{m}}(\mathbf{r}_{\tilde{j}})\,\mathbf{e}_{\tilde{\alpha}}$ which produces

$$\left(1+\frac{\Delta\epsilon_{\tilde{j}}}{\epsilon_{\mathrm{B}}}\mathbf{L}^{\tilde{\alpha}\alpha}\right)e_{\tilde{j}\tilde{\alpha}\tilde{l}\tilde{m}}=M^{\tilde{j}}_{\tilde{l}}e^{\mathrm{B}}_{\tilde{j}\tilde{\alpha}\tilde{l}\tilde{m}}+k_0^2\sum_{j'=1}^{N}\Delta\epsilon_{j'}\sum_{\alpha'}\sum_{l',m'}\langle\psi^{\tilde{j}}_{\tilde{l},\tilde{m}}|\mathbf{G}^{\tilde{\alpha}\alpha'}_{\mathrm{B}}|\psi^{j'}_{l',m'}\rangle e_{j'\alpha'l'm'}, \tag{C.2}$$

where we used the orthonormality relations in Eqs. (3.11), and the fact that $\mathbf{e}^T_{\tilde{\alpha}}\,\mathbf{e}_\alpha=\delta_{\tilde{\alpha}\alpha}$. In the above equation, α and $\tilde{\alpha}$ are in principle both free indices, but since $\mathbf{L}^{\tilde{\alpha}\alpha}=\delta_{\tilde{\alpha}\alpha}/3$

(see Eq. (2.19)), we may set $\alpha = \tilde{\alpha}$ and subsequently replace all the tilded indices by untilded indices, without loss of generality

$$\left(1 + \frac{\Delta\epsilon_j}{\epsilon_{\mathrm{B}}}\mathbf{L}^{\alpha\alpha}\right) e_{j\alpha lm} = M_l^j e^{\mathrm{B}}_{j\alpha lm} + k_0^2 \sum_{j'=1}^{N} \Delta\epsilon_{j'} \sum_{\alpha'} \sum_{l',m'} \langle \psi^j_{l,m} | \mathbf{G}_{\mathrm{B}}^{\alpha\alpha'} | \psi^{j'}_{l',m'} \rangle e_{j'\alpha' l' m'}. \tag{C.3}$$

This last maneuver of changing the free indices from tilded to untilded in fact shows that we could have projected Eq. (C.1) onto $\psi^j_{l,m}(\mathbf{r}_j)\,\mathbf{e}_\alpha$ directly, originating from the fact that $\mathbf{L}$ is a diagonal dyadic. Yaghjian in Ref. [27] presents source dyadics for various exclusion geometries, and these are all diagonal dyadics so the procedure is justified even for other exclusion geometries than the spherical. The Green's tensor matrix elements are

$$\langle \psi^j_{l,m} | \mathbf{G}_{\mathrm{B}}^{\alpha\alpha'} | \psi^{j'}_{l',m'} \rangle \equiv \int_{V_j} \int_{V_{j'} - \delta V_{j'}} \{\psi^j_{l,m}(\mathbf{r}_j)\}^{Y^*} \mathbf{G}_{\mathrm{B}}^{\alpha\alpha'}(\mathbf{r}_j, \mathbf{r}'_{j'}) \psi^{j'}_{l',m'}(\mathbf{r}_{j'})\, \mathrm{d}\mathbf{r}'_{j'}\, \mathrm{d}\mathbf{r}_j, \tag{C.4}$$

where we have written the Principal volume integral, $\int_{V_{j'} - \delta V_{j'}} \mathrm{d}\mathbf{r}'_{j'}$, explicitly even though it is only needed when $j = j'$. We sum Eq. (C.3) over all free indices, j, α, l and m and have

$$\left(\mathbf{I} + \frac{L}{\epsilon_{\mathrm{B}}}\boldsymbol{\Delta\epsilon}\right)\mathbf{e} = \mathbf{M}_{\mathrm{B}}\mathbf{e}_{\mathrm{B}} + k_0^2 \mathbf{G}\boldsymbol{\Delta\epsilon}\mathbf{e}, \tag{C.5}$$

where $\mathbf{e}$ ($\mathbf{e}_{\mathrm{B}}$) contains the expansion coefficients of the field (background field) inside the scatterers. This is Eq. (3.15), and its solution is given formally in Eq. (3.16).

As discussed in Section 3.2.3, $\boldsymbol{\Delta\epsilon}$ and $\mathbf{M}_{\mathrm{B}}$ are diagonal matrices

$$\boldsymbol{\Delta\epsilon} = \begin{bmatrix} \Delta\epsilon_1\mathbf{I}_1 & \mathbf{0}_{12} & \dots & \mathbf{0}_{1j'} & \dots & \mathbf{0}_{1N} \\ \mathbf{0}_{21} & \Delta\epsilon_2\mathbf{I}_2 & \dots & \dots & \dots & \mathbf{0}_{2N} \\ \vdots & & \ddots & & & \vdots \\ \mathbf{0}_{j1} & \dots & & \Delta\epsilon_j\mathbf{I}_j & \dots & \mathbf{0}_{jN} \\ \vdots & & & & \ddots & \vdots \\ \mathbf{0}_{N1} & \dots & \dots & \dots & \dots & \Delta\epsilon_N\mathbf{I}_N \end{bmatrix}, \tag{C.6a}$$

$$\mathbf{M}_{\mathrm{B}} = \begin{bmatrix} M_0^1 & 0 & 0 & \dots & \dots & \dots & \dots & \dots & 0 \\ 0 & M_1^1 & 0 & \dots & \dots & \dots & \dots & \dots & 0 \\ 0 & 0 & M_1^1 & \dots & \dots & \dots & \dots & \dots & 0 \\ \vdots & & & \ddots & & & & & \vdots \\ 0 & \dots & \dots & \dots & M_0^2 & \dots & \dots & \dots & 0 \\ \vdots & & & & & \ddots & & & \vdots \\ 0 & \dots & \dots & \dots & \dots & \dots & M_0^N & \dots & 0 \\ \vdots & & & & & & & \ddots & \\ 0 & \dots & \dots & \dots & \dots & \dots & \dots & \dots & M^N_{l_{\max}} \end{bmatrix}, \tag{C.6b}$$

where $\mathbf{I}_j$ is an identity matrix of dimensions $K_j \times K_j$, $\mathbf{0}_{jj'}$ is a zero-matrix of dimensions $K_j \times K_{j'}$, and M_l^j is the overlap between $\psi^j_{l,m}(\mathbf{r}_j)$ and $\psi^{j,\mathrm{B}}_{l,m}(\mathbf{r}_j)$, see Eq. (3.11c). The elements of $\mathbf{M}_{\mathrm{B}}$ are expressed analytically in Appendix A.4.

$\mathbf{G}$ can be decomposed into submatrices as follows

$$\mathbf{G} = \begin{bmatrix} \mathbf{G}_{1,1} & \mathbf{G}_{1,2} & \dots & \mathbf{G}_{1,j'} & \dots & \mathbf{G}_{1,N} \\ \mathbf{G}_{2,1} & \mathbf{G}_{2,2} & \dots & \dots & \dots & \mathbf{G}_{2,N} \\ \vdots & & \ddots & & & \vdots \\ \mathbf{G}_{j,1} & \dots & & \mathbf{G}_{j,j'} & \dots & \mathbf{G}_{j,N} \\ \vdots & & & & \ddots & \vdots \\ \mathbf{G}_{N,1} & \dots & \dots & \dots & \dots & \mathbf{G}_{N,N} \end{bmatrix}, \tag{C.6ca}$$

$$\mathbf{G}_{j,j'} = \begin{bmatrix} \mathbf{G}_{j,j'}^{xx} & \mathbf{G}_{j,j'}^{xy} & \mathbf{G}_{j,j'}^{xz} \\ \mathbf{G}_{j,j'}^{xy} & \mathbf{G}_{j,j'}^{yy} & \mathbf{G}_{j,j'}^{yz} \\ \mathbf{G}_{j,j'}^{xz} & \mathbf{G}_{j,j'}^{yz} & \mathbf{G}_{j,j'}^{zz} \end{bmatrix}, \tag{C.6cb}$$

$$\mathbf{G}_{j,j'}^{\alpha\alpha'} = \begin{bmatrix} \left[\mathbf{G}_{j,j'}^{\alpha\alpha'}\right]_{0,0}^{0,0} & \left[\mathbf{G}_{j,j'}^{\alpha\alpha'}\right]_{0,1}^{0,-1} & \dots & \left[\mathbf{G}_{j,j'}^{\alpha\alpha'}\right]_{0,l'}^{0,m'} & \dots & \left[\mathbf{G}_{j,j'}^{\alpha\alpha'}\right]_{0,l_{\max}}^{0,l_{\max}} \\ \left[\mathbf{G}_{j,j'}^{\alpha\alpha'}\right]_{1,0}^{-1,0} & \left[\mathbf{G}_{j,j'}^{\alpha\alpha'}\right]_{1,1}^{-1,-1} & \dots & \dots & \dots & \left[\mathbf{G}_{j,j'}^{\alpha\alpha'}\right]_{1,l_{\max}}^{-1,l_{\max}} \\ \vdots & & \ddots & & & \vdots \\ \left[\mathbf{G}_{j,j'}^{\alpha\alpha'}\right]_{l,0}^{m,0} & \dots & & \left[\mathbf{G}_{j,j'}^{\alpha\alpha'}\right]_{l,l'}^{m,m'} & \dots & \left[\mathbf{G}_{j,j'}^{\alpha\alpha'}\right]_{l,l_{\max}}^{m,l_{\max}} \\ \vdots & & & & \ddots & \vdots \\ \left[\mathbf{G}_{j,j'}^{\alpha\alpha'}\right]_{l_{\max},0}^{l_{\max},0} & \dots & \dots & \dots & \dots & \left[\mathbf{G}_{j,j'}^{\alpha\alpha'}\right]_{l_{\max},l_{\max}}^{l_{\max},l_{\max}} \end{bmatrix}, \tag{C.6cc}$$

where

$$\left[\mathbf{G}_{j,j'}^{\alpha\alpha'}\right]_{l,l'}^{m,m'} = \langle \psi_{l,m}^{j} | \mathbf{G}_{\mathrm{B}}^{\alpha\alpha'} | \psi_{l',m'}^{j'} \rangle, \tag{C.6cd}$$

is a generic Green's tensor matrix element, see Eq. (C.4).

C.2 Field Outside Scatterers

As outlined in Section 3.4, the H-integrals (introduced in Eqs. (3.40)) can be computed as the B-integrals; In Fig. 3.5(b), we interchange the roles of $\mathbf{r}_j$ and $\mathbf{r}'_j$ and express the scalar Green's function analogously to Eq. (3.36)

$$g_{\mathrm{B}}(\mathbf{R}) = ik_{\mathrm{B}} \sum_{\nu,\mu} \{\tilde{\psi}_{\nu,\mu}^{j,\mathrm{B}}(\mathbf{r}'_j)\}^{Y^*} \varphi_{\nu,\mu}^{\mathrm{B}}(\mathbf{r}_j). \tag{C.7}$$

We then insert the elements of the Green's tensor by acting the differential operators on $\varphi_{\nu,\mu}^{\mathrm{B}}(\mathbf{r}_j)$ and the α'th component of the induced field on scatterer j, Eq. (3.13a), to find

$$\begin{aligned} H_j^{\alpha\alpha'}(\mathbf{r}) &= \sum_{l,m} e_{j\alpha' lm} \int_{V_j} \psi_{l,m}^{j}(\mathbf{r}'_j) \left\{ ik_{\mathrm{B}} \sum_{\nu,\mu} \{\tilde{\psi}_{\nu,\mu}^{j,\mathrm{B}}(\mathbf{r}'_j)\}^{Y^*} \left(\delta_{\alpha\,\alpha'} + \frac{1}{k_{\mathrm{B}}^2} \partial_\alpha \partial_{\alpha'}\right) \varphi_{\nu,\mu}^{\mathrm{B}}(\mathbf{r}_j) \right\} \mathrm{d}\mathbf{r}'_j \\ &= ik_{\mathrm{B}} \sum_{l,m} e_{j\alpha' lm} M_l^j \Big/ \left(N_l^{j,\mathrm{B}}\right) \left(\delta_{\alpha\,\alpha'} + \frac{1}{k_{\mathrm{B}}^2} \partial_\alpha \partial_{\alpha'}\right) \varphi_{l,m}^{\mathrm{B}}(\mathbf{r}_j). \end{aligned} \tag{C.8}$$

We finally obtain the explicit expressions for all permutations of α and α' by using the results from Appendix A.5

$$\begin{aligned} H_j^{xx}(\mathbf{r}) = ik_\mathrm{B} \sum_{l,m} e_{jxlm} M_l^j \Big/ \left(N_l^{j,\mathrm{B}}\right) \Big\{ & \varphi_{l,m}^\mathrm{B}(\mathbf{r}_j) + \frac{1}{4} \Big[g_{++}^{+2,+2}(l,m) \varphi_{l+2,m+2}^\mathrm{B}(\mathbf{r}_j) \\ & + g_{++}^{0,+2}(l,m) \varphi_{l,m+2}^\mathrm{B}(\mathbf{r}_j) + g_{++}^{-2,+2}(l,m) \varphi_{l-2,m+2}^\mathrm{B}(\mathbf{r}_j) + g_{--}^{+2,-2}(l,m) \varphi_{l+2,m-2}^\mathrm{B}(\mathbf{r}_j) \\ & + g_{--}^{0,-2}(l,m) \varphi_{l,m-2}^\mathrm{B}(\mathbf{r}_j) + g_{--}^{-2,-2}(l,m) \varphi_{l-2,m-2}^\mathrm{B}(\mathbf{r}_j) + 2 \Big(g_{-+}^{+2,0}(l,m) \varphi_{l+2,m}^\mathrm{B}(\mathbf{r}_j) \\ & + \; g_{-+}^{0,0}(l,m) \varphi_{l,m}^\mathrm{B}(\mathbf{r}_j) + g_{-+}^{-2,0}(l,m) \varphi_{l-2,m}^\mathrm{B}(\mathbf{r}_j) \Big) \Big] \Big\}, \end{aligned} \tag{C.9a}$$

$$\begin{aligned} H_j^{xy}(\mathbf{r}) = ik_\mathrm{B} \sum_{l,m} e_{jylm} M_l^j \Big/ \left(N_l^{j,\mathrm{B}}\right) \frac{1}{4i} \Big\{ & g_{++}^{+2,+2}(l,m) \varphi_{l+2,m+2}^\mathrm{B}(\mathbf{r}_j) \\ & + g_{++}^{0,+2}(l,m) \varphi_{l,m+2}^\mathrm{B}(\mathbf{r}_j) + g_{++}^{-2,+2}(l,m) \varphi_{l-2,m+2}^\mathrm{B}(\mathbf{r}_j) - \Big[g_{--}^{+2,-2}(l,m) \varphi_{l+2,m-2}^\mathrm{B}(\mathbf{r}_j) \\ & + g_{--}^{0,-2}(l,m) \varphi_{l,m-2}^\mathrm{B}(\mathbf{r}_j) + g_{--}^{-2,-2}(l,m) \varphi_{l-2,m-2}^\mathrm{B}(\mathbf{r}_j) \Big] \Big\}, \end{aligned} \tag{C.9b}$$

$$\begin{aligned} H_j^{xz}(\mathbf{r}) = ik_\mathrm{B} \sum_{l,m} e_{jzlm} M_l^j \Big/ \left(N_l^{j,\mathrm{B}}\right) \frac{1}{2} \Big\{ & g_{0+}^{+2,+1}(l,m) \varphi_{l+2,m+1}^\mathrm{B}(\mathbf{r}_j) \\ & + g_{0+}^{0,+1}(l,m) \varphi_{l,m+1}^\mathrm{B}(\mathbf{r}_j) + g_{0+}^{-2,+1}(l,m) \varphi_{l-2,m+1}^\mathrm{B}(\mathbf{r}_j) + g_{-0}^{+2,-1}(l,m) \varphi_{l+2,m-1}^\mathrm{B}(\mathbf{r}_j) \\ & + g_{-0}^{0,-1}(l,m) \varphi_{l,m-1}^\mathrm{B}(\mathbf{r}_j) + g_{-0}^{-2,-1}(l,m) \varphi_{l-2,m-1}^\mathrm{B}(\mathbf{r}_j) \Big\}, \end{aligned} \tag{C.9c}$$

$$H_j^{yx}(\mathbf{r}) = H_j^{xy}(\mathbf{r}) \left(e_{jylm} \to e_{jxlm}\right), \tag{C.9d}$$

$$\begin{aligned} H_j^{yy}(\mathbf{r}) = ik_\mathrm{B} \sum_{l,m} e_{jylm} M_l^j \Big/ \left(N_l^{j,\mathrm{B}}\right) \Big\{ & \varphi_{l,m}^\mathrm{B}(\mathbf{r}_j) - \frac{1}{4} \Big[g_{++}^{+2,+2}(l,m) \varphi_{l+2,m+2}^\mathrm{B}(\mathbf{r}_j) \\ & + g_{++}^{0,+2}(l,m) \varphi_{l,m+2}^\mathrm{B}(\mathbf{r}_j) + g_{++}^{-2,+2}(l,m) \varphi_{l-2,m+2}^\mathrm{B}(\mathbf{r}_j) + g_{--}^{+2,-2}(l,m) \varphi_{l+2,m-2}^\mathrm{B}(\mathbf{r}_j) \\ & + g_{--}^{0,-2}(l,m) \varphi_{l,m-2}^\mathrm{B}(\mathbf{r}_j) + g_{--}^{-2,-2}(l,m) \varphi_{l-2,m-2}^\mathrm{B}(\mathbf{r}_j) - 2 \Big(g_{-+}^{+2,0}(l,m) \varphi_{l+2,m}^\mathrm{B}(\mathbf{r}_j) \\ & + \; g_{-+}^{0,0}(l,m) \varphi_{l,m}^\mathrm{B}(\mathbf{r}_j) + g_{-+}^{-2,0}(l,m) \varphi_{l-2,m}^\mathrm{B}(\mathbf{r}_j) \Big) \Big] \Big\}, \end{aligned} \tag{C.9e}$$

$$\begin{aligned} H_j^{yz}(\mathbf{r}) = ik_\mathrm{B} \sum_{l,m} e_{jzlm} M_l^j \Big/ \left(N_l^{j,\mathrm{B}}\right) \frac{1}{2i} \Big\{ & g_{0+}^{+2,+1}(l,m) \varphi_{l+2,m+1}^\mathrm{B}(\mathbf{r}_j) \\ & + g_{0+}^{0,+1}(l,m) \varphi_{l,m+1}^\mathrm{B}(\mathbf{r}_j) + g_{0+}^{-2,+1}(l,m) \varphi_{l-2,m+1}^\mathrm{B}(\mathbf{r}_j) - \Big[g_{-0}^{+2,-1}(l,m) \varphi_{l+2,m-1}^\mathrm{B}(\mathbf{r}_j) \Big] \\ & + g_{-0}^{0,-1}(l,m) \varphi_{l,m-1}^\mathrm{B}(\mathbf{r}_j) + g_{-0}^{-2,-1}(l,m) \varphi_{l-2,m-1}^\mathrm{B}(\mathbf{r}_j) \Big] \Big\}, \end{aligned} \tag{C.9f}$$

$$H_j^{zx}(\mathbf{r}) = H_j^{xz}(\mathbf{r}) \left(e_{jzlm} \to e_{jxlm}\right), \tag{C.9g}$$

$$H_j^{zy}(\mathbf{r}) = H_j^{yz}(\mathbf{r})\,(e_{jzlm} \to e_{jylm})\,, \tag{C.9h}$$

$$H_j^{zz}(\mathbf{r}) = ik_{\mathrm{B}} \sum_{l,m} e_{jzlm} M_l^j \,/\, \left(N_l^{j,\mathrm{B}}\right) \Big\{ \varphi_{l,m}^{\mathrm{B}}(\mathbf{r}_j) + g_{00}^{+2,0}(l,m)\varphi_{l+2,m}^{\mathrm{B}}(\mathbf{r}_j) + g_{00}^{0,0}(l,m)\varphi_{l,m}^{\mathrm{B}}(\mathbf{r}_j) + g_{00}^{-2,0}(l,m)\varphi_{l-2,m}^{\mathrm{B}}(\mathbf{r}_j) \Big\}. \tag{C.9i}$$

C.3 Scattering Cross Section

In this section, we modify the calculation of the scattering cross section from Section 3.6.

In the view of the asymptotic expansion in Eq. (3.52), and to be able to express the scattering amplitude compactly, we define the following function

$$\Phi_{l,m}^j(\mathbf{r}_j) \equiv \frac{(-i)^{l+1}}{k_{\mathrm{B}}} Y_l^m(\theta_{G-j}, \phi_{G-j}), \tag{C.10}$$

where θ_{G-j} and ϕ_{G-j} are the polar and azimuthal angles of the vector $\mathbf{r}_j = \mathbf{r} - \mathbf{r}_j^0$, respectively. Using this function, the scattering amplitude is given in Eq. (3.53).

As discussed in Section 3.6, the contributions to $\mathbf{f}(\theta, \phi)$ from the different scatterers are defined in the local coordinates, and this representation renders the solid angle integration in Eq. (2.31) infeasible; The contributions must be defined with respect to the same Origo. The translation from one Origo to another can be carried out using the separation matrices of Appendix B.1. Most elegantly, we would translate the contributions from all N scatterers to the global Origo, $\mathcal{O}$ (see Fig. 3.1), but since, as discussed in Section 4.4, these matrices are time-consuming to compute, we prefer to minimize the use of these. We therefore proceed as discussed in Ref. [54] and translate the basis function of the scatterers $j = 2, 3, \ldots, N$ to the coordinate system of the scatterer $j = 1$. Subsequently, we perform the solid angle integration with respect to $\mathcal{O}_1$. We in this way reduce the number of separation matrices by one, as compared to translating all the basis functions to $\mathcal{O}$, and for small systems, $N \gtrsim 1$, this substantially decreases the computation time.

We start from the expressions for $H_j^{\alpha\alpha'}(\mathbf{r})$ from Appendix C.2. These, as discussed in Section 3.6, contain sums over terms that are all proportional to one of the spherical outgoing wavefunctions, $\varphi_{l,m}^{\mathrm{B}}(\mathbf{r}_j)$, and for $j \neq 1$ we wish to translate these to $\mathcal{O}_1$.

To that end, we consider the sketch in Fig. C.1 where an arbitrary scatterer $j \neq 1$ and the scatterer $j = 1$ are shown in 2D. An arbitrary point, with coordinates $\mathbf{r}_j$ (red vector) and $\mathbf{r}_1$ (blue vector) with respect to $\mathcal{O}_j$ and $\mathcal{O}_1$, respectively, is shown, and the dashed parts of these signify that the point is far away from the scatterers. The displacement vector between $\mathcal{O}_1$ and $\mathcal{O}_j$, $\mathbf{b}_{1,j}$ is shown, and in the following we employ $\mathbf{b} \equiv \mathbf{b}_{1,j}$.

From the sketch, it is apparent that the sum of the two blue vectors equals the red vector

$$\mathbf{r}_j = \mathbf{b} + \mathbf{r}_1, \tag{C.11}$$

with $\mathbf{b} < \mathbf{r}_1$, and using this we expand $\varphi_{l,m}^{\mathrm{B}}(\mathbf{r}_j)$ around $\mathcal{O}_1$ [34, Chap. 3]

$$\varphi_{l,m}^{\mathrm{B}}(\mathbf{r}_j) = \sum_{\nu,\mu} \hat{S}_{l,\nu}^{m,\mu}(\mathbf{b}) \varphi_{\nu,\mu}^{\mathrm{B}}(\mathbf{r}_1). \tag{C.12}$$

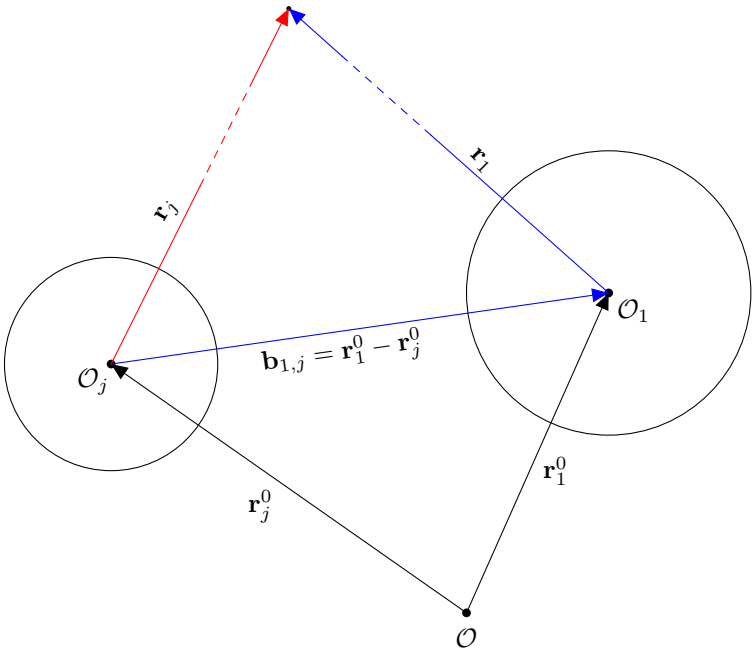

Figure C.1 Two scatterers, $j \neq 1$ and $j = 1$, sketched in 2D. The centers of the scatterers, $\mathbf{r}_j^0$ and $\mathbf{r}_1^0$, and an arbitrary point outside the scatterers, $\mathbf{r}_j$ (red vector) and $\mathbf{r}_1$ (blue vector) with respect to $\mathcal{O}_j$ and $\mathcal{O}_1$, respectively, is shown. The dashed parts of these vectors signify that the point is far away from the scatterers. Likewise, the displacement vector between the centers of the scatterers, $\mathbf{b}_{1,j}$, is shown.

Combining this with the results from Eqs. (3.52) and (C.10), we have

$$\varphi^{\mathrm{B}}_{l,m}(\mathbf{r}_j) = \sum_{\nu,\mu} \hat{S}^{m,\mu}_{l,\nu}(\mathbf{b}) \Phi^1_{\nu,\mu}(\mathbf{r}_1) \exp(-i\mathbf{k}_{\mathrm{B}} \cdot \mathbf{r}_1^0) \frac{\exp(ik_{\mathrm{B}} r)}{r}. \tag{C.13}$$

We have thus expressed the outgoing spherical wavefunctions of the scatterers $j \neq 1$ with respect to the Origin of the scatterer $j = 1$. We can then present the following auxiliary definition of the components of the scattering amplitude, which supplements the definition in Eq. (3.53) and must be applied when computing the scattering cross section explicitly

$$\begin{aligned} \mathbf{f}^{\alpha}(\theta,\phi) =& k_0^2 \exp(-i\mathbf{k}_{\mathrm{B}} \cdot \mathbf{r}_j^0) \sum_{\alpha'} \Bigg\{ \Delta\epsilon_1 H_1^{\alpha\alpha'}(\mathbf{r}) \left(\varphi^{\mathrm{B}}_{l,m}(\mathbf{r}_1) \to \Phi^1_{l,m}(\mathbf{r}_1) \right) \\ &+ \sum_{j=2}^{N} \Delta\epsilon_j H_j^{\alpha\alpha'}(\mathbf{r}) \Big(\varphi^{\mathrm{B}}_{l,m}(\mathbf{r}_j) \to \sum_{\nu,\mu} \hat{S}^{m,\mu}_{l,\nu}(\mathbf{b}_{1,j}) \Phi^1_{\nu,\mu}(\mathbf{r}_1) \Big) \Bigg\}. \end{aligned} \tag{C.14}$$

This definition is complicated by the presence of the separation matrices, $\hat{S}^{m,\mu}_{l,\nu}(\mathbf{b}_{1,j})$, and we only use the above expression in a few cases to verify that indeed $C_{\mathrm{ext}} = C_{\mathrm{scat}} + C_{\mathrm{abs}}$.

C.4 Dipole Approximation: Green's Tensor Integrals

In this section, we express the integrals over the elements of the Green's tensor used in the dipole approximation, see Eq. (3.55b). As for the elements of the Green's tensor

matrix, see Section 3.3, we must treat the $j \neq j'$- and $j = j'$-cases separately. We start with the latter case.

We have $\mathbf{r}_j = \mathbf{0}$ (it is evaluated at the center of the jth scatterer, in the local coordinates), and when $j = j'$ this implies that $\mathbf{R}' = \mathbf{r}'_j - \mathbf{r}_j = \mathbf{r}'_j$. Consequently, the elements of the Green's tensor may be expressed as in Eq. (3.33), and since the solid angle integrations over the normalized spherical harmonics vanish unless $l = m = 0$ (see Eq. (A.5)), we have

$$\mathbf{G}_{jj}^{\mathrm{D},\alpha\alpha'} = \frac{ik_\mathrm{B}}{\sqrt{4\pi}} \left(\delta_{\alpha\,\alpha'} + \frac{1}{k_\mathrm{B}^2} \sum_{\gamma_{\alpha,\alpha'}} g_{\gamma_{\alpha,\alpha'}} \delta_{0\,\gamma'_{\alpha,\alpha'}} \delta_{0\,\gamma''_{\alpha,\alpha'}} \right) \sqrt{4\pi} \int_0^{R_j} h_0^{(1)}(k_\mathrm{B} r'_j) r'^2_j \, \mathrm{d}r'_j. \tag{C.15}$$

Writing $h_0^{(1)}(k_\mathrm{B} r'_j) = -i \exp(ik_\mathrm{B} r'_j)/(k_\mathrm{B} r'_j)$, the remaining integral becomes

$$\int_0^{R_j} h_0^{(1)}(k_\mathrm{B} r'_j) r'^2_j \, \mathrm{d}r'_j = -\frac{i}{k_\mathrm{B}} \int_0^{R_j} \exp(ik_\mathrm{B} r'_j) r'_j \, \mathrm{d}r'_j = \frac{-i}{k_\mathrm{B}^3} \Big[(1 - ik_\mathrm{B} R_j) \exp(ik_\mathrm{B} R_j) - 1 \Big]. \tag{C.16}$$

Inspection of the Cartesian derivatives in Appendix A.5 shows that the sum term in Eq. (C.15) vanishes unless $\alpha = \alpha'$, and we thus have

$$\mathbf{G}_{jj}^{\mathrm{D},\alpha\alpha'} = \delta_{\alpha\,\alpha'} \frac{2}{3k_\mathrm{B}^2} \Big[(1 - ik_\mathrm{B} R_j) \exp(ik_\mathrm{B} R_j) - 1 \Big], \tag{C.17}$$

where we have used that $1 + 1/2 g_{-+}^{0,0}(0,0) = 1 + g_{00}^{0,0}(0,0) = 2/3$. This result is consistent with a similar expression in [28].

We next proceed to the elements with $j \neq j'$ and employ the form of the Green's tensor in Eq. (3.26). We, as in the previous case, set $\mathbf{r}_j = \mathbf{0}$ which in the (ν, μ)-sum only retains the terms with basis functions with both indices equal to zero (due to Eq. (3.6); $\tilde{\psi}_{\nu,\mu}^{j,\mathrm{B}}(\mathbf{0}) = \delta_{\nu\,0}\delta_{\mu\,0}/\sqrt{4\pi}$)

$$\begin{aligned} \mathbf{G}_\mathrm{B}^{\alpha\alpha'}(\mathbf{r}_j^0, \mathbf{r}') = \frac{ik_\mathrm{B}}{\sqrt{4\pi}} \sum_{p,t} \{\tilde{\psi}_{p,t}^{j',\mathrm{B}}(\mathbf{r}'_{j'})\}^{Y^*} \\ \times \left(\delta_{\alpha\,\alpha'} S_{p,0}^{t,0}(\mathbf{b}) + \frac{1}{k_\mathrm{B}^2} \sum_{\gamma_{\alpha,\alpha'}} S_{p,-\gamma'_{\alpha,\alpha'}}^{t,-\gamma''_{\alpha,\alpha'}}(\mathbf{b}) g_{\gamma_{\alpha,\alpha'}} \right). \end{aligned} \tag{C.18}$$

We then perform the integration over $\mathbf{r}'_{j'}$ which only retains the $p = t = 0$-terms

$$\mathbf{G}_{jj'}^{\mathrm{D},\alpha\alpha'} = ik_\mathrm{B} Z_0^{j'} \left(\delta_{\alpha\,\alpha'} S_{0,0}^{0,0}(\mathbf{b}) + \frac{1}{k_\mathrm{B}^2} \sum_{\gamma_{\alpha,\alpha'}} S_{0,-\gamma'_{\alpha,\alpha'}}^{0,-\gamma''_{\alpha,\alpha'}}(\mathbf{b}) g_{\gamma_{\alpha,\alpha'}} \right), \tag{C.19}$$

where

$$\begin{aligned} Z_0^{j'} \equiv \int_0^{R_{j'}} j_0(k_\mathrm{B} r'_{j'}) r'^2_{j'} \, \mathrm{d}r'_{j'} &= \frac{1}{k_\mathrm{B}} \int_0^{R_{j'}} \sin(k_\mathrm{B} r'_{j'}) r'_{j'} \, \mathrm{d}r'_{j'} \\ &= \frac{1}{k_\mathrm{B}^3} \Big[\sin(k_\mathrm{B} R_{j'}) - k_\mathrm{B} R_{j'} \cos(k_\mathrm{B} R_{j'}) \Big]. \end{aligned} \tag{C.20}$$

Eqs. (C.17) and (C.19) give the elements of the Green's tensor matrix for determining the electric field inside N small scatterers.

APPENDIX D

Cross Section Spectra

This appendix contains most of the data that was presented in more condensed forms in Chapter 5. The material is organized as follows:

D.1 Dimer Spectra

D.1.1 Varying Gap, d, $R = 10$ nm

Longitudinal

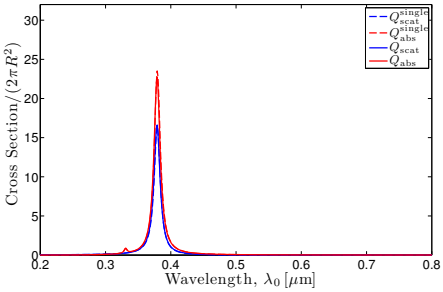

(a) $d/R = 15$.

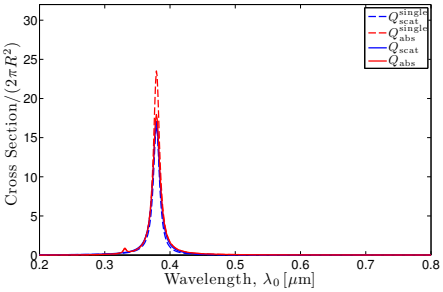

(b) $d/R = 10$.

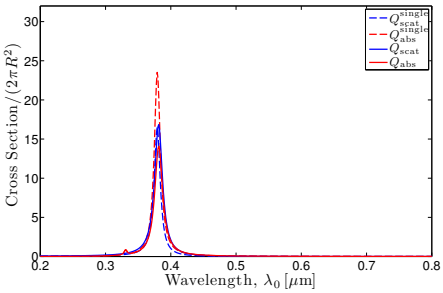

(c) $d/R = 5$.

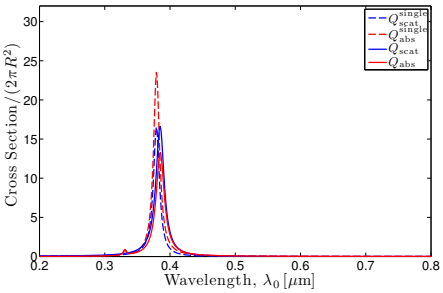

(d) $d/R = 3$.

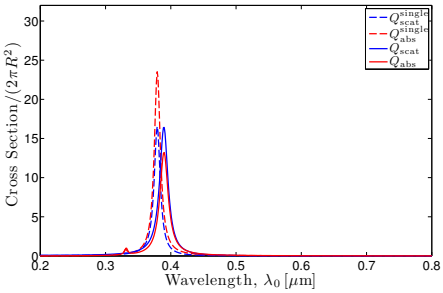

(e) $d/R = 2$.

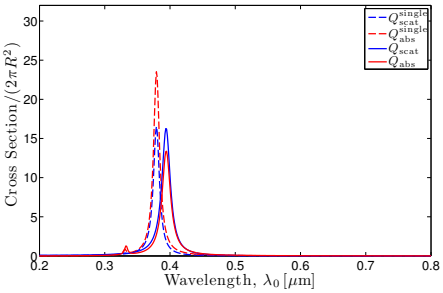

(f) $d/R = 1.5$.

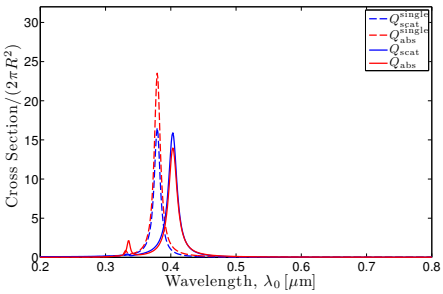

(g) $d/R = 1$.

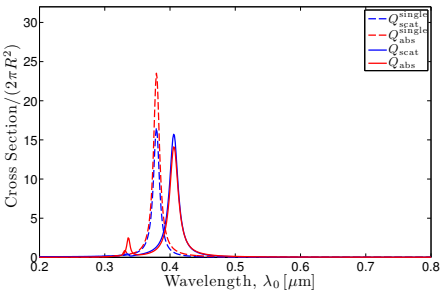

(h) $d/R = 0.9$.

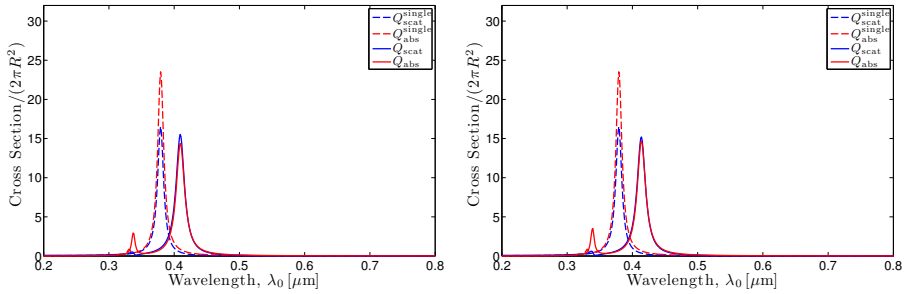

(i) $d/R = 0.8$.

(j) $d/R = 0.7$.

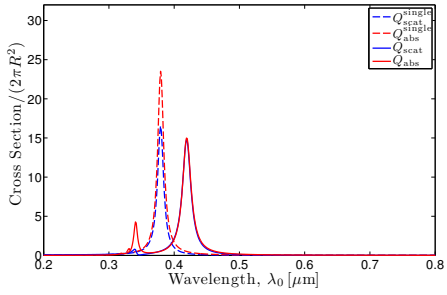

(k) $d/R = 0.6$.

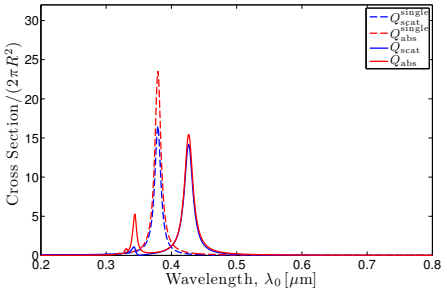

(l) $d/R = 0.5$.

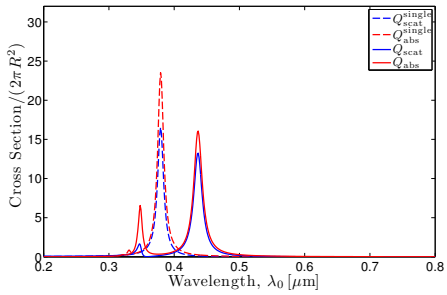

(m) $d/R = 0.4$.

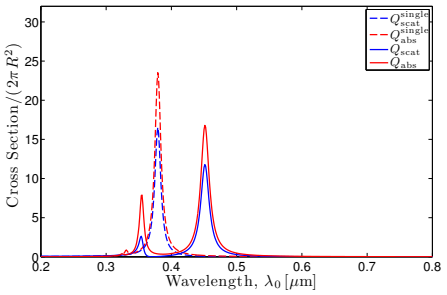

(n) $d/R = 0.3$.

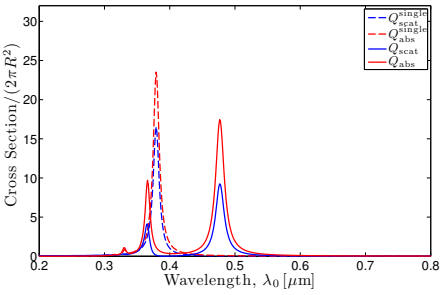

(o) $d/R = 0.2$.

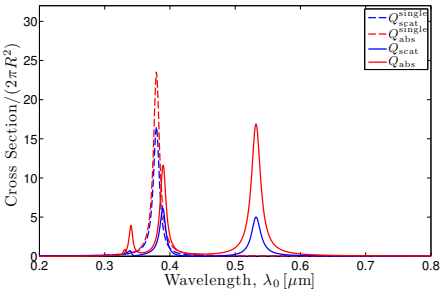

(p) $d/R = 0.1$.

Figure D.1 Longitudinal, see inset in Fig. 5.1(a).

Transverse

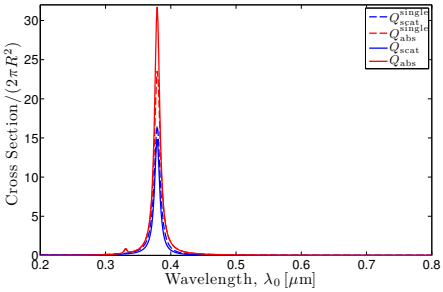

(a) $d/R = 15$.

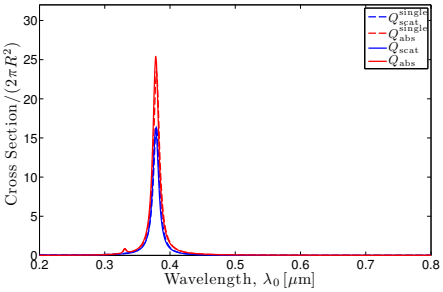

(b) $d/R = 10$.

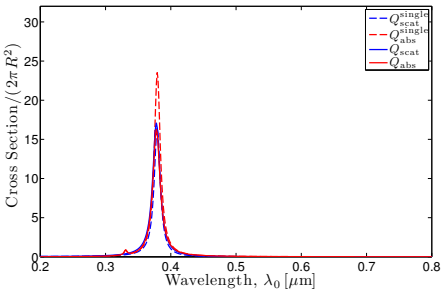

(c) $d/R = 5$.

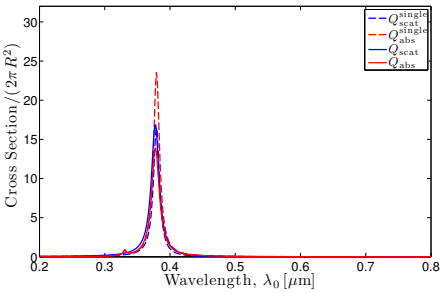

(d) $d/R = 3$.

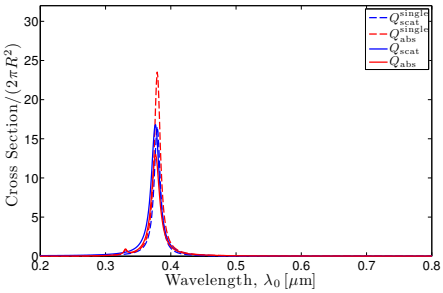

(e) $d/R = 2$.

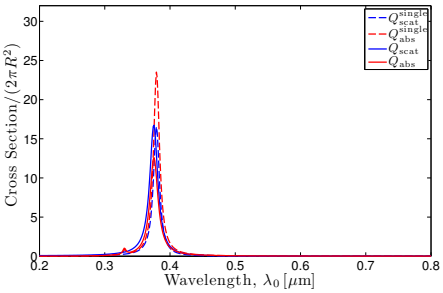

(f) $d/R = 1.5$.

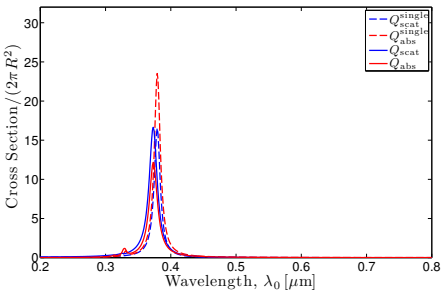

(g) $d/R = 1$.

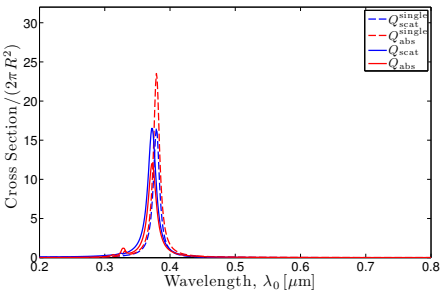

(h) $d/R = 0.9$.

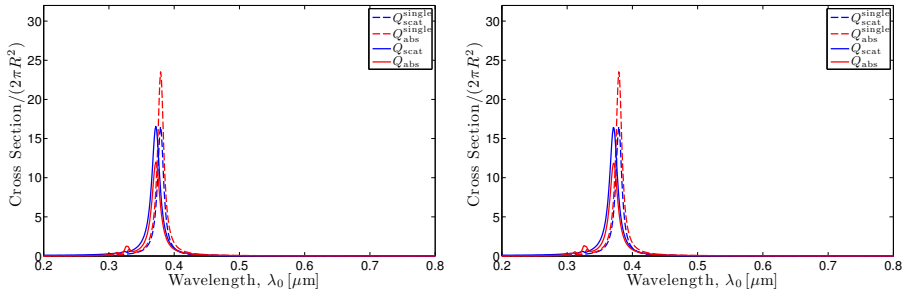

(i) $d/R = 0.8$.

(j) $d/R = 0.7$.

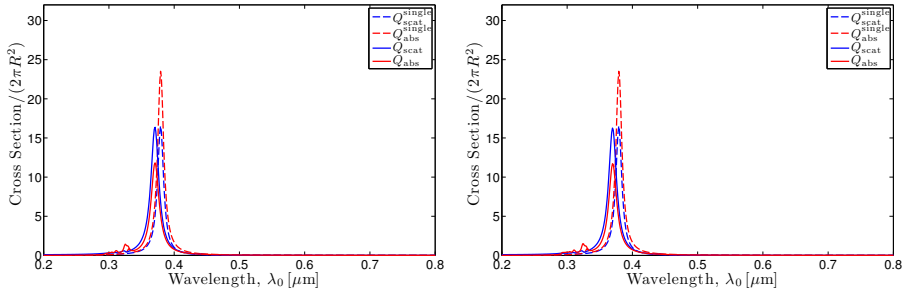

(k) $d/R = 0.6$.

(l) $d/R = 0.5$.

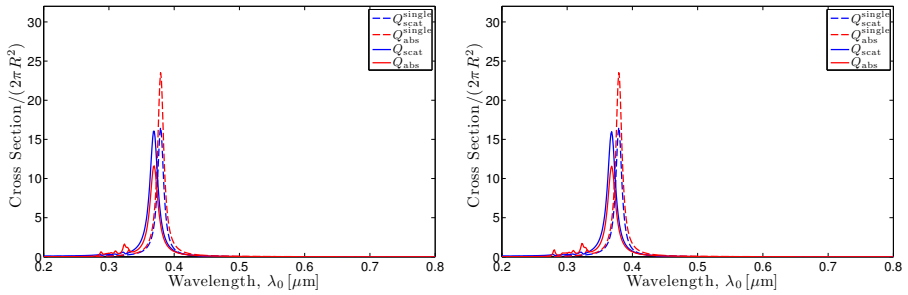

(m) $d/R = 0.4$.

(n) $d/R = 0.3$.

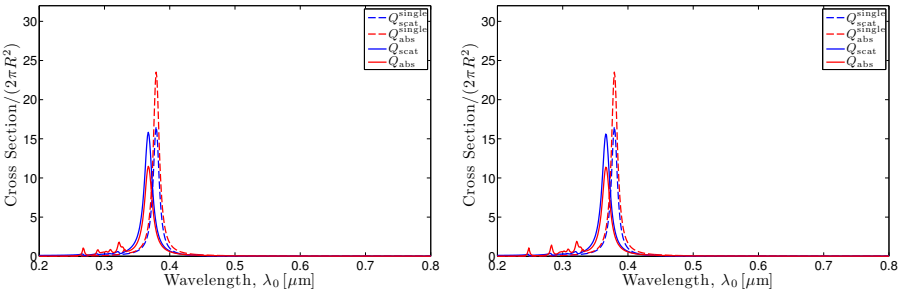

(o) $d/R = 0.2$.

(p) $d/R = 0.1$.

Figure D.2 Transverse, see inset in Fig. 5.1(b).

D.1.2 Varying Gap, d, $R = 25$ nm

Longitudinal

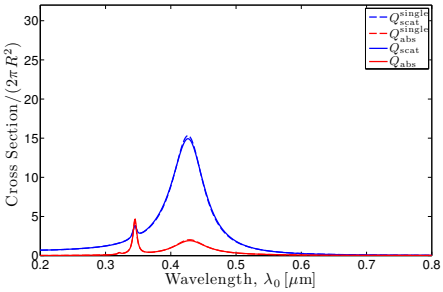

(a) $d/R = 15$.

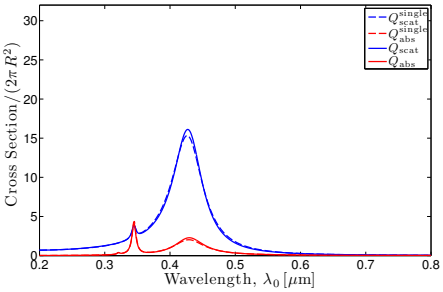

(b) $d/R = 10$.

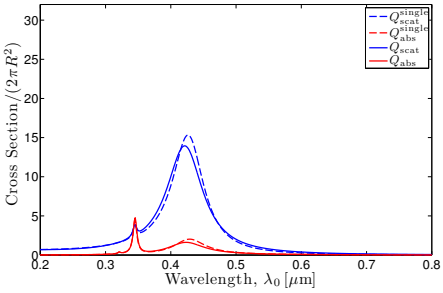

(c) $d/R = 5$.

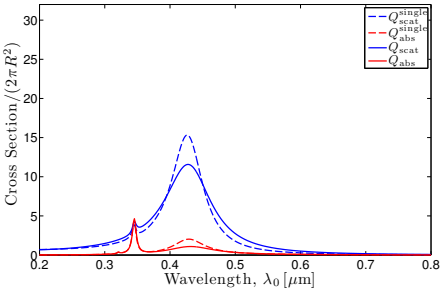

(d) $d/R = 3$.

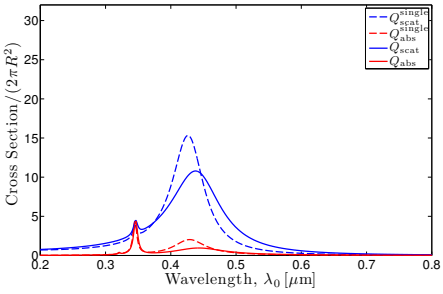

(e) $d/R = 2$.

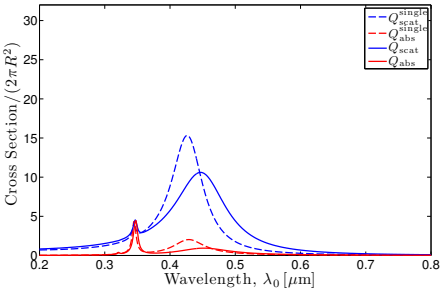

(f) $d/R = 1.5$.

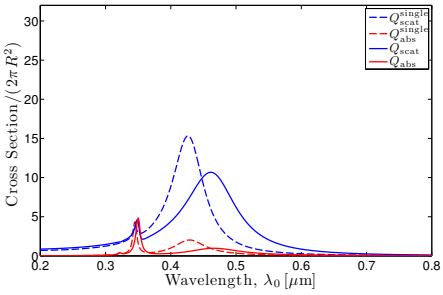

(g) $d/R = 1$.

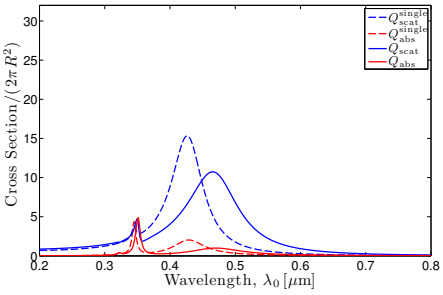

(h) $d/R = 0.9$.

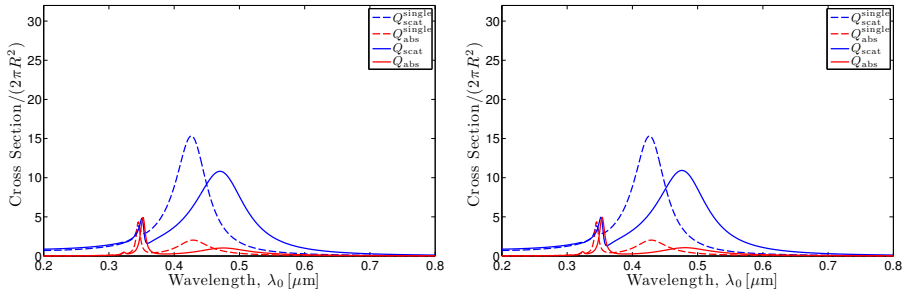

(i) $d/R = 0.8$.

(j) $d/R = 0.7$.

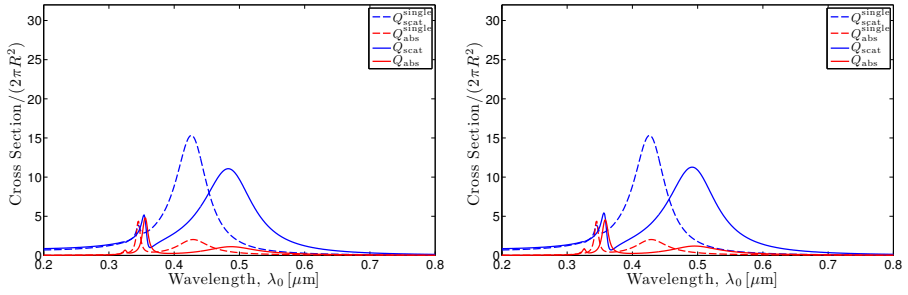

(k) $d/R = 0.6$.

(l) $d/R = 0.5$.

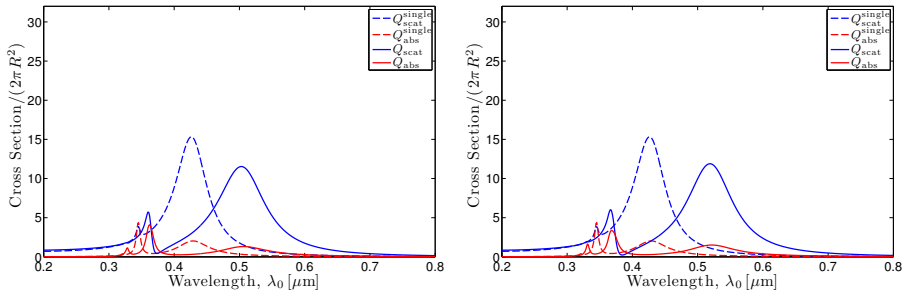

(m) $d/R = 0.4$.

(n) $d/R = 0.3$.

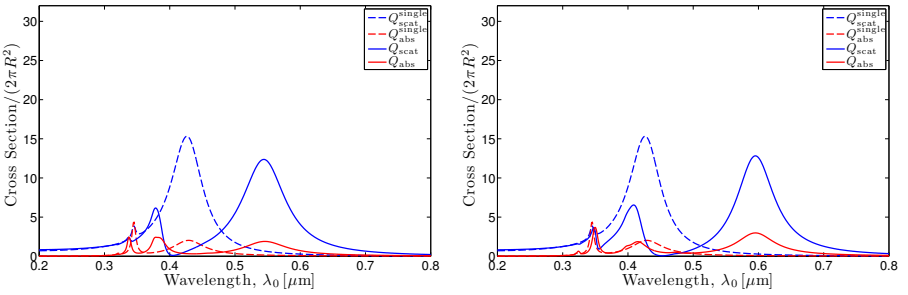

(o) $d/R = 0.2$.

(p) $d/R = 0.1$.

Figure D.3 Longitudinal, see inset in Fig. 5.4(a).

Transverse

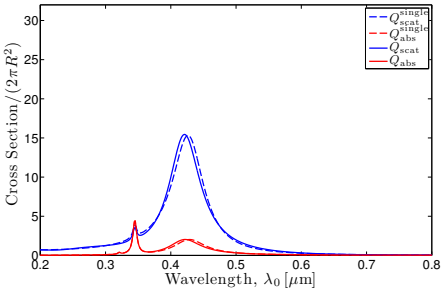

(a) $d/R = 15$.

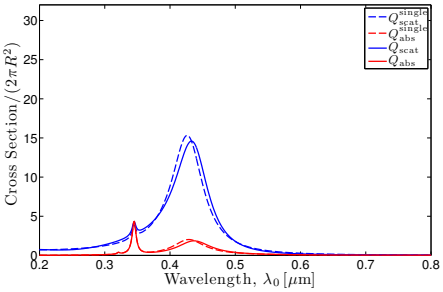

(b) $d/R = 10$.

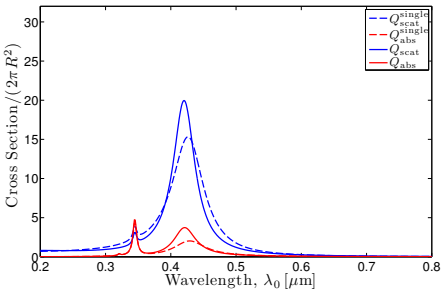

(c) $d/R = 5$.

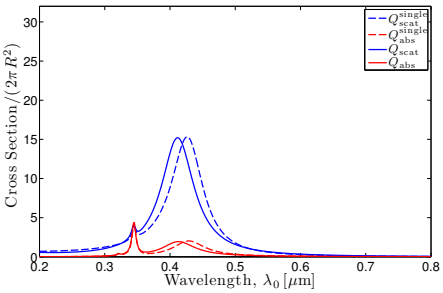

(d) $d/R = 3$.

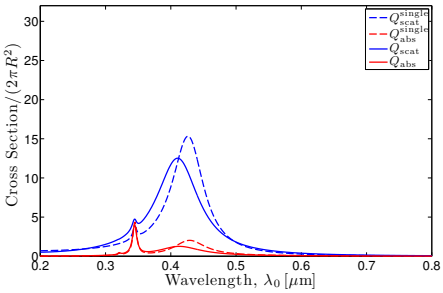

(e) $d/R = 2$.

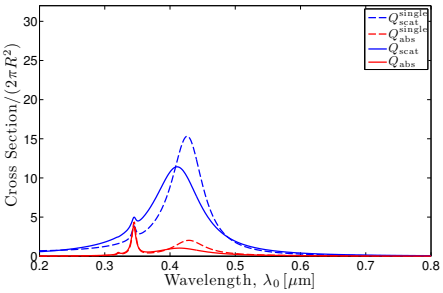

(f) $d/R = 1.5$.

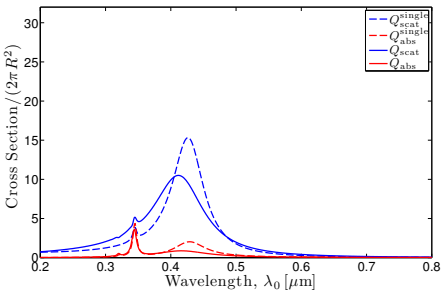

(g) $d/R = 1$.

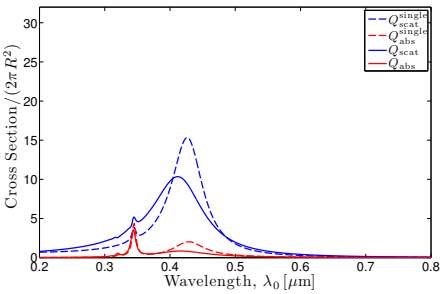

(h) $d/R = 0.9$.

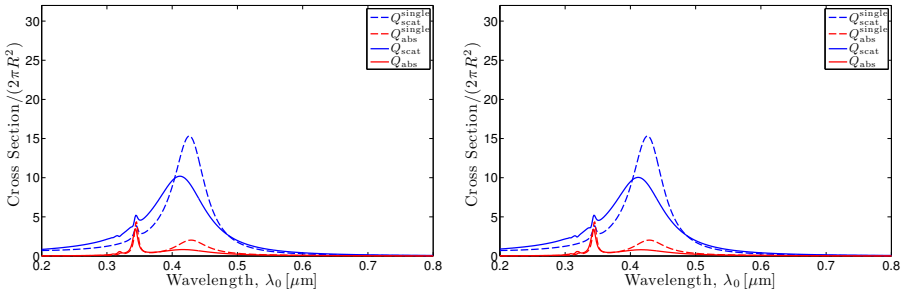

(i) $d/R = 0.8$.

(j) $d/R = 0.7$.

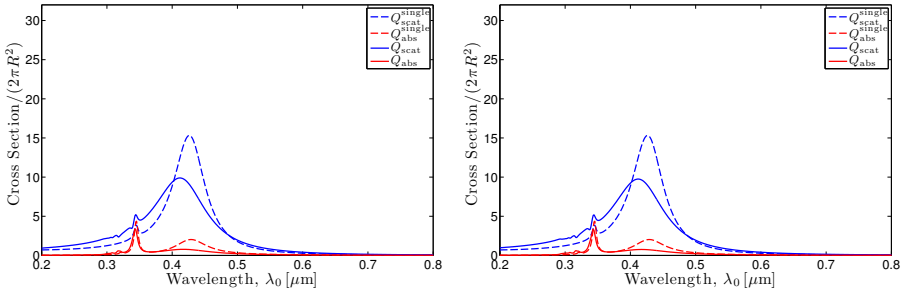

(k) $d/R = 0.6$.

(l) $d/R = 0.5$.

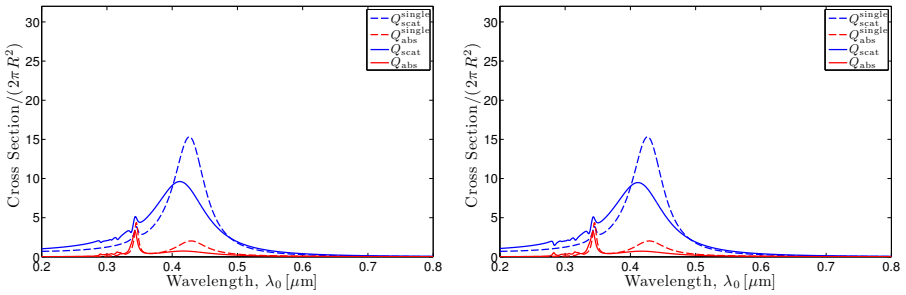

(m) $d/R = 0.4$.

(n) $d/R = 0.3$.

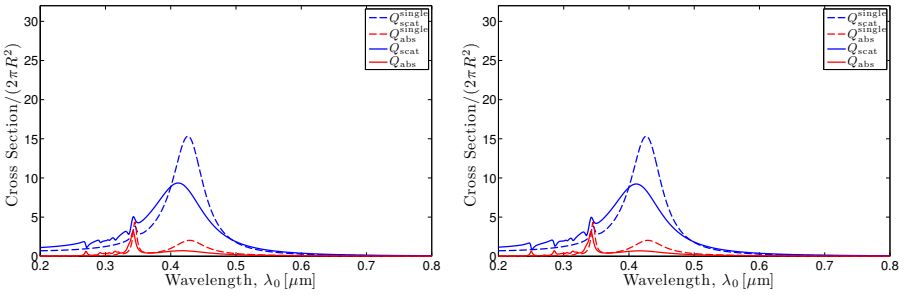

(o) $d/R = 0.2$.

(p) $d/R = 0.1$.

Figure D.4 Transverse, see inset in Fig. 5.4(b).

D.2 Chain Spectra

D.2.1 Varying Number of Scatterers, N , Fixed Gap, d, $R = 10$ nm

Longitudinal

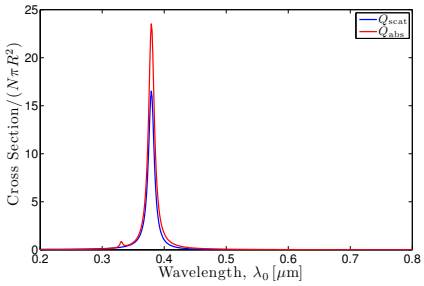

(a) $N = 1$.

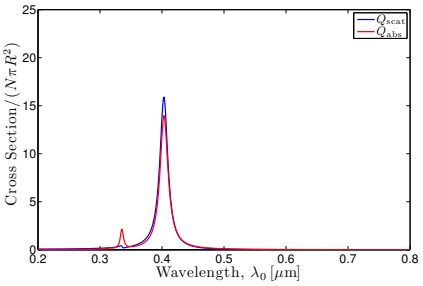

(b) $N = 2$.

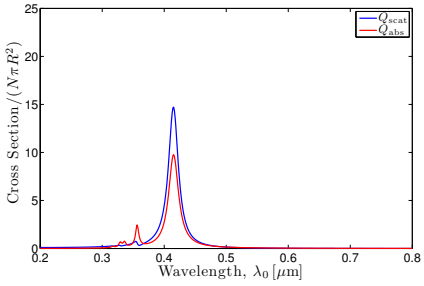

(c) $N = 3$.

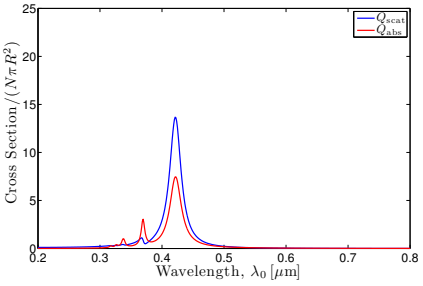

(d) $N = 4$.

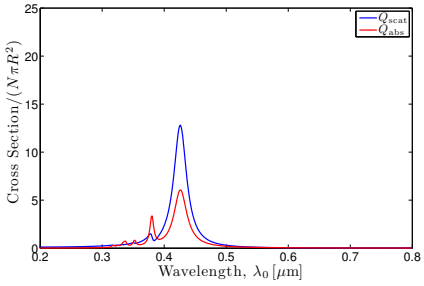

(e) $N = 5$.

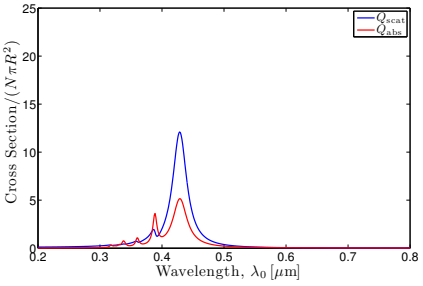

(f) $N = 6$.

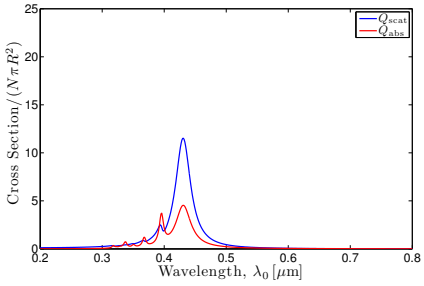

(g) $N = 7$.

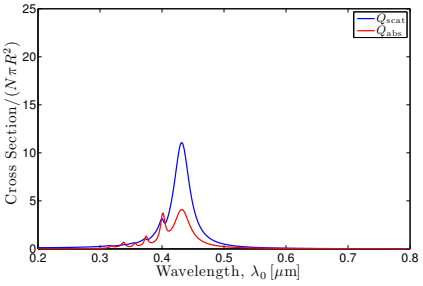

(h) $N = 8$.

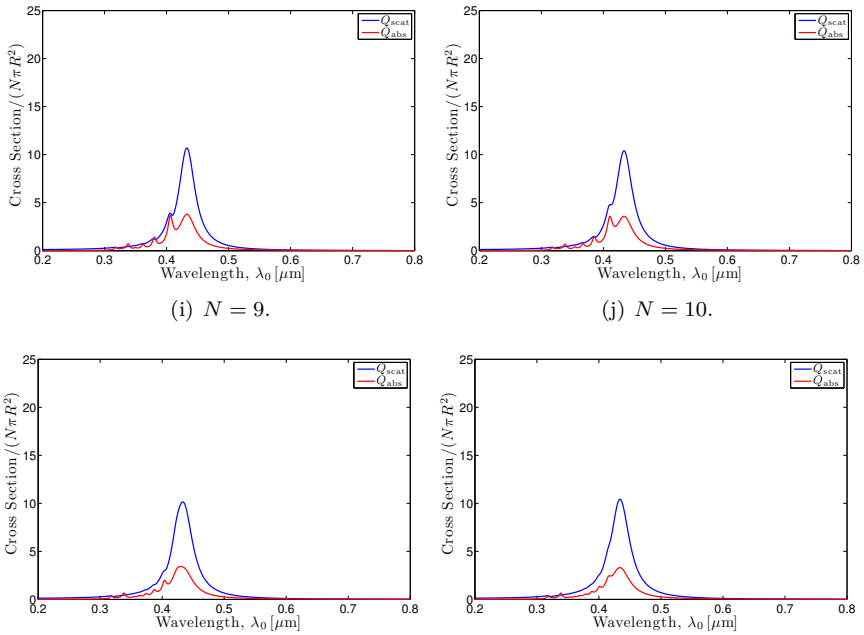

(i) $N = 9$. (j) $N = 10$.

(k) $N = 15$. (l) $N = 20$.

Figure D.5 Longitudinal, see inset in Fig. 5.6(a).

Transverse

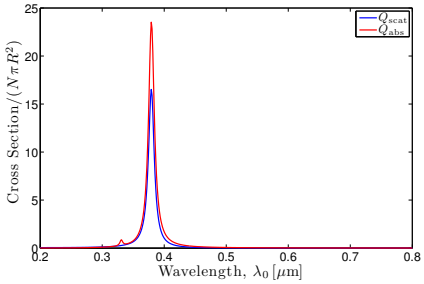

(a) $N = 1$.

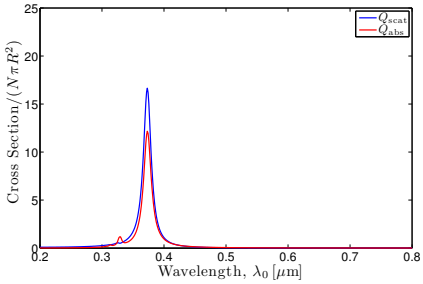

(b) $N = 2$.

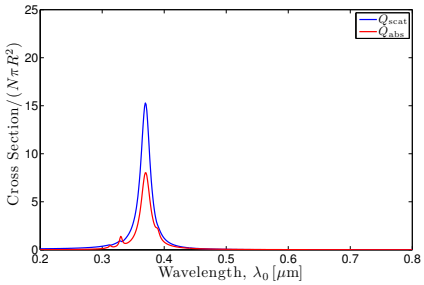

(c) $N = 3$.

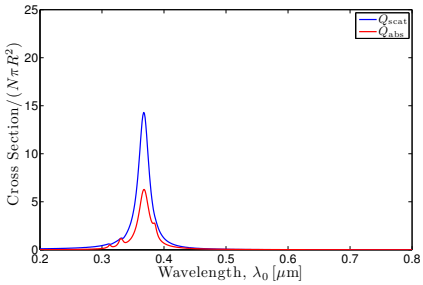

(d) $N = 4$.

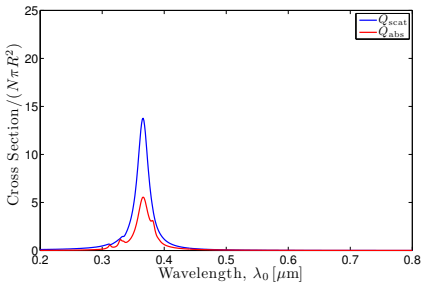

(e) $N = 5$.

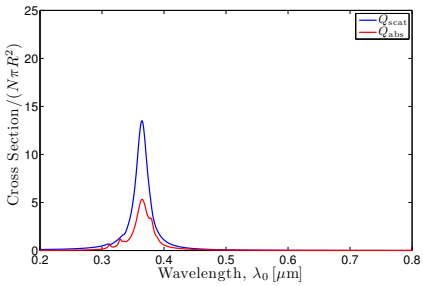

(f) $N = 6$.

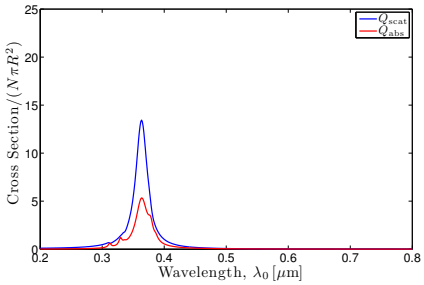

(g) $N = 7$.

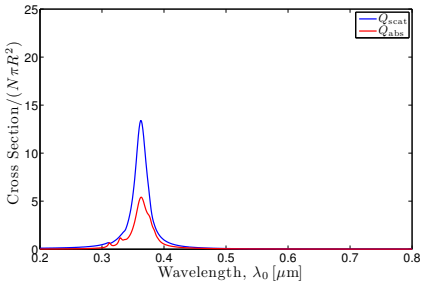

(h) $N = 8$.

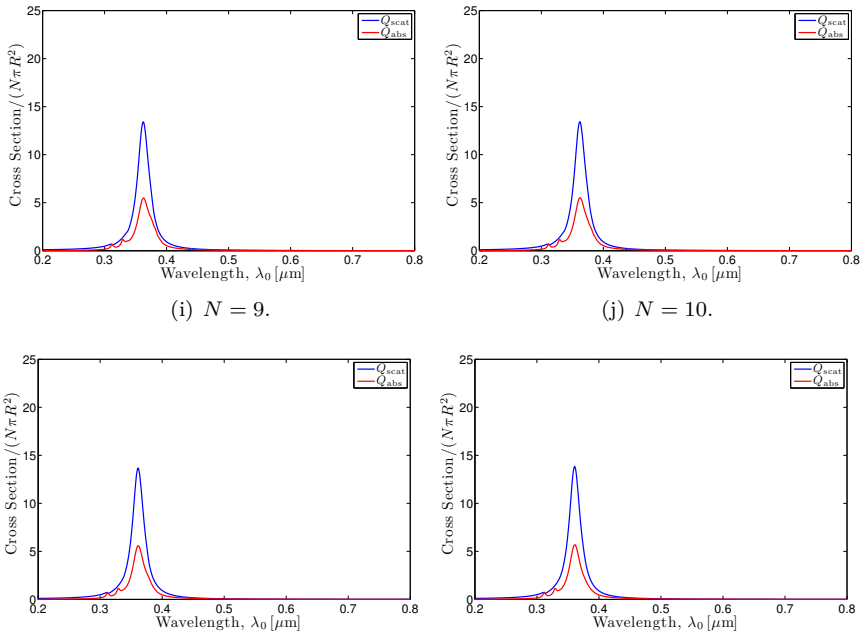

(i) $N = 9$. (j) $N = 10$.

(k) $N = 15$. (l) $N = 20$.

Figure D.6 Transverse, see inset in Fig. 5.6(b).

D.2.2 Varying Number of Scatterers, N , Fixed Gap, d, $R = 25$ nm

Longitudinal

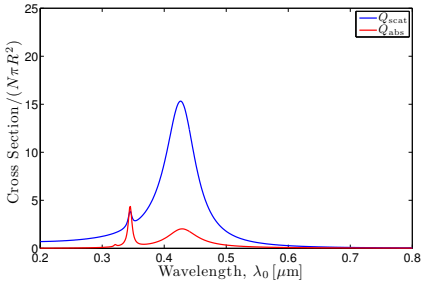

(a) $N = 1$.

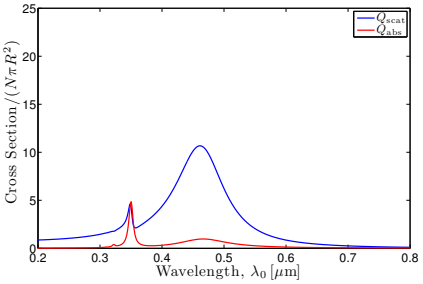

(b) $N = 2$.

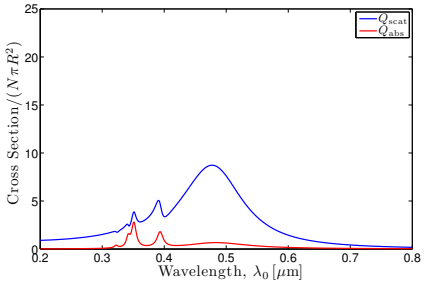

(c) $N = 3$.

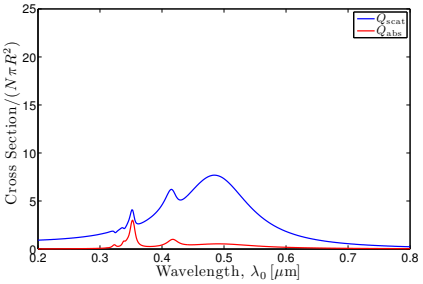

(d) $N = 4$.

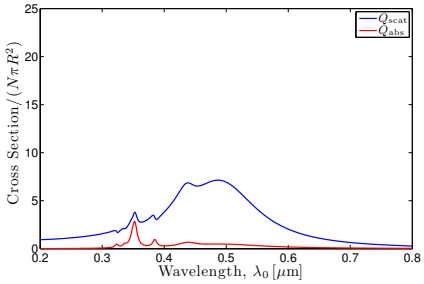

(e) $N = 5$.

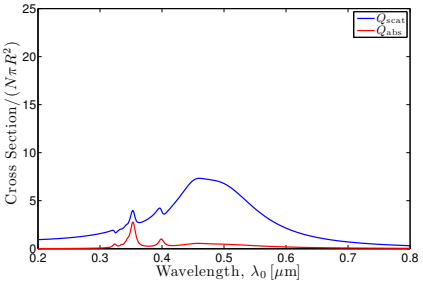

(f) $N = 6$.

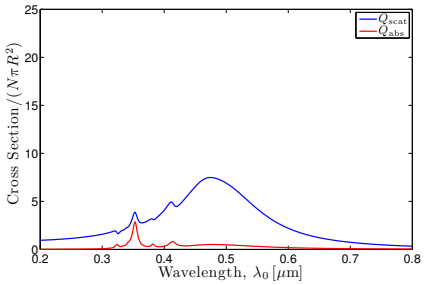

(g) $N = 7$.

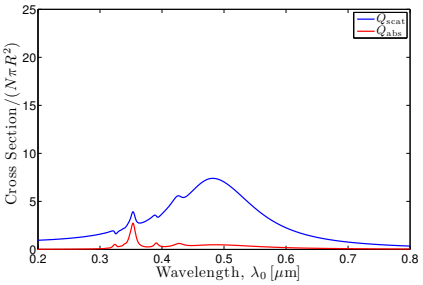

(h) $N = 8$.

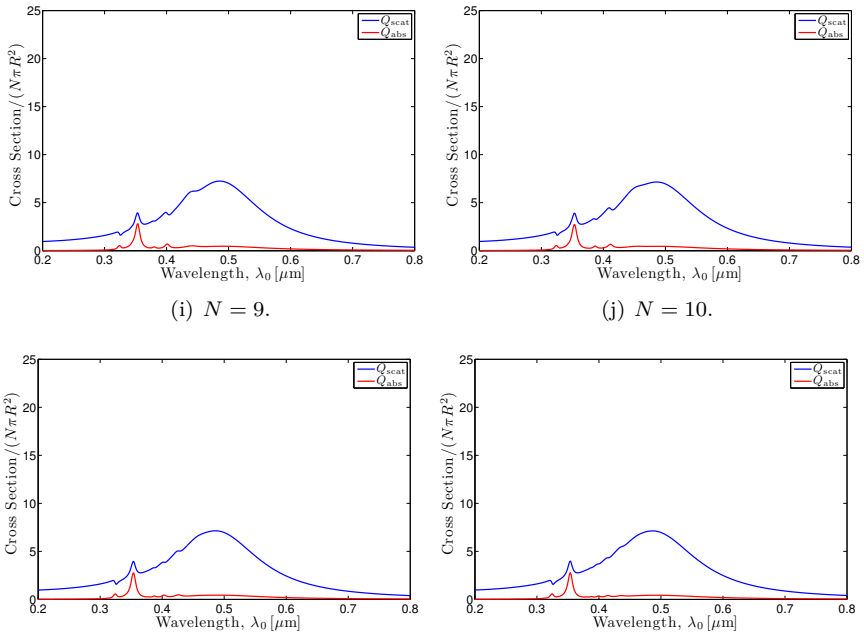

(i) $N = 9$. (j) $N = 10$.

(k) $N = 15$. (l) $N = 20$.

Figure D.7 Longitudinal, see inset in Fig. 5.6.

Transverse

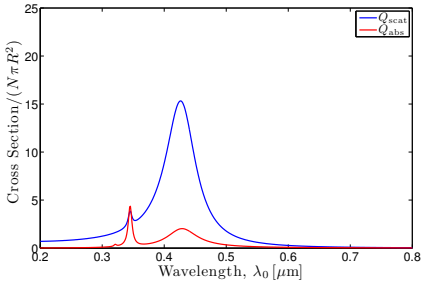

(a) $N = 1$.

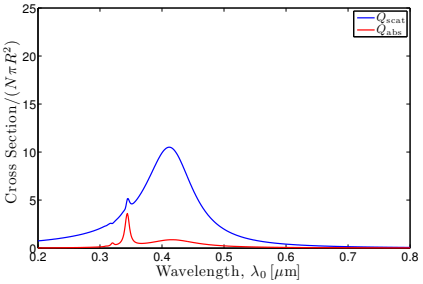

(b) $N = 2$.

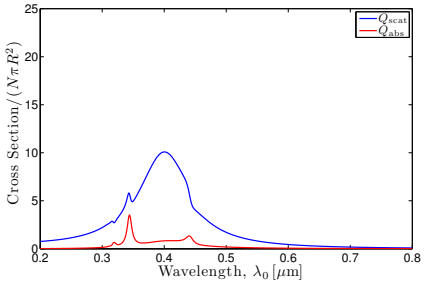

(c) $N = 3$.

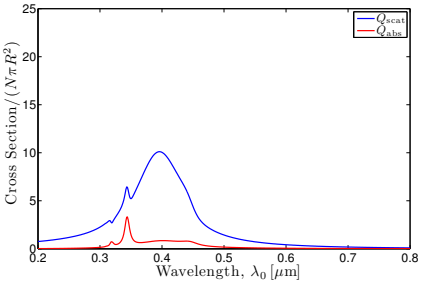

(d) $N = 4$.

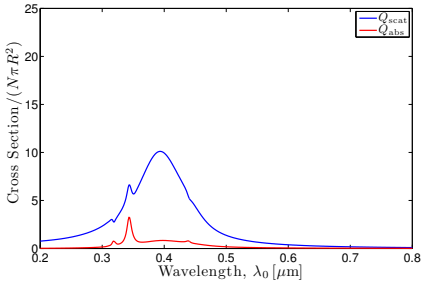

(e) $N = 5$.

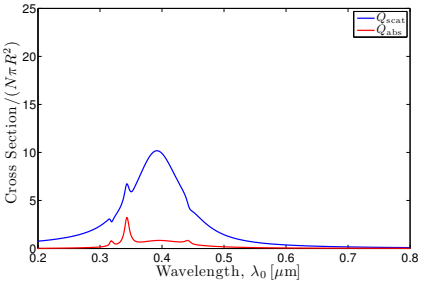

(f) $N = 6$.

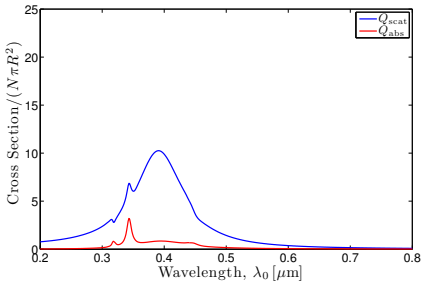

(g) $N = 7$.

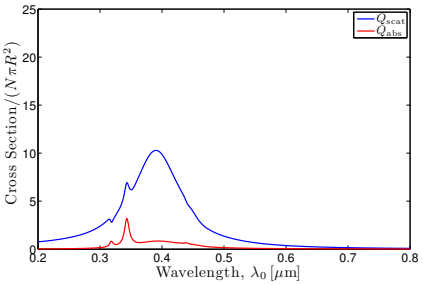

(h) $N = 8$.

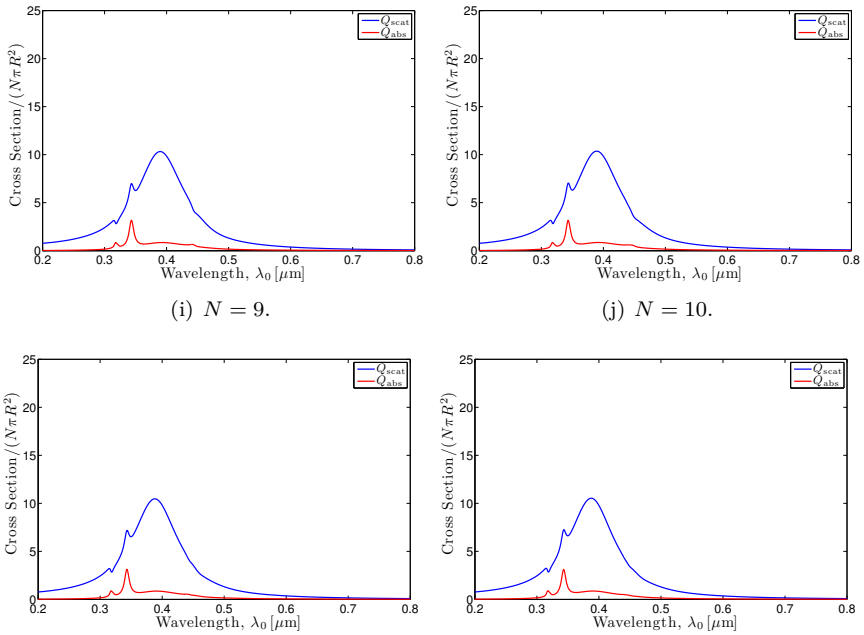

(i) $N = 9$. (j) $N = 10$.

(k) $N = 15$. (l) $N = 20$.

Figure D.8 Transverse, see the inset in Fig. 5.8.

D.3 Resonance Cross Sections

D.3.1 Dimer

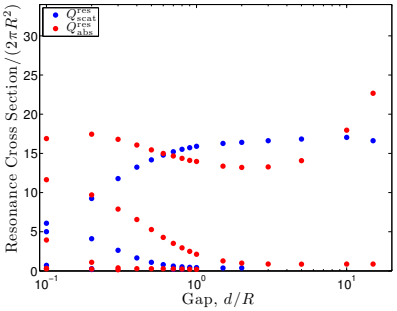

(a) $R = 10$ nm, Longitudinal, see inset in Fig. 5.1(a)

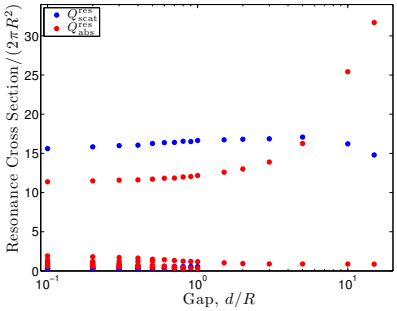

(b) $R = 10$ nm, Transverse, see inset in Fig. 5.1(b)

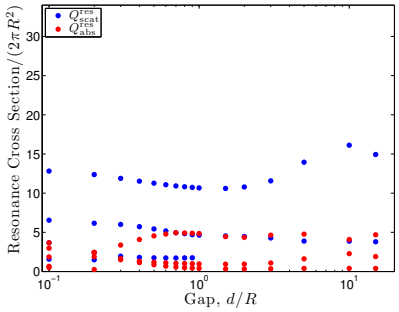

(c) $R = 25$ nm, Longitudinal, see inset in Fig. 5.4(a)

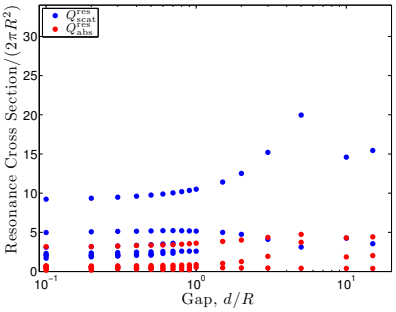

(d) $R = 25$ nm, Transverse, see inset in Fig. 5.4(b)

Figure D.9 Resonance cross sections from the spectra with $N = 2$ scatterers and varying gap, d, between the two scatterers; The spectra are presented in Appendices D.1.1 and D.1.2.

D.3.2 Chain

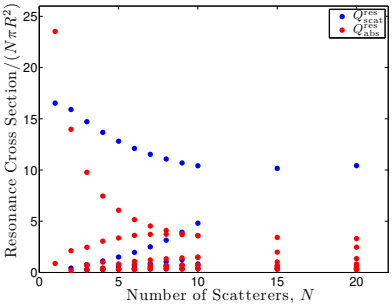

(a) $R = 10$ nm, Longitudinal, see inset in Fig. 5.6(a)

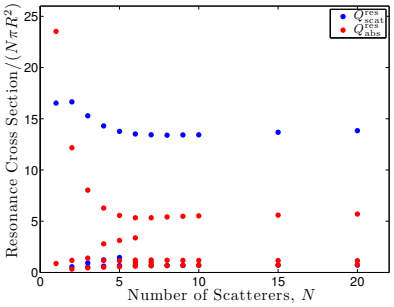

(b) $R = 10$ nm, Transverse, see inset in Fig. 5.6(b)

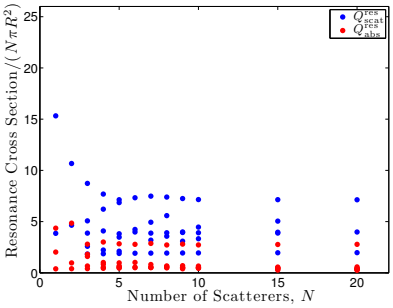

(c) $R = 25$ nm, Longitudinal, see inset in Fig. 5.8(a)

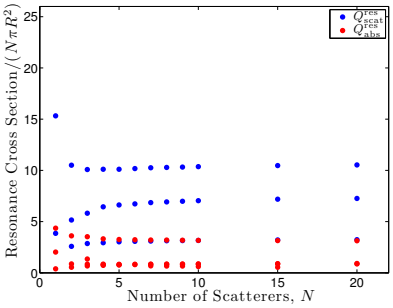

(d) $R = 25$ nm, Transverse, see inset in Fig. 5.8(b)

Figure D.10 Resonance cross sections from the spectra with N scatterers and fixed gap, $d = R$, between the scatterers; The spectra are presented in Appendices D.2.1 and D.2.2.

APPENDIX

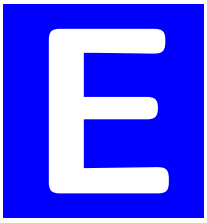

TaCoNa 2012 Contribution

On the following pages, we attach the contribution that was submitted to The Fifth International Workshop on Theoretical and Computational Nano-Photonics (TaCoNa), to be held in October, 2012, in Bad Honnef, Germany. The contribution contains selected parts of the work presented in this thesis.

Multiple-scattering formalism beyond the quasistatic approximation: Analyzing resonances in plasmonic chains

Jakob Rosenkrantz de Lasson, Philip Trøst Kristensen and Jesper Mørk

DTU Fotonik, Technical University of Denmark, DK-2800 Kongens Lyngby, Denmark

Abstract. We present a multiple-scattering formalism for simulating scattering of electromagnetic waves on spherical inhomogeneities in 3D. The formalism is based on the Lippmann-Schwinger equation and the electromagnetic Green's tensor and applies an expansion of the electric field on spherical wavefunctions. As an example, we analyze localized surface plasmons in chains of Ag spheres, and show how the resonances of such systems depend sensitively on the polarization of the incoming field, the spacing between the particles and the number of particles in the chain.

Keywords: Electromagnetic Green's tensor, scattering, plasmonic nanoparticles, localized surface plasmons
PACS: 02.70.-c, 41.20.-q, 42.25.Fx, 78.20.Bh

INTRODUCTION

Plasmonics has received significant attention in recent years, and diverse applications, including metallic nanoantennas [1], waveguiding beyond the diffraction limit [2] and plasmonic solar cells [3], have been proposed. The possibilities for tailoring the spectra of such systems are intriguing, and at resonance localized surface plasmons (LSPs) give rise to strong field enhancements in the vicinity of the metal particles (see Fig. 1). Consequently, accurate modeling of the electromagnetic field is important, and in particular when particles are closely spaced, modeling of the field beyond the quasistatic approximation is needed [4]. In this context, we present a scattering formalism for modeling optical microstructures and nanosize plasmonic systems, including calculations of the Green's tensor, the Local Density of States (LDOS), Purcell factors and cavity modes [5].

We consider N spherical and non-magnetic scatterers, with permittivities ε_j, embedded in a background medium with permittivity ε_B. The structure is illuminated by the field $\mathbf{E}_\mathrm{B}$, and assuming harmonic time-dependence, $\mathbf{E}(\mathbf{r};t) = \mathbf{E}(\mathbf{r};\omega)\exp(-i\omega t)$, the resulting field is the sum of the incoming field and the scattered field [6]

$$\mathbf{E}(\mathbf{r}) = \mathbf{E}_\mathrm{B}(\mathbf{r}) + \int_V \mathbf{G}_\mathrm{B}(\mathbf{r},\mathbf{r}')k_0^2\Delta\varepsilon(\mathbf{r}')\mathbf{E}(\mathbf{r}')\,\mathrm{d}\mathbf{r}', \qquad (1)$$

with $\mathbf{E}(\mathbf{r}) \equiv \mathbf{E}(\mathbf{r};\omega)$, $k_0 \equiv \omega/c$ and $\Delta\varepsilon(\mathbf{r}) \equiv \varepsilon(\mathbf{r}) - \varepsilon_\mathrm{B}$. V is the volume of the the scatterers, where $\Delta\varepsilon(\mathbf{r}) \neq 0$, and $\mathbf{G}_\mathrm{B}(\mathbf{r},\mathbf{r}')$ is the electromagnetic Green's tensor of the background medium. Eq. (1) is the so-called Lippmann-Schwinger equation which is an implicit equation for the electric field for $\mathbf{r} \in V$; Once it is known in these regions, it is explicit for $\mathbf{r} \notin V$.

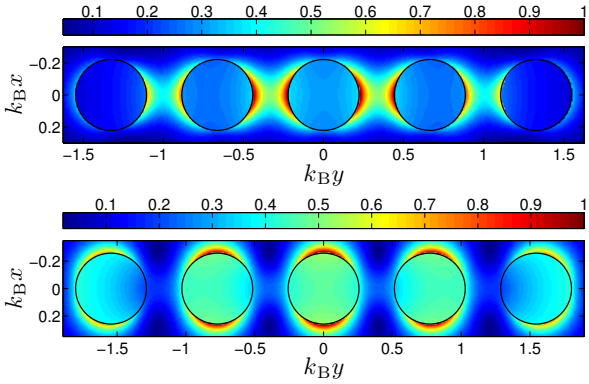

FIGURE 1. Localized surface plasmons around $N = 5$ Ag spheres of radius $R = 10$ nm and spaced a distance $d = R$. Illustrated in $z = 0$-plane. **Top panel:** y-polarization. **Bottom panel:** x-polarization.

The use of the electromagnetic Green's tensor is convenient since the scattered field by construction satisfies the outgoing wave boundary condition in the far-field

$$\mathbf{E}_\mathrm{scat}(\mathbf{r}) \sim \mathbf{f}(\theta,\phi)\frac{\exp(ik_\mathrm{B}r)}{r}, \qquad k_\mathrm{B}r \to \infty, \qquad (2)$$

where $\mathbf{f}(\theta,\phi)$ is the far-field radiation pattern, that is computed analytically in the present formulation.

MULTIPLE-SCATTERING FORMALISM

For solving Eq. (1) we use the general technique of Ref. [7], which we have generalized for 3D problems.

We expand the field and the background field inside the jth scatterer, centered at $\mathbf{r}_j^0$, as follows

$$\mathbf{E}(\mathbf{r}) = \sum_\alpha \sum_\nu a_{\nu,\alpha}^j \psi_\nu^j(\mathbf{r}_j)\,\mathbf{e}_\alpha, \tag{3}$$

$$\mathbf{E}_\mathrm{B}(\mathbf{r}) = \sum_\alpha \sum_\nu a_{\nu,\alpha}^{j,\mathrm{B}} \psi_\nu^{j,\mathrm{B}}(\mathbf{r}_j)\,\mathbf{e}_\alpha, \tag{4}$$

with

$$\psi_\nu^j(\mathbf{r}_j) = K_j(\mathbf{r}_j) j_l(k_j r_j) Y_l^m(\theta_j,\phi_j), \tag{5}$$

$$\psi_\nu^{j,\mathrm{B}}(\mathbf{r}_j) = \psi_\nu^j(\mathbf{r}_j)\,(k_j \to k_\mathrm{B}), \tag{6}$$

where $\mathbf{r}_j \equiv \mathbf{r} - \mathbf{r}_j^0$ and $k_j \equiv k_0\sqrt{\varepsilon_j}$. The functions $j_l(x)$ and $Y_l^m(\theta,\phi)$ are the spherical Bessel function of order l and the spherical harmonic of degree l and order m, respectively. $K_j(\mathbf{r}_j)$ contains the normalization of the basis functions and vanishes outside scatterer j, ensuring orthogonality of basis functions of different scatterers. $\nu = \{l,m\}$ is a composite index and $\alpha \in \{x,y,z\}$ is a Cartesian component. Finally, $a_{\nu,\alpha}^j$ are the unknown expansion coefficients, and $a_{\nu,\alpha}^{j,\mathrm{B}}$ are known expansion coefficients of the background field.

Inserting these expansions into Eq. (1), projecting the equation onto $\psi_{\nu'}^{j'}(\mathbf{r}_{j'})\,\mathbf{e}_{\alpha'}$ and summing over all free indices yields a matrix equation for the expansion coefficients

$$\mathbf{a} = \mathbf{M}\mathbf{a}_\mathrm{B} + k_0^2 \mathbf{G}\Delta\varepsilon\mathbf{a}, \tag{7}$$

where $\mathbf{a}$ ($\mathbf{a}_\mathrm{B}$) is a vector containing all $a_{\nu,\alpha}^j$ ($a_{\nu,\alpha}^{j,\mathrm{B}}$). $\mathbf{M}$ is a diagonal matrix, while $\mathbf{G}$ is a non-diagonal matrix. All parts of the formalism are expressed analytically, which prompts high speed in calculations, and rearranging the central Eq. (1) yields an explicit error estimate [7]. This and the direct possibilities for extending to multi-layered geometries [6, 7] makes the formalism viable for modeling, e.g., plasmonic thin-film solar cells.

Scattering objects are commonly characterized by the extinction cross section, C_ext, that may be elegantly computed using the Optical theorem [8]

$$C_\mathrm{ext} = \frac{4\pi}{k_\mathrm{B}} \mathrm{Im}\left(\mathbf{f}(\theta_\mathrm{in},\phi_\mathrm{in})\cdot\mathbf{e}_\mathrm{in}^*\right), \tag{8}$$

where θ_in and ϕ_in are the spherical angles of the incoming field's wave vector, and $\mathbf{f}(\theta,\phi)$ is given by Eq. (2). $\mathbf{e}_\mathrm{in}$ is the unit polarization vector for the incoming field. It is customary to normalize C_ext to the geometrical cross section, giving the extinction efficiency $Q_\mathrm{ext} \equiv C_\mathrm{ext}/(N\pi R^2)$.

EXAMPLE 1: TWO PARTICLES

We consider two Ag particles (y-direction), of radius $R =$ 10 nm and spaced a distance d. They are embedded in SiO$_2$ ($\varepsilon_\mathrm{B} = 2.25$), and the permittivity of the Ag spheres is given by the Drude model ($\varepsilon(\omega) = 1 - \omega_\mathrm{p}^2/(\omega^2 + i\gamma\omega)$ with $\omega_\mathrm{p} = 7.9$ eV and $\gamma = 0.06$ eV [9]). We illuminate these by plane waves with an incoming $\mathbf{k}$-vector perpendicular (z-direction) to the dimer axis, and polarized along the dimer axis (y-pol.) or perpendicular to the dimer axis (x-pol.).

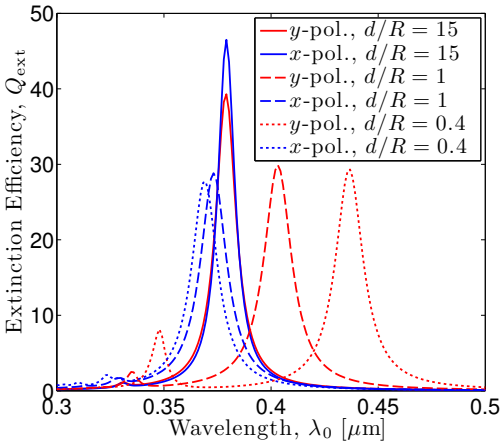

FIGURE 2. Dimer of two Ag spheres, of radius $R = 10$ nm, and spaced the distance d. Extinction efficiency for y- and x-polarization for three values of d/R.

The extinction spectra are shown for three values of d/R, for the two polarizations, in Fig. 2. The dominant peaks are the dipole resonances, and we observe a redshift and a blueshift for y- and x-polarizations, respectively. To study this more systematically, we plot the resonance wavelengths, λ_0^Res, as function of d/R for the two polarizations in the top panel of Fig. 3. The redshift stems from the induced charges of opposite signs on the spheres in the gap; It acts as a dipole whose potential energy decreases for decreasing d/R [10].

To quantify the dependence of the resonance wavelength under y-polarization, we define the peak shift ratio [10]

$$\Delta\lambda_0^\mathrm{Res} \equiv \frac{\lambda_0^\mathrm{Res} - \lambda_0^\mathrm{single}}{\lambda_0^\mathrm{single}}, \tag{9}$$

where $\lambda_0^\mathrm{single}$ is the resonance wavelength of the isolated Ag sphere. The authors in [10] suggest an exponential increase of $\Delta\lambda_0^\mathrm{Res}$ for decreasing d/R, $\Delta\lambda_0^\mathrm{Res} \sim \exp(-(d/R)/\eta_d)$, η_d being a characteristic interaction length, while a softer dependence on d/R is found in [11], $\Delta\lambda_0^\mathrm{Res} \sim 1/(d/R)$. The latter is explained by the van der Waals force between the spheres that scales inversely with the gap distance.

In the bottom panel of Fig. 3, we show $\Delta\lambda_0^\mathrm{Res}$ as function of $(d/R)^{-1/2}$, and the agreement with the linear fit is acceptable. Similar analyses with two spheres of

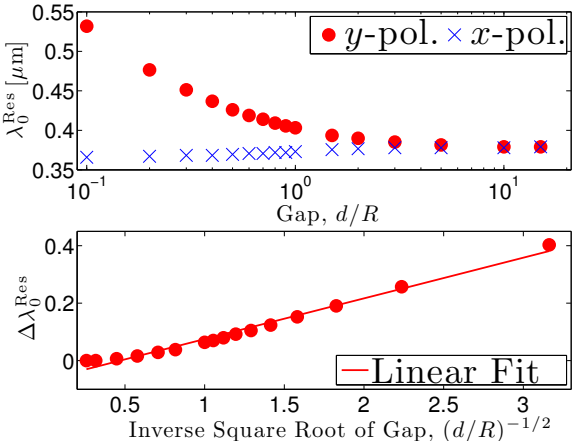

FIGURE 3. Dimer of two Ag spheres, of radius $R = 10$ nm, and spaced the distance d. **Top panel:** Resonance wavelengths in extinction spectra as function of d/R. **Bottom panel:** Peak shift ratio as function of $(d/R)^{-1/2}$.

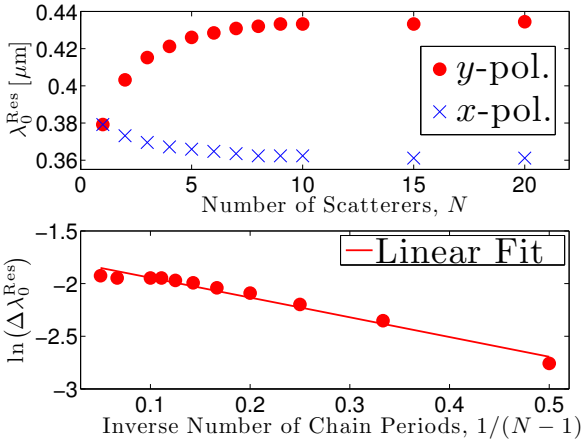

FIGURE 4. Chain of N Ag spheres, of radius $R = 10$ nm, and spaced the distance $d = R$. **Top panel:** Resonance wavelengths as function of N. **Bottom panel:** Logarithm of peak shift ratio as function of inverse number of chain periods, $1/(N-1)$.

radius $R = 25$ nm (not included here) indicate a similar dependence, suggesting a slower increase of the peak shift ratio than reported earlier.

EXAMPLE 2: N PARTICLES

We consider a chain of N Ag spheres, of radius $R = 10$ nm and spaced the distance $d = R$. We vary N and expose them to the y- and x-polarized plane waves described in the previous section. This gives a spectrum for each value of N and for each polarization, and the top panel in Fig. 4 shows the resonance wavelengths as function N.

We observe a clear redshift and a slight blueshift in the y- and x-polarized cases, respectively. For $N = 5$, Fig. 1 shows shows the LSPs in the $z = 0$-plane in the two cases. The induced charges of opposite signs in the gaps in the former case (top panel) give rise to strong field enhancements between the spheres, yielding a redshift as more particles are added. In contrast, for x-polarization (bottom panel) the field is essentially located on the individual particles, with no interaction across the gaps.

In the y-polarized case, an exponential-like convergence to an asymptotic resonance wavelength is observed for increasing N, suggesting that $\Delta\lambda_0^{\mathrm{Res}} \sim \exp(-\eta_N/(N-1))$. The bottom panel of Fig. 4 shows $\ln\left(\Delta\lambda_0^{\mathrm{Res}}\right)$ as function of the inverse number of periods in the chain, $1/(N-1)$. The agreement with the linear fit is not excellent, but acceptable, giving $\eta_N = 1.9$. This suggests an interaction length of approximately two periods in the chain, i.e., each particle interacts with its two nearest neighbors. A similar conclusion is reached in [11].

In conclusion, we have outlined a scheme based on the Lippmann-Schwinger equation and the electromagnetic Green's tensor for simulating, in 3D, scattering of electromagnetic waves on N spheres. The method can be used for calculations of the Green's tensor and the LDOS as well as Purcell factors and cavity modes in optical microstructures (including photonic crystals) and plasmonic nanostructures. We presented two example calculations of the latter, where the resonance wavelengths for chains of Ag nanoparticles were analyzed. We found a strong dependence on the polarization of the incoming field, and a finite interaction length along the chain.

REFERENCES

1. L. Novotny, and N. van Hulst, *Nat. Photon.* **5**, 83–90 (2011).
2. D. K. Gramotnev, and S. I. Bozhevolnyi, *Nat. Photon.* **4**, 83–91 (2010).
3. H. A. Atwater, and A. Polman, *Nat. Mater.* **9**, 205–213 (2010).
4. S. Y. Park, and D. Stroud, *Phys. Rev. B* **69**, 125418 (2004).
5. P. T. Kristensen, C. V. Vlack, and S. Hughes, *Opt. Lett.* **37**, 1649–1651 (2012).
6. L. Novotny, and B. Hecht, *Principles of Nano-Optics*, Cambridge University Press, 2006, first edn.
7. P. T. Kristensen, P. Lodahl, and J. Mørk, *J. Opt. Soc. Am. B* **27**, 228–237 (2010).
8. J. D. Jackson, *Classical Electrodynamics*, Wiley, 1998, third edn.
9. A. F. Koenderink, *Opt. Lett.* **35**, 4208–4210 (2010).
10. P. K. Jain, W. Huang, and M. A. El-Sayed, *Nano Lett.* **7**, 2080–2088 (2007).
11. N. Harris, M. D. Arnold, M. G. Blaber, and M. J. Ford, *J. Phys. Chem. C* **113**, 2784–2791 (2009).

Bibliography

[1] D. K. Gramotnev and S. I. Bozhevolnyi, "Plasmonics beyond the diffraction limit," Nat. Photon. **4**, 83–91 (2010).

[2] P. Berini and I. D. Leon, "Surface plasmon-polariton amplifiers and lasers," Nat. Photon. **6**, 16–24 (2012).

[3] M. L. Juan, M. Righini, and R. Quidant, "Plasmon nano-optical tweezers," Nat. Photon. **5**, 349–356 (2011).

[4] L. Novotny and N. van Hulst, "Antennas for light," Nat. Photon. **5**, 83–90 (2011).

[5] W. Zhang, L. Huang, C. Santschi, and O. J. F. Martin, "Trapping and sensing 10 nm metal nanoparticles using plasmonic dipole antennas," Nano Lett. **10**, 1006–1011 (2010).

[6] K. R. Catchpole and A. Polman, "Plasmonic solar cells," Opt. Express **16**, 21793–21800 (2008).

[7] H. A. Atwater and A. Polman, "Plasmonics for improved photovoltaic devices," Nat. Mater. **9**, 205–213 (2010).

[8] K. Nakayama, K. Tanabe, and H. A. Atwater, "Plasmonic nanoparticle enhanced light absorption in GaAs solar cells," Appl. Phys. Lett. **93**, 121904 –121904–3 (2008).

[9] S. Xiao, E. Stassen, and N. A. Mortensen, "Ultrathin silicon solar cells with enhanced photocurrents assisted by plasmonic nanostructures," J. Nanophoton. **6**, 061503 (2012).

[10] A. Taflove and S. Hagness, *Computational Electrodynamics: The Finite-Difference Time-Domain Method* (Artech House, 2005), 3rd ed.

[11] J. Reddy, *An Introduction to the Finite Element Method* (McGraw-Hill Science/Engineering/Math, 2005), 3rd ed.

[12] G. Mie, "Articles on the optical characteristics of turbid tubes, especially colloidal metal solutions," Ann. Phys. **25**, 377–445 (1908).

[13] Y. Akimov, K. Ostrikov, and E. Li, "Surface plasmon enhancement of optical absorption in thin-film silicon solar cells," Plasmonics **4**, 107–113 (2009).

[14] S. A. Maier, *Plasmonics: Fundamentals and Applications* (Springer, 2007), 1st ed.

[15] S. Y. Park and D. Stroud, "Surface-plasmon dispersion relations in chains of metallic nanoparticles: An exact quasistatic calculation," Phys. Rev. B **69**, 125418 (2004).

[16] Y. lin Xu, "Electromagnetic scattering by an aggregate of spheres," Appl. Opt. **34**, 4573–4588 (1995).

[17] F. J. García de Abajo, "Multiple scattering of radiation in clusters of dielectrics," Phys. Rev. B **60**, 6086–6102 (1999).

[18] P. T. Kristensen, "Light-matter interaction in nanostructured materials," Ph.D. thesis, Technical University of Denmark, Department of Photonics Engineering (2009).

[19] P. T. Kristensen, P. Lodahl, and J. Mørk, "Light propagation in finite-sized photonic crystals: multiple scattering using an electric field integral equation," J. Opt. Soc. Am. B **27**, 228–237 (2010).

[20] L. C. Botten, R. C. McPhedran, N. A. Nicorovici, A. A. Asatryan, C. M. de Sterke, P. A. Robinson, K. Busch, G. H. Smith, and T. N. Langtry, "Rayleigh multipole methods for photonic crystal calculations," Prog. Electromagn. Res. **41**, 21–60 (2003).

[21] K. Vahala, "Optical microcavities," Nature **424**, 839–846 (2003).

[22] J. Claudon, J. Bleuse, N. S. Malik, M. Bazin, P. Jaffrennou, N. Gregersen, C. Sauvan, P. Lalanne, and J.-M. Gérard, "A highly efficient single-photon source based on a quantum dot in a photonic nanowire," Nat. Photon. **4**, 839–846 (2010).

[23] E. Purcell, "Spontaneous emission probabilities at radio frequencies," Phys. Rev. **69**, 681 (1946).

[24] L. Novotny and B. Hecht, *Principles of Nano-Optics* (Cambridge University Press, 2006), 1st ed.

[25] J. D. Jackson, *Classical Electrodynamics* (Wiley, 1998), 3rd ed.

[26] M. Born and E. Wolf, *Principles of Optics: Electromagnetic Theory of Propagation Interference and Diffraction of Light* (Pergamon Pr, 1981), 6th ed.

[27] A. D. Yaghjian, "Electric dyadic Green's functions in the source region," Proc. IEEE **68**, 248–263 (1980).

[28] O. J. F. Martin and N. B. Piller, "Electromagnetic scattering in polarizable backgrounds," Phys. Rev. E **58**, 3909–3915 (1998).

[29] J. J. Sakurai, *Modern Quantum Mechanics* (Addison-Wesley, 1994), 2nd ed.

[30] A. Ishimaru, *Wave Propagation and Scattering in Random Media* (IEEE Press, 1997), 1st ed.

[31] A. A. Kokhanovsky, *Aerosol Optics: Light Absorption and Scattering by Particles in the Atmosphere* (Springer, 2008), 1st ed.

[32] A. F. Koenderink, "On the use of Purcell factors for plasmon antennas," Opt. Lett. **35**, 4208–4210 (2010).

[33] A. F. Peterson, S. L. Ray, and R. Mittra, *Computational Methods for Electromagnetics* (IEEE Press, 1998), 1st ed.

[34] P. A. Martin, *Multiple Scattering. Interaction of Time-Harmonic Waves with N Obstacles.* (Cambridge University Press, 2006), 1st ed.

[35] H. Bruus and K. Flensberg, *Many-Body Quantum Theory in Condensed Matter Physics* (Oxford University Press, 2004), 1st ed.

[36] P. T. Kristensen, C. V. Vlack, and S. Hughes, "Generalized effective mode volume for leaky optical cavities," Opt. Lett. **37**, 1649–1651 (2012).

[37] M. R. Spiegel, S. Lipschutz, and J. Liu, *Schaum's Outline of Mathematical Handbook of Formulas and Tables* (McGraw-Hill, 2008), 3rd ed.

[38] F. Capolino, *Theory and Phenomena of Metamaterials* (CRC Press, 2009), 1st ed.

[39] N. Harris, M. D. Arnold, M. G. Blaber, and M. J. Ford, "Plasmonic resonances of closely coupled gold nanosphere chains," J. Phys. Chem. C **113**, 2784–2791 (2009).

[40] C. Mätzler, "MATLAB functions for Mie scattering and absorption, version 2," MATLAB code, Institut für angewandte Physik, Universität Bern (2002).

[41] P. A. Martin, "Multiple scattering and the Rehr-Albers-Fritzsche formula for the propagator matrix," J. Phys. A **31**, 8923 (1998).

[42] P. K. Jain, W. Huang, and M. A. El-Sayed, "On the universal scaling behavior of the distance decay of plasmon coupling in metal nanoparticle pairs: A plasmon ruler equation," Nano Lett. **7**, 2080–2088 (2007).

[43] M. Chen, Y.-F. Chau, and D. Tsai, "Three-dimensional analysis of scattering field interactions and surface plasmon resonance in coupled silver nanospheres," Plasmonics **3**, 157–164 (2008).

[44] M. Lermer, N. Gregersen, F. Dunzer, S. Reitzenstein, S. Höfling, J. Mørk, L. Worschech, M. Kamp, and A. Forchel, "Bloch-wave engineering of quantum dot micropillars for cavity quantum electrodynamics experiments," Phys. Rev. Lett. **108**, 057402 (2012).

[45] B. T. Draine and P. J. Flatau, "Discrete-dipole approximation for scattering calculations," J. Opt. Soc. Am. A **11**, 1491–1499 (1994).

[46] D. W. Mackowski and M. I. Mishchenko, "Calculation of the T matrix and the scattering matrix for ensembles of spheres," J. Opt. Soc. Am. A **13**, 2266–2278 (1996).

[47] S. Raza, G. Toscano, A.-P. Jauho, M. Wubs, and N. A. Mortensen, "Unusual resonances in nanoplasmonic structures due to nonlocal response," Phys. Rev. B **84**, 121412 (2011).

[48] N. Liu, M. Hentschel, T. Weiss, A. P. Alivisatos, and H. Giessen, "Three-dimensional plasmon rulers," Science **332**, 1407–1410 (2011).

[49] J. D. Joannopoulos, S. G. Johnson, J. N. Winn, and R. D. Meade, *Photonic Crystals – Molding the Flow of Light* (Princeton University Press, 2008), 2nd ed.

[50] J. Jung, T. Søndergaard, T. G. Pedersen, K. Pedersen, A. N. Larsen, and B. B. Nielsen, "Dyadic Green's functions of thin films: Applications within plasmonic solar cells," Phys. Rev. B **83**, 085419 (2011).

[51] M. Paulus, P. Gay-Balmaz, and O. J. F. Martin, "Accurate and efficient computation of the Green's tensor for stratified media," Phys. Rev. E **62**, 5797–5807 (2000).

[52] J. Kellendonk and S. Richard, "Weber-Schafheitlin-type integrals with exponent 1," Integr. Transf. Spec. F. **20**, 147–153 (2009).

[53] S. Richard (2012). Personal communication with author of Ref. [52].

[54] B. Li and C. Liu, "Multi-scattering of electromagnetic waves by nanoshell aggregates," J. Nanopart. Res. **14**, 1–11 (2012).